A MEASUREMENT OF THE CROSS SECTION FOR W PRODUCTION AND DECAY INTO ELECTRON AND NEUTRINO IN $P\bar{P}$ COLLISIONS AT $\sqrt{S} = 1.8$ TEV

Marshall Miller

A DISSERTATION

in

PHYSICS

Presented to the Faculties of the University of Pennsylvania in Partial Fulfillment of the Requirements for the Degree of Doctor of Philosophy

1989

Hugh H. Williams
Supervisor of Dissertation

H T Fortune
Graduate Group Chairperson

ACKNOWLEDGMENTS

I owe a great debt to the numerous people who, throughout my years in graduate school, have aided my education in and understanding of particle physics. I most wish to thank my advisor, Brig Williams, for many valuable discussions on all aspects of my thesis topic. I am especially thankful to Steve Hahn for having the patience to answer a myriad questions from details of calibration to the wonders of TEX.

The members of the CDF group at the University of Pennsylvania were always very helpful by answering questions, providing assistance, lending support, and especially by creating an enjoyable atmosphere in which to work.

CDF is an enormous collaboration of physicists, technicians, and support people. My thesis required the design, building, and testing of the detector and data acquisition system, the writing of data acquisition, analysis, and simulation software, and the coordination of thousands of person-years of time and effort devoted to extracting useful physics from this endeavour. I thank everyone who contributed to this effort.

ABSTRACT

A MEASUREMENT OF THE CROSS SECTION FOR W PRODUCTION AND DECAY INTO ELECTRON AND NEUTRINO IN $P\overline{P}$ COLLISIONS AT $\sqrt{S} = 1.8$ TEV

Marshall Miller

Dissertation Supervisor: H. H. Williams

The cross section for W production and decay into electron and neutrino was measured at the Fermilab Tevatron at $\sqrt{s} = 1.8$ TeV. The integrated luminosity used for the study was 25.3 nb^{-1}. We find $\sigma(p\bar{p} \rightarrow WX \rightarrow e\nu X) = 2.5 \pm 0.6$ (stat) $\pm$ 0.5 (syst) nb. We fit the transverse mass distribution from the W candidates to Monte Carlo calulations to find $M_W = 79.5 \pm 2.9$ (stat) $\pm$ 2.4 (syst) GeV. The cross section agrees with theoretical predictions, and the mass measurement agrees with W mass values quoted by the UA1 and UA2 experiments at CERN.

Contents

List of Tables

List of Figures

Chapter 1

Introduction

This thesis describes measurements of W boson production at the Fermilab Tevatron by the CDF collaboration [1]. The W and Z particles are massive vector bosons which mediate the weak force. They were first detected at the CERN Sp$\bar{p}$S by the UA1 and UA2 experiments [2,3] confirming predictions of the Weinberg-Glashow-Salam electroweak theory [4,5,6]. The W is short-lived, and only its decay products are detected. W bosons have several decay modes; however, due to certain features of the leptonic modes, the easiest to detect are the decays $W \rightarrow e\nu$ and $W \rightarrow \mu\nu$. Analysis of data from the 1987 colliding beam run at Fermilab has produced events demonstrating both decay modes. This thesis will discuss only the $W \rightarrow e\nu$ events from this run.

The detection of W bosons is aided by their often spectacular event signature. W bosons are massive particles whose leptonic decays can result in very distinctive events. In the $W \rightarrow e\nu$ decay, the electron deposits energy in the electromagnetic

calorimeter, and the neutrino goes undetected due to its extremely small interaction cross section. The event signature is then a high p_T electromagnetic cluster with no detected particles to balance the momentum. At $p\bar{p}$ colliders, events with high p_T electrons are produced at very low rates, and large missing momentum is associated with the production of a high p_T neutrino, calorimeter problems or mismeasured energy, or new physics. Certain physics processes produce background to W production, but these backgrounds can be shown to occur at much lower rates than the W signal. The electron E_T distribution from the sample of $W \rightarrow e\nu$ candidates may be compared with theoretical expectations for further evidence that the candidates constitute a clean W signal.

The $W \rightarrow e\nu$ sample selected from the 1987 colliding beam run at Fermilab consists of 21 events and corresponds to an integrated luminosity of 25.3 nb^{-1}. From this sample we are able to determine the cross section at a new center of mass energy of 1.8 TeV, and we can confirm the W mass measurements of the UA experiments although our present errors are larger. Details of the event selection from the 1987 run resulted in our sample containing only W bosons whose electrons entered the central part of the detector; consequently, our efficiency for W detection was significantly lower than we anticipate in future runs.

The W boson has 2 charged states, the W^+ and W^- . The specific decays involving electrons or positrons are $W^+ \rightarrow e^+\nu_e$ and $W^- \rightarrow e^-\bar{\nu}_e$. The details of the cross

section analysis do not depend on the charge of the W or the specific decay – only that an electron and neutrino are produced. In this thesis I will usually refer only to W bosons, electrons, and neutrinos and not keep track of the particle – anti-particle details.

Some details of the analysis contained in this thesis could not be studied directly from data; therefore, we used Monte Carlo simulations of physics processes and detector performance to study these effects. Unless we specify otherwise, the term "Monte Carlo" will always refer to version 6.10 of the Isajet Monte Carlo [7]. Detector simulations use a software package written explicitly to model the CDF detector and based on extensive testbeam data.

Chapter 2

Theory

The standard electroweak gauge theory [8] is based on the gauge group $SU_2 \times U_1$ and contains 4 gauge bosons, 3 fermion generations, and neutral, scalar particles called Higgs particles. The gauge bosons are the photon, which carries the electromagnetic force, and 3 massive, vector particles known as the Z, W^+ , and W^- . The W^+ and W^- transmit charged current weak interactions in which one unit of electric charge is exchanged while the Z transmits neutral current weak interactions where no charge is exchanged. The fermions consist of 3 generations of leptons and quarks.

$$\begin{pmatrix} \nu_e \\ e \end{pmatrix} \quad \begin{pmatrix} \nu_\mu \\ \mu \end{pmatrix} \quad \begin{pmatrix} \nu_\tau \\ \tau \end{pmatrix} \quad \text{leptons}$$

$$\begin{pmatrix} u \\ d \end{pmatrix} \quad \begin{pmatrix} c \\ s \end{pmatrix} \quad \begin{pmatrix} t \\ b \end{pmatrix} \quad \text{quarks}$$

Left-handed fermions (right-handed anti-fermions) transform as weak isospin doublets and couple to the weak interaction whereas right-handed fermions (left-handed anti-

fermions) transform as weak isospin singlets and only couple to the neutral component of the weak force. The standard model has no right-handed neutrinos. In order to give masses to the fermions and gauge bosons, the Higgs field is introduced [9]. Its self-interactions give rise to spontaneous symmetry breaking yielding fermion and boson masses as well as Higgs particles. The terms in the Lagrangian which give rise to fermion masses require both a left-handed and a right-handed fermion; therefore, the neutrinos cannot acquire masses in this manner and are assumed massless.

The electroweak interaction Lagrangian involving fermions but excluding Higgs interactions can be written:

$$L = -eJ^{\mu}_{em}A_{\mu} - \frac{g}{\sqrt{2}}\left(J^{+\mu}_{W}W^{+}_{\mu} + J^{-\mu}_{W}W^{-}_{\mu}\right) + \frac{g}{\cos\theta_W}J^{\mu}_{Z}Z_{\mu} \qquad (2.1)$$

where θ_W is the weak mixing angle, e and g are coupling constants related by $e = g\sin\theta_{\rm W}$, A is the massless photon field, Z is the massive neutral weak boson field, W^+ and W^- are the massive charged weak boson fields, and J_{em}, J_W, and J_Z are the various weak currents. The weak currents can be written in terms of fermion fields, ψ, the charge and weak isospin operators, Q and T, and the gamma matrices, γ^{μ}:

$$\begin{aligned} J^{\pm\mu}_{W} &= \sqrt{2}\,\overline{\psi}_{q}\gamma^{\mu}T^{\pm}_{L}V\psi_{q} + \sqrt{2}\,\overline{\psi}_{l}\gamma^{\mu}T^{\pm}_{L}\psi_{l} \\ J^{\mu}_{Z} &= \overline{\psi}\gamma^{\mu}\left[T_{3L} - \sin^{2}\theta_{\rm W}{\rm Q}\right]\psi \\ J^{\mu}_{em} &= \overline{\psi}\gamma^{\mu}Q\psi \end{aligned}$$

where ψ_q is the quark field, ψ_l is the lepton field, and V is the Kobayashi-Maskawa-Cabbibo mixing matrix. The weak isospin operators vanish on right-handed fermion (left-handed anti-fermion) fields. From equation 2.1 and the currents, $J_W^{\pm\mu}$, the W^+ and W^- couple to members of the same lepton weak isospin doublet (i.e. $e\nu_e$, $\mu\nu_\mu$, or $\tau\nu_\tau$) or, to any quark pair whose corresponding mixing matrix coefficient does not vanish.

The basic parameters of the standard electroweak model are the coupling constants, e and g, and the vacuum expectation value of the Higgs field, v. It is more common to use a different parameterization involving the fine structure constant, α, the Fermi constant, G_F, and $\sin^2\theta_{\rm W}$. Their values are:

$$\begin{aligned} \alpha &= \frac{e^2}{4\pi} = 1/137.036 \quad [10] \\ G_F &= 1/\sqrt{2}v^2 = 1.6637 \times 10^{-5}\ \text{GeV}^{-2} \\ \sin^2\theta_{\rm W} &= (e/g)^2 = 0.230 \quad [11] \end{aligned}$$

Using this parameterization, the weak boson masses are:

$$\begin{aligned} M_W &= A/\sin\theta_{\rm W} \\ M_Z &= A/\sin\theta_{\rm W}\cos\theta_{\rm W} \end{aligned}$$

where

$$A = (\pi\alpha/\sqrt{2}G_F)^{\frac{1}{2}} = 37.2810\ \text{GeV}$$

M_Z may soon be known to very high accuracy from experiments at SLAC [12] and LEP [13]. At that point M_Z will replace $\sin^2\theta_W$ as the third parameter.

To calculate the mass of the W, one must include higher order corrections to the formula given above. These corrections are of order 4%. Using values for $\sin^2\theta_W$ from deep inelastic scattering experiments, $M_W = 80.2 \pm 1.1$ GeV [14].

2.1 Hadronic W $\rightarrow e\nu$ Production

At $p\bar{p}$ colliders W bosons are produced through quark anti-quark interactions (see figure 2.1). To determine the cross section for the process $p\bar{p} \rightarrow WX \rightarrow e\nu X$, we first write the matrix element for the subprocess shown in figure 2.1:

$$M = \frac{G_F}{\sqrt{2}} M_W^2 V_{q\bar{q}} \frac{\overline{v}(\bar{q})\gamma^\alpha(1-\gamma_5)u(q)\overline{u}(\nu)\gamma_\alpha(1-\gamma_5)v(e)}{\hat{s} - M_W^2 + iM_W\Gamma_W} \tag{2.2}$$

where $\sqrt{\hat{s}}$ is the center of mass energy of the 2 interacting quarks and Γ_W is the total width of the W. After squaring and integrating over phase space, the spin-averaged subprocess cross section can be written:

$$\frac{d\hat{\sigma}}{d\cos\hat{\theta}}(q\bar{q} \rightarrow W \rightarrow e\nu) = \frac{|V_{q\bar{q}}|^2}{8\pi}\left(\frac{G_F M_W^2}{\sqrt{2}}\right)^2 \frac{\hat{s}\left(1+\cos\hat{\theta}\right)^2}{\left(\hat{s} - M_W^2\right)^2 + \left(\Gamma_W M_W\right)^2} \tag{2.3}$$

where $\cos\hat{\theta}$ is the center of mass angle between the lepton anti-particle (e^+ or $\bar{\nu}$) and $\bar{p}$. Integrating over all angles, the total subprocess cross section is:

$$\hat{\sigma}(q\bar{q} \rightarrow W \rightarrow e\nu) = \frac{|V_{q\bar{q}}|^2}{3\pi}\left(\frac{G_F M_W^2}{\sqrt{2}}\right)^2 \frac{\hat{s}}{\left(\hat{s} - M_W^2\right)^2 + \left(\Gamma_W M_W\right)^2} \tag{2.4}$$

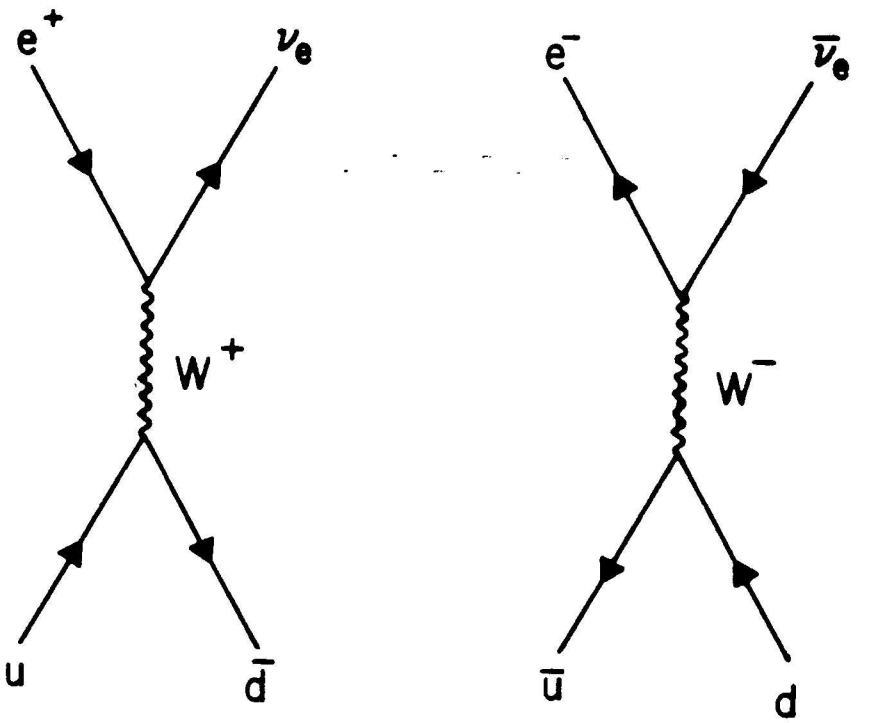

Figure 2.1: Feynmann diagrams for lowest order W boson production and decay into electron and neutrino at $p\bar{p}$ colliders. The u and d quarks dominate the interaction cross section at center of mass energy of 1.8 TeV.

The quarks reside inside the colliding hadrons, and to calculate the cross section from $p\bar{p}$ production of the W we must include all potential $q\bar{q}$ subprocesses. Since the cross section depends on the subprocess center of mass energy, we must know the distribution of the quark momenta inside the hadrons. The function, $f_q^p(x_p, Q^2)$, is called the parton distribution function and gives the probability that hadron p contains a parton q which carries a fraction x_p of the hadron's momentum. These distributions are functions of the variable, $Q^2 = \hat{s}$. The cross sections in equations 2.3 and 2.4 do not include higher order QCD processes such as gluon emission; therefore, to calculate the cross section for W production and decay into electron and neutrino where higher order processes are allowed, we must include a correction known as the K-factor. We can then write the total cross section as:

$$\sigma\left(p\bar{p} \rightarrow WX \rightarrow e\nu X\right) = \frac{K}{3} \sum_{q,q'} \int_0^1 dx_p \int_0^1 dx_{\bar{p}} f_q^p\left(x_p, Q^2\right) f_{q'}^{\bar{p}}\left(x_{\bar{p}}, Q^2\right) \hat{\sigma}\left(q\bar{q}' \rightarrow e\nu\right) \tag{2.5}$$

Including first-order QCD corrections, the K-factor can be written

$$K \simeq 1 + \frac{8\pi}{9}\alpha_s\left(M_W^2\right) \simeq 1.35 \tag{2.6}$$

There are 2 significant sources of theoretical error in this calculation. The proton and anti-proton parton distribution functions are not well known at the Fermilab Tevatron center of mass energy of 1.8 TeV. Until they can be measured, they must be calculated by evolving the distribution functions at lower Q^2. Also the cross section depends on the W total width, Γ_W. The total width is the sum of all partial widths

for specific W decays including the possible decay $W \rightarrow tb$. The top quark has yet to be discovered, and its theoretical mass range is large ($\sim$ 44 - 180 GeV) [15,16]. Figure 2.2 shows the dependence of the W total decay width on the top quark mass. Assuming the top quark mass has a lower limit of 44 GeV, the total cross section can vary by roughly 15%.

Two important W event properties which are measured experimentally are the electron transverse energy, E_T , and the missing transverse energy, $\not\!\!E_T$, of the event. The $\not\!\!E_T$ is the vector sum over all calorimeter towers of the transverse energy deposited in the calorimeter. Since the neutrino doesn't interact in the detector, the neutrino energy and the detector resolution contribute to the $\not\!\!E_T$. We can calculate the expected electron and neutrino p_T distributions from W decay by transforming the subprocess differential cross section $d\hat{\sigma}/d\cos\hat{\theta}$ (equation 2.3) to $d\hat{\sigma}/d\hat{p}_T^2$. We find

$$\frac{d\hat{\sigma}}{d\hat{p}_T^2} = \frac{\hat{\sigma}}{\hat{s}}\frac{3}{2}\frac{(1-2\hat{p}_T^2/\hat{s})}{(1-4\hat{p}_T^2/\hat{s})^{\frac{1}{2}}} \tag{2.7}$$

The distribution diverges at $\hat{p} = \frac{1}{2}\sqrt{\hat{s}} \simeq \frac{1}{2}M_W$ with a characteristic Jacobian peak. Integrating over the parton distribution functions removes this singularity, and including higher order processes (W plus jet production) gives the W transverse momentum which smears the Jacobian. Figure 2.3 shows the electron p_T distribution from W bosons generated by Monte Carlo calculation and simulated in the CDF detector.

If the neutrino were detected in the same manner as the electron, we could calculate the invariant mass of the electron-neutrino pair and directly measure the W

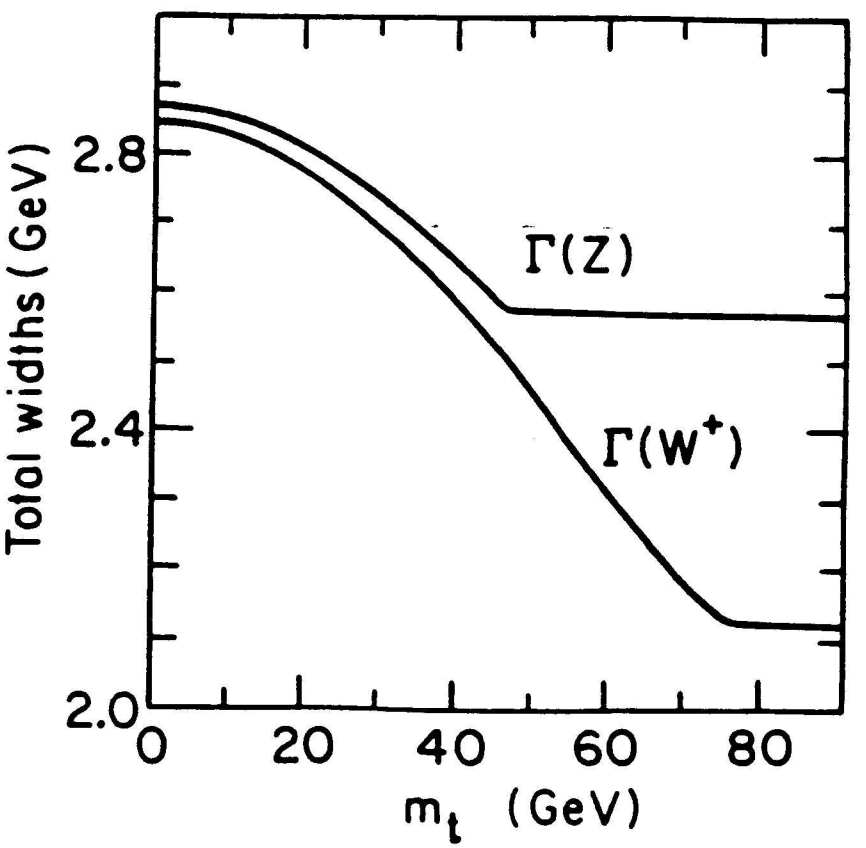

Figure 2.2: Dependence of the W and Z total decay width on the top quark mass.

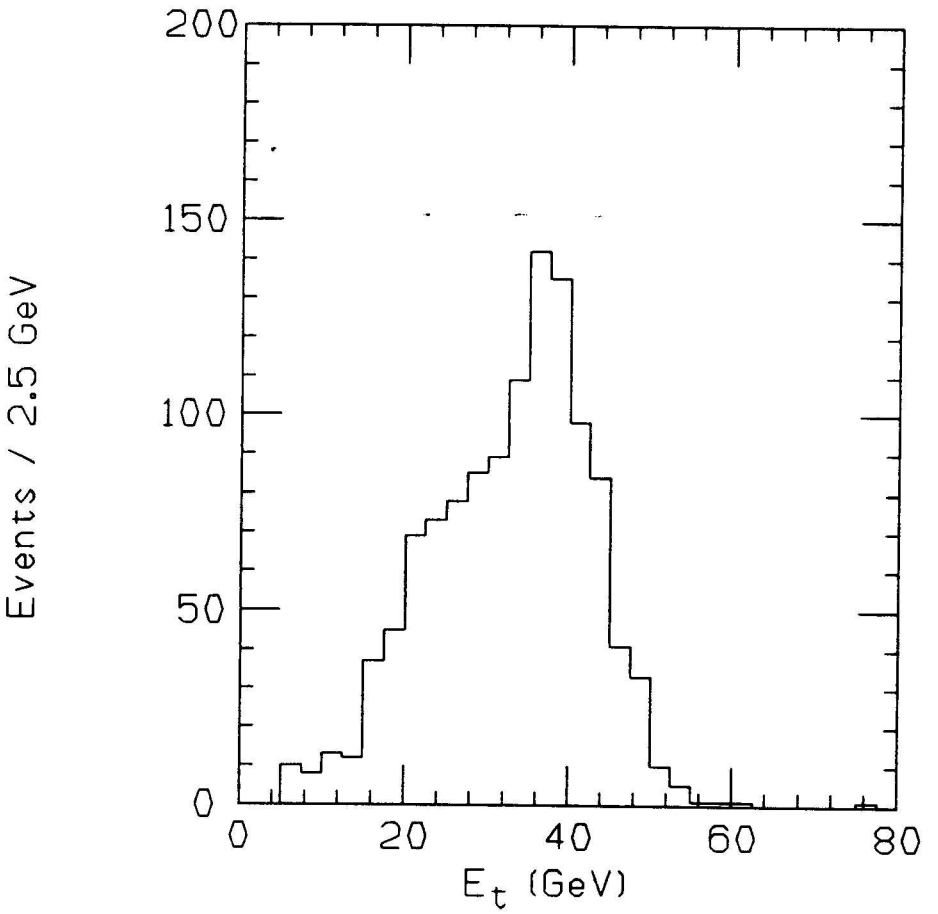

Figure 2.3: Distribution of the electron p_T from the process $W \rightarrow e\nu$. These events were generated by the Isajet Monte Carlo. The electrons were required to deposit > 5 GeV in active regions of the detector.

mass. Since the neutrino is undetected, the only measure we have of its properties is the event $\not\!\!E_T$ which, in a perfect detector, is equal to the neutrino E_T . The electron E_T and event $\not\!\!E_T$ allow us to calculate the W transverse mass defined as:

$$m_T^2(e,\nu) = (|p_{eT}| + |p_{\nu T}|)^2 - (p_{eT} + p_{\nu T})^2 \tag{2.8}$$

We can rewrite equation 2.8 as:

$$m_T^2(e,\nu) = 2E_T \not\!\!E_T (1 - \cos\phi) \tag{2.9}$$

where ϕ is the angle between the electron p_T vector and the $\not\!\!E_T$ vector. The transverse mass distribution is less sensitive to the transverse motion of the produced W than the electron E_T distribution and can yield more accurate mass estimates. Figure 2.4 shows the transverse mass distribution for $W \rightarrow e\nu$ events in the UA1 experiment compared to theoretical calculations which include acceptance and efficiency corrections [17].

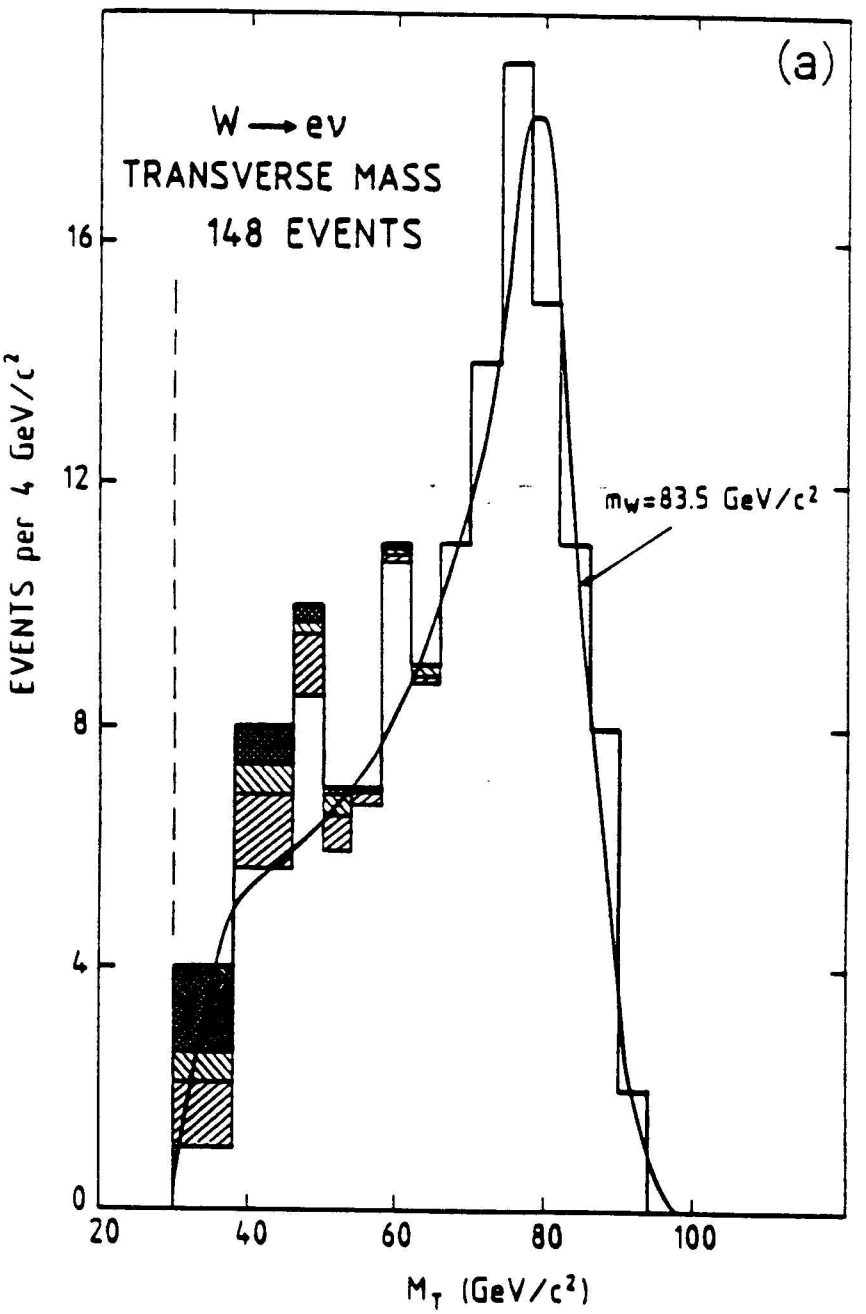

Figure 2.4: Distribution of the tranvserse mass for the process W $\rightarrow e\nu$ at center of mass energy 630 GeV from UA1 data. Curves from theoretical calculations are overlayed.

Chapter 3

The CDF Detector

3.1 Introduction

The CDF detector [1] is a general purpose 4π detector utilizing a solenoidal magnetic field, charged particle tracking, and fine-grained calorimetry to study collisions at the Fermilab Tevatron. Each detector sub-system will be described below; however, since the analysis requires electrons from the decaying W bosons to be contained in the central calorimeter, the sections of the detector relevant to central electron identification will be emphasized. Figure 3.1 shows a perspective view of the full detector, and figure 3.2 shows a cross sectional view with the major components identified.

Since various coordinate systems are useful in discussing detector layouts, event parameters, and W selection criteria, we will define commonly used coordinates here. Theta, θ, is the polar angle measured from either the proton or anti-proton direction along the beam line. Phi, ϕ, is the azimuthal angle around the beam axis. Z is the

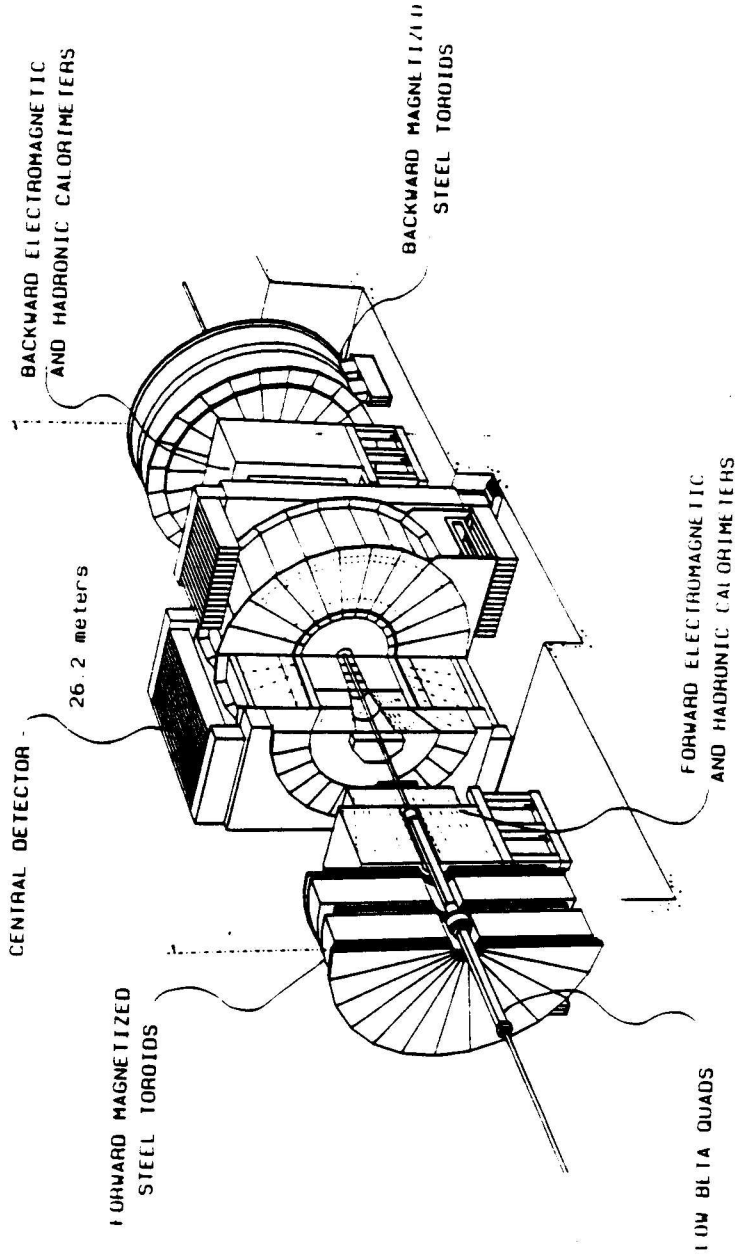

Figure 3.1: A perspective view of the CDF detector.

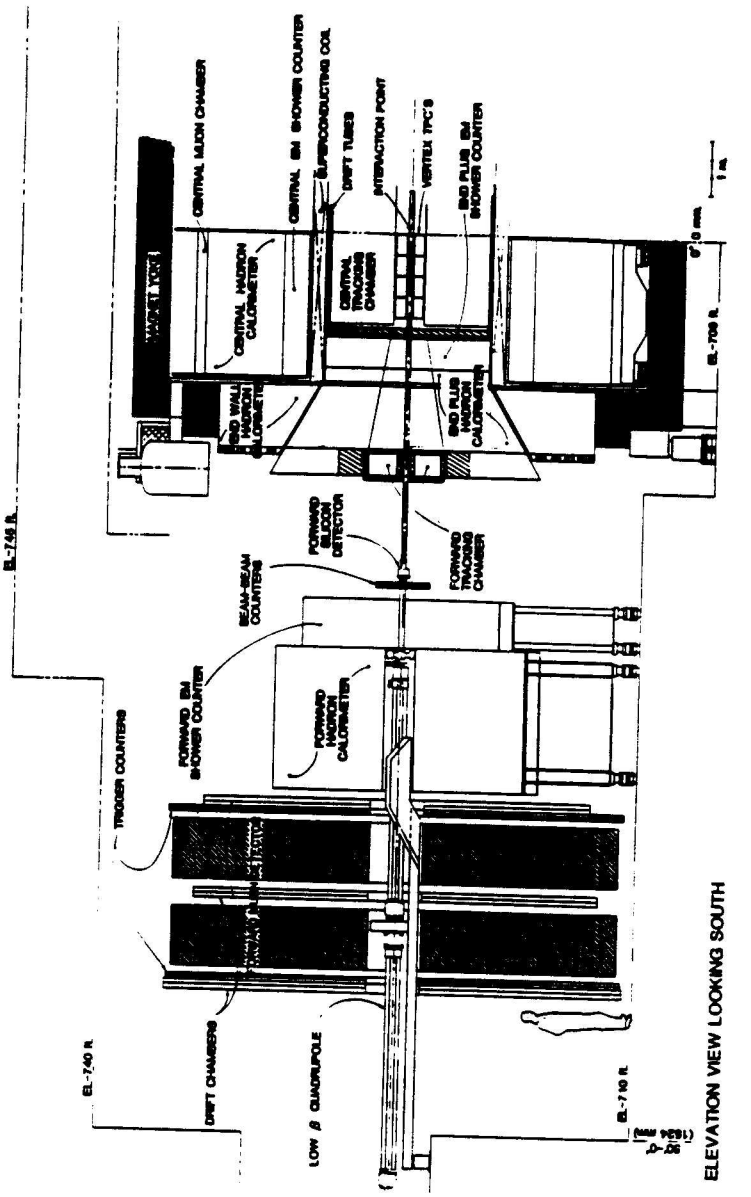

Figure 3.2: A cross sectional view of the CDF detector.

distance along the beam line measured from the center of the detector, and R is the radial distance from the beamline.

3.2 Calorimetry

The calorimetry was constructed in 3 regions each containing several sub-systems: the central region extending out to rapidity of 1.1, the plug region covering rapidity from 1.1 to 2.4, and the forward region reaching to rapidity of 4.2. Each region has an electromagnetic shower counter in front of a hadron calorimeter. The calorimeters were constructed in a projective tower geometry such that each tower points back to the interaction region. The tower sizes are roughly 0.1 units in pseudorapidity, η where $\eta = -\log\ \tan(\theta/2)$, and 15° (central) or 5° (plug and forward) in the azimuthal angle, ϕ.

3.2.1 Central Calorimetry

The central calorimetry consists of the central electromagnetic shower counter, the central hadron calorimeter, and the endwall hadron calorimeter. There are 48 wedge shaped modules, called wedges, which comprise the central EM and hadron calorimeters. They form 4 "C"- shaped arches which surround the solenoid coil. The endwall calorimeter extends the rapidity coverage of the central hadron calorimeter.

The central electromagnetic shower counter

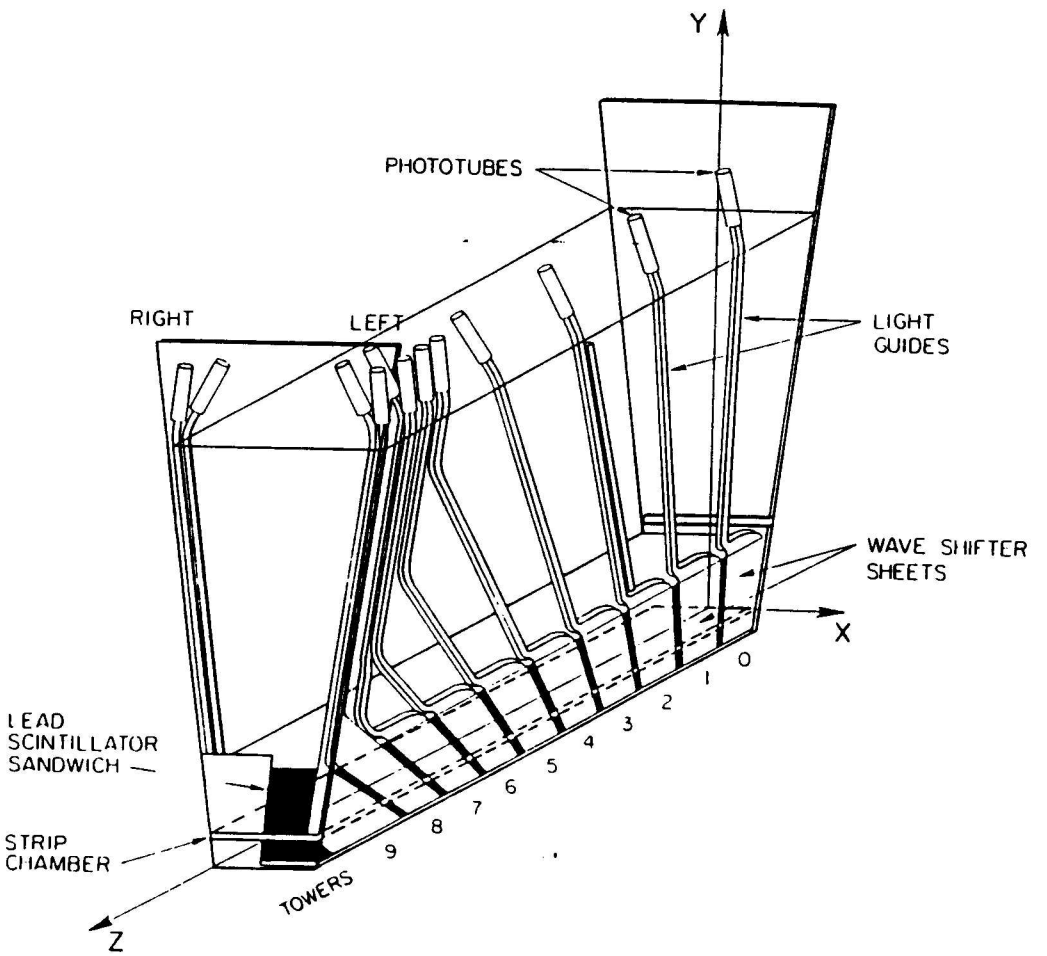

Figure 3.3: A central wedge containing the central electromagnetic shower counter.

Figure 3.3 shows a view of the central electromagnetic shower counter [18]. It is a Pb-scintillator sampling calorimeter 18 radiation lengths thick. The calorimeter is divided into 10 towers each 0.11 units in η and 15° in ϕ . There are 31 layers of 5 mm SCSN-38 polystyrene scintillator interleaved with 3.1 mm lead. To maintain a constant thickness in radiation lengths as the polar angle varies, acrylic is substituted for certain layers of lead. Three mm thick UVA acrylic doped with 30 ppm Y6 wavelength shifters are mounted on each side of the stack. UVA acrylic rod lightguides pass through the hadron calorimeter and connect to 10 ppm Y7 doped transition pieces. The waveshifted light then enters 1.5 in diameter bialkali 10-stage photomultiplier tubes.

The performance of the EM calorimeter was studied at the NW testbeam at Fermilab. Typical light yields are greater than 100 photoelectrons/GeV/tube. The energy resolution for electrons incident on the tower center is given by:

$$\frac{\sigma(\mathrm{E})}{\mathrm{E}} = \frac{13.5\%}{\sqrt{\mathrm{E}\sin\theta}}$$

Figure 3.4 shows the resolution versus energy for a typical tower. In general the response varies depending on where the electron enters the tower. At the testbeam the response across the tower face was mapped by varying the position of the incident electrons, and a detailed response mapping function was fit to the data [19]. Figure 3.5 shows this mapping function. With the tower center response set to 1.0, the map varies between .92 and 1.08.

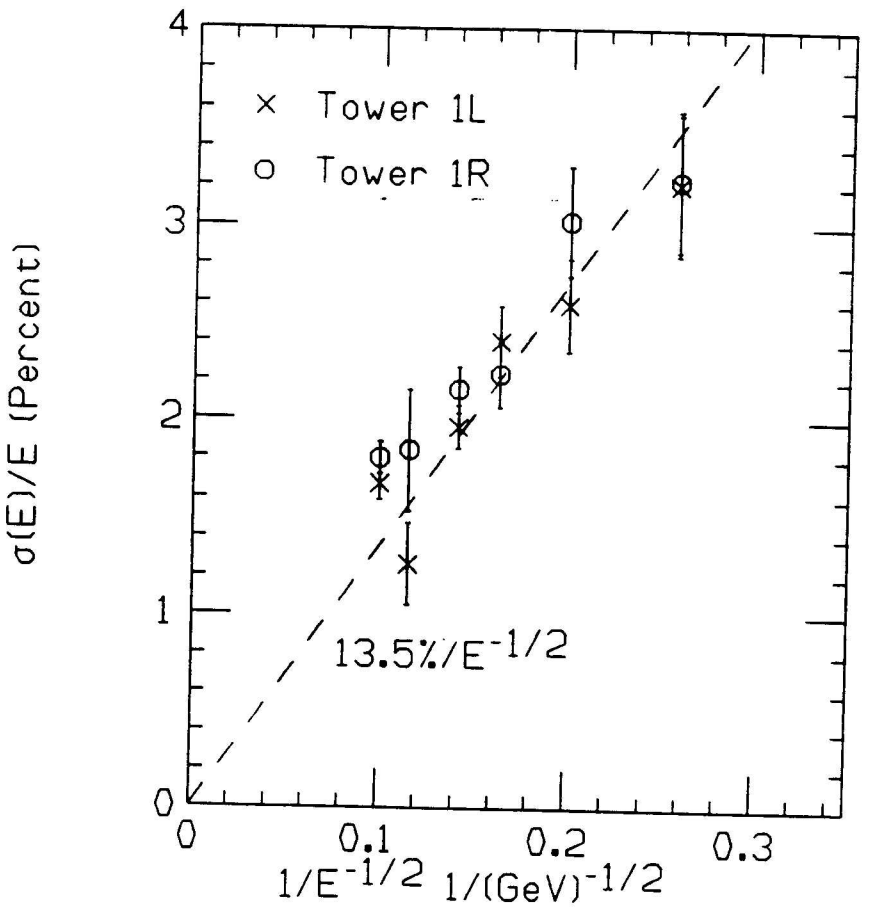

Figure 3.4: Energy resolution for a typical tower in the central EM calorimeter versus electron energy.

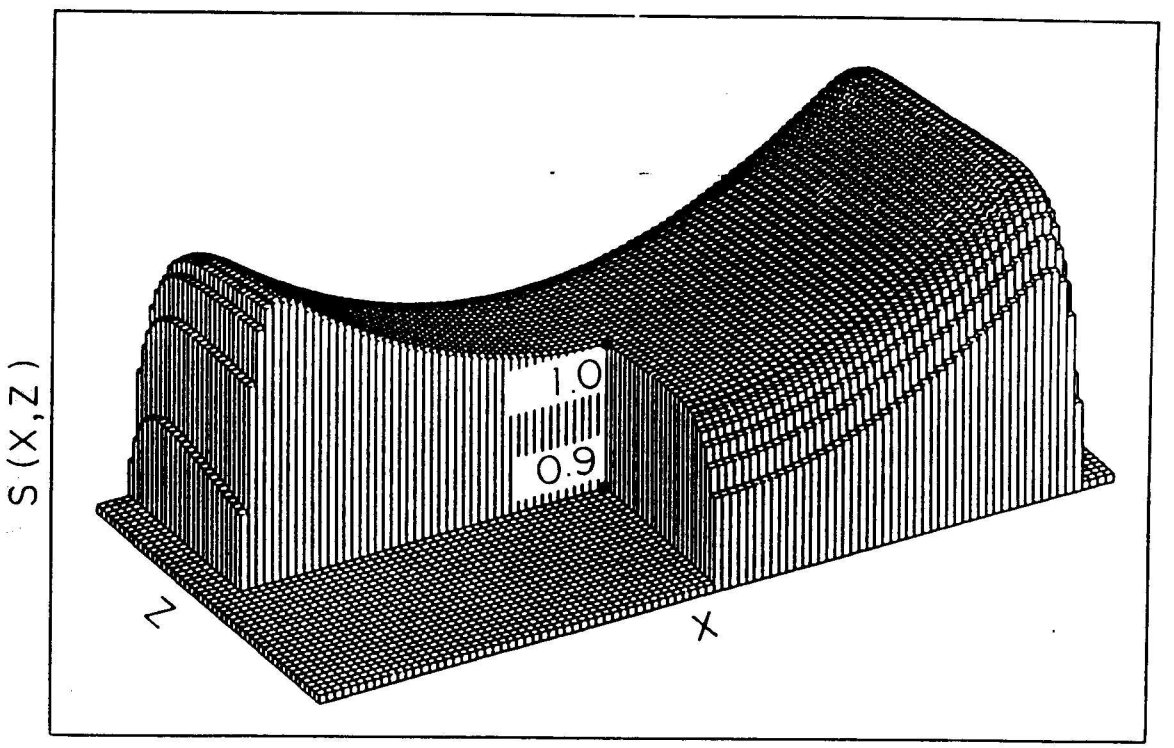

Figure 3.5: The mapping function for a central EM calorimeter tower. The function predicts the calorimeter response based on the position of the incident particle.

Strip chambers are imbedded at shower maximum (5.9 radiation lengths) to help measure the position and the transverse development of the shower. The chambers are wire proportional chambers filled with a 95%/5% mixture of Ar/CO_2 with pulse height readout in 2 directions. Anode wires give shower profiles in ϕ, and cathode strips give profiles along the rapidity axis. The position resolution is typically ± 2 mm for 50 GeV electrons. Figures 3.6 - 3.7 show the relative pulse height and position resolution as a function of beam momentum measured in the testbeam.

The central and endwall hadron calorimeter

The central hadron calorimeter [20] is a steel-scintillator sampling calorimeter stacked immediately behind the EM calorimeter in the wedges. The steel plates are 2.5 cm thick, and the active medium is 1 cm thick sheets of acrylic scintillator doped with 8% naphthalene, 1% butyl-PBD, and 0.01% POPOP. The wavelength shifters are 0.5×1.0 cm^2 rods of acrylic material doped with Laser-dye 481 which form the theta boundaries between towers. The wedge contains 8 hadron towers with the same dimensions as EM towers, and the calorimeter is roughly 5.7 interaction lengths deep.

The endwall calorimeters have a similar arrangement of scintillator, steel, and wavelength shifters. There are 6 endwall towers - 2 of which overlap with central hadron towers, and the total rapidity coverage of the central hadron calorimeter is $-1.3 < \eta < 1.3$. Light yields in the hadron calorimeters are roughly 15 photoelec-

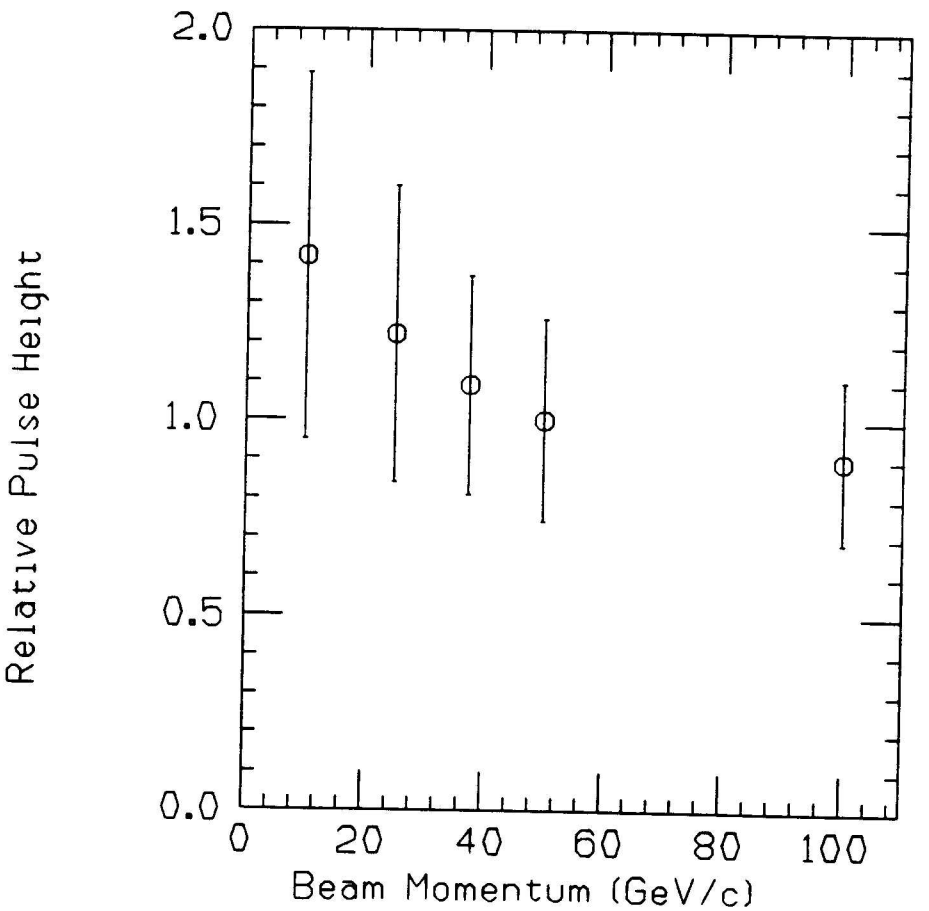

Figure 3.6: Strip chamber pulse height energy dependence. The pulse height is normalized to 1.0 at 50 GeV/c. Error bars correspond to the rms width of the pulse height distributions.

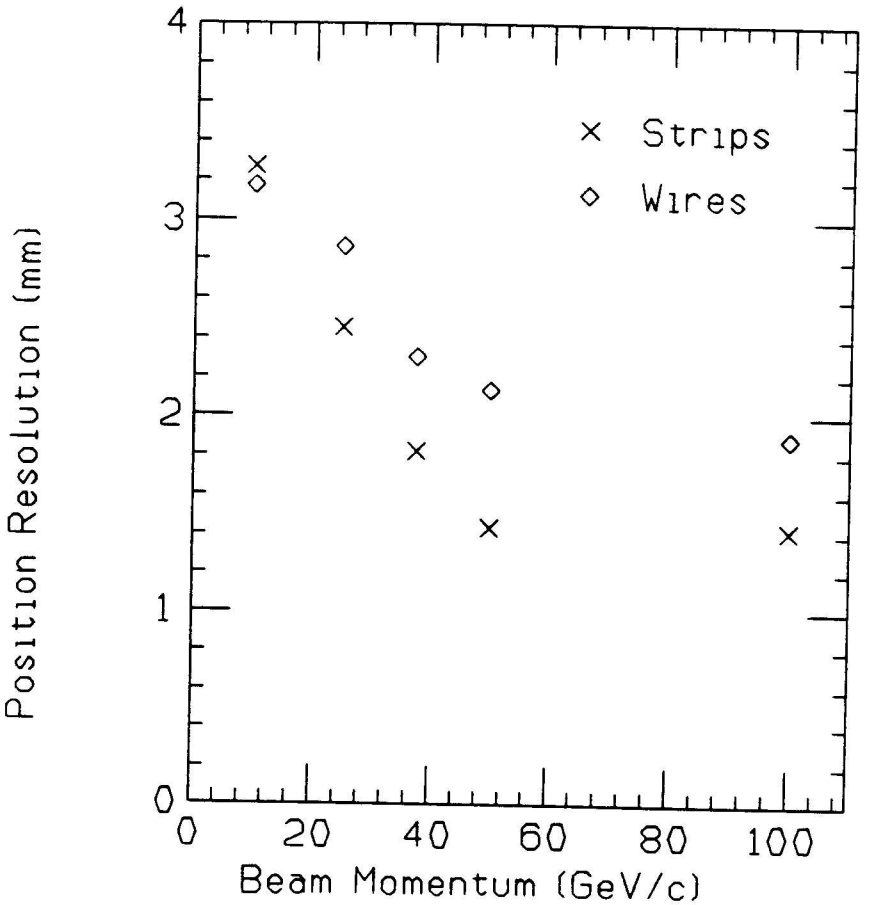

Figure 3.7: Strip chamber position resolution as a function of beam momentum.

trons/Gev/tube. The resolution is given by

$$\frac{\sigma(E)}{E} = \frac{70\%}{\sqrt{E}}$$

The response map for the hadron towers is qualitatively similar to the EM map. Minimum ionizing particles deposit 1.9 GeV on average compared to 0.3 GeV in the EM calorimeter.

Central calibration systems

Accurate calibration of the central calorimeter is critical for many electroweak measurements. All wedges were initially calibrated in the testbeam by measuring the response to 50 GeV electrons or pions and, immediately before or after, measuring the response to a movable, radioactive source. The ratio of these responses was recorded as the calibration constant for every central phototube. Subsequent source measurements monitor changes in the energy response due to movement of the wedges, the magnetic field of the solenoid, decay of scintillator, or other effects. Source calibrations monitor changes over time scales of weeks. To check calibrations over shorter time scales several different systems are used. The EM calorimeter uses 2 redundant light flasher systems – a xenon flash bulb and LEDs. The hadron calorimeter uses a CO_2 laser for both the central and endwall detectors. The physical calibration systems will be described below. More details of the calibration process can be found in the appendix.

Source calibrations for both central calorimeters are made with a ^{137}Cs 3 mCi source permanently mounted on each wedge [21]. The source is attached to a source drive system which consists of a nylon covered steel wire loop, a set of pulleys, and a motor which is remotely controlled. During calibration, the source is driven at a constant rate through tubes mounted between two scintillator layers inside the calorimeter. The photomultiplier currents are read out as the source passes through the calorimeter such that each phototube response shows a characteristic peak (see figure 3.8). Typically calibration of all wedges for either the EM or the hadron calorimeter requires less than an hour, and under proper conditions (no circulating beam) calibration may be done during the data taking period. A similar system is mounted on the endwalls.

There are xenon flasher and LED flasher systems [21] mounted on each wedge. The xenon flasher system simultaneously distributes light from a xenon flash bulb to each waveshifter via quartz light fibers and to 3 monitoring PIN diodes. Since the xenon bulb output varies somewhat from flash to flash, the PIN diodes are used to normalize the photomultiplier response. The LED system distributes light from green LEDs to the photomultiplier transition pieces and reference PIN diodes. The hadron calorimetry uses a CO_2 laser which deposits light into the photomultiplier transition pieces via quartz light fibers and into reference PIN diodes.

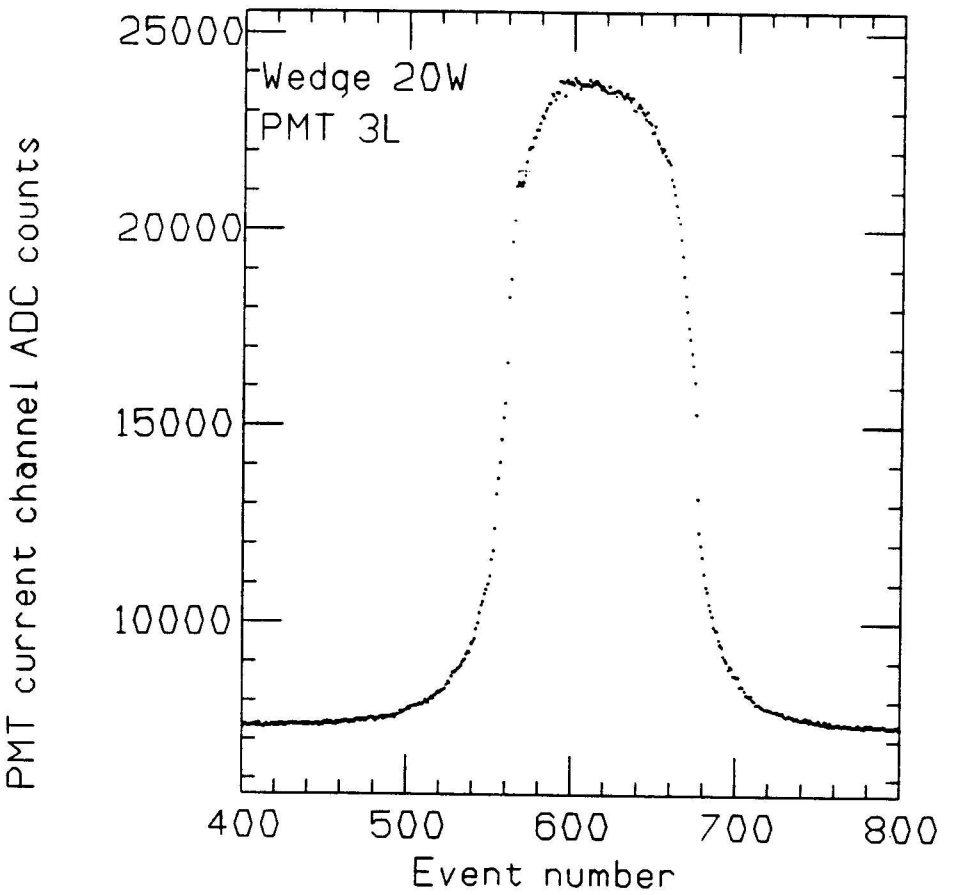

Figure 3.8: Phototube current response as a function of the source position in a central EM calorimeter tower.

3.2.2 Gas Calorimetry

The plug and forward calorimeters use proportional tube chambers. The towers are read out by measuring the induced signals on cathode pads and the charge on anode wires. The absorbers are the same as for the central calorimetry - Pb in the EM calorimeters and steel in the hadron calorimeters. The chambers cover 90° in ϕ (a quadrant) except in the endplug hadron calorimeter where structural supports are placed every 30°.

The plug EM calorimeter [22] includes readout of the cathode pads in 3 depth segments integrating over 3.8, 14.2, and 3.0 radiation lengths. Each wire plane is read out by quadrant yielding a detailed longitudinal shower profile for isolated electrons or photons. The forward EM calorimeter [23] has 2 depth segments each 12 radiation lengths and individual wire plane readout to give shower profiles. The energy resolution in the plug EM calorimeter is:

$$\frac{\sigma}{\mathrm{E}} = \frac{28\%}{\sqrt{\mathrm{E}}}$$

The forward EM calorimeter energy resolution is:

$$\frac{\sigma}{\mathrm{E}} = \frac{25\%}{\sqrt{\mathrm{E}}}$$

The plug [1] and forward hadron calorimeters [24] are read out in 1 depth segment, but they have the wire planes digitized by quadrant to provide additional profile information. The resolution at 50 GeV is roughly 20% for the gas hadronic calorimeters.

System	Inner Layer Coverage	Outer Layer Coverage	Number of (Sense) Wires	Spatial Precision (per hit)
VTPC	-3.5 $< \eta <$ 3.5	-2.6 $< \eta <$ 2.6	3072 wires 3072 pads	200 - 550 μm
CTC	-2.0 $< \eta <$ 2.0	-1.0 $< \eta <$ 1.0	6156	$<$ 200 μm $(R-\phi)$
CDT	-1.0 $< \eta <$ 1.0	-1.0 $< \eta <$ 1.0	2016	200 μm $(R-\phi)$ 2.5 mm (z)
FTC	2.4 $< \eta <$ 4.0	2.4 $< \eta <$ 4.0	3024	150 μm $(R-\phi)$

Table 3.1: Physical parameters for the CDF tracking chambers.

3.3 Tracking

The CDF detector utilizes several tracking devices to give tracking information over the full rapidity region subtended by the calorimeters. A superconducting solenoidal coil which produces a 15 kG magnetic field in the axial (beam) direction allows accurate momentum determination for charged tracks in the central region. The central region uses the central tracking chamber (CTC) with additional information from central drift tubes (CDT). The forward tracking chamber (FTC) tracks in the far forward region, and the vertex time projection chamber (VTPC) enables the determination of the event vertex and gives intermediate tracking information. Physical

parameters for the tracking chambers are shown in table 3.1

The tracking systems provide many useful functions for electron analysis. The electron trigger or offline code may require a high p_T track pointing at an electromagnetic cluster in the calorimeter. Reconstructed tracks in the VTPC are used to locate the event vertex and reject events with beam–gas interactions or multiple beam–beam vertices. A significant background to electrons is the overlap of a charged hadronic particle and a neutral electromagnetic particle such as a γ or a π^0. By demanding that the ratio of the energy in the calorimeter to the momentum of the track pointing at the cluster, E/p, be near 1.0, this background may be effectively reduced. Matching the position of the CTC track with cluster position information available in the calorimeter can further reduce the background. Photon conversions can fake prompt electrons. The conversion background can be reduced by using VTPC hits to reconstruct secondary vertices and searching for oppositely charged CTC tracks with negligible invariant mass.

3.3.1 Vertex Time Projection Chamber

Immediately outside the beampipe, there are 8 VTPC modules [25] each containing 8 octants in ϕ which give position information down to 3.5° from the beamline. The 8 modules extend 2.8 meters along the beamline to allow event vertex reconstruction over the full interaction region ($\sigma(z) \sim 30$ cm). The chamber contains 16 sense

wires per octant for track reconstruction in the $R - z$ plane, where R is the radial distance from the beam, and pads to measure coordinates in the $R - \phi$ plane. The z resolution varies between 200 and 550 μm depending on the drift distance, and the $R - \phi$ resolution is roughly 350-450 μm.

Since all particles detected in the calorimeters and other tracking chambers pass through the beam pipe and the VTPC, an effort was made to keep the mass of these systems as low as possible. Larger masses in these systems decrease tracking accuracy due to multiple scattering and increase the γ conversion probability. The beam pipe consists of a Be tube with a wall thickness of 500 μm. Figure 3.9 shows the number of radiation lengths of material versus polar angle for critical detector components.

3.3.2 Central Tracking Chamber

The CTC [26] is a cylindrical drift chamber which provides momentum and position information on tracks in the region $30° < \theta < 150°$. The chamber contains 84 layers of sense wires organized into 9 superlayers with five superlayers containing 12 axial sense wires and the other 4 superlayers containing 6 stereo sense wires tilted 3° from the beam direction. Figure 3.10 shows an $R-\phi$ view of the chamber layout. The chamber uses a 50%/50% mixture of argon/ethane gas. The spatial precision is < 250 μm in the $R - \phi$ plane, and the CTC momentum resolution is given by $\Delta p/p = .002$ p.

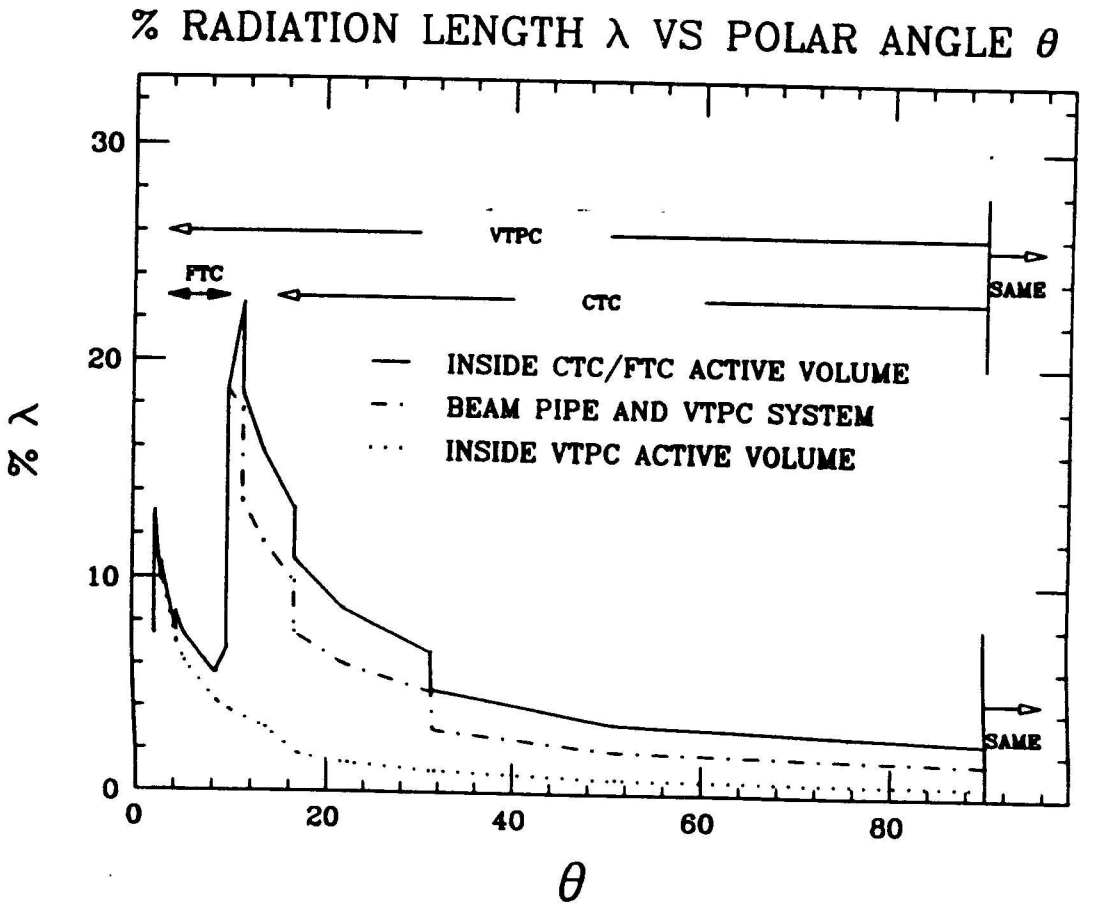

Figure 3.9: Number of radiation lengths of material versus polar angle for the CDF detector.

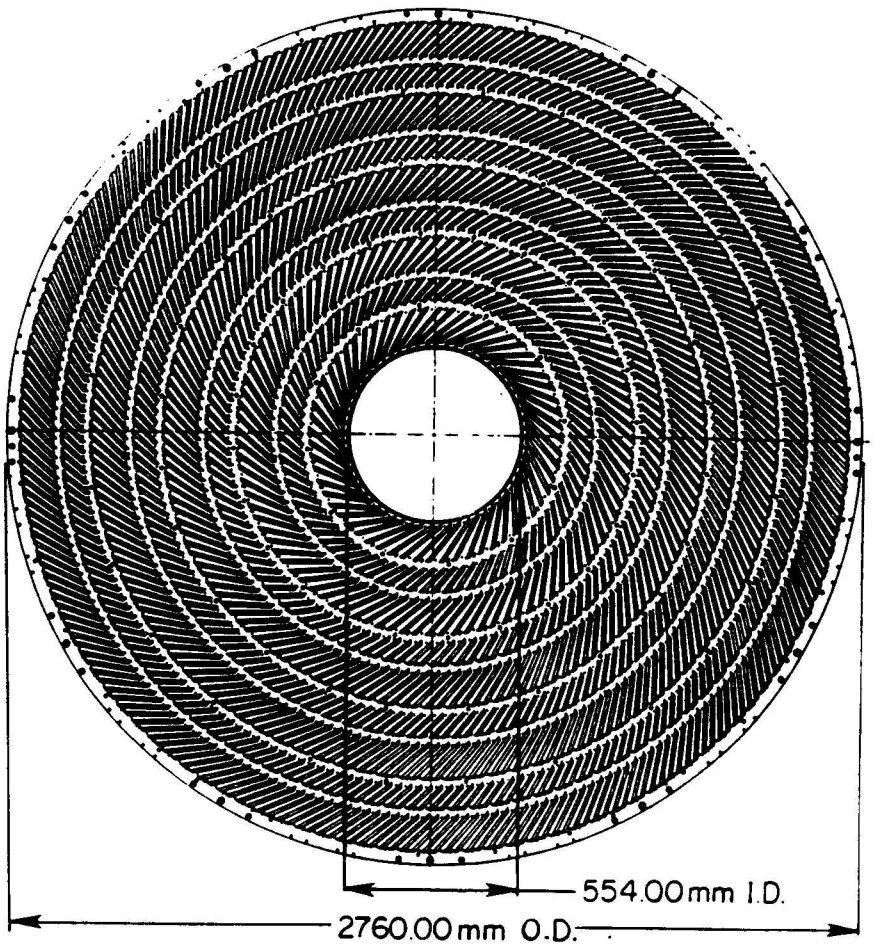

Figure 3.10: An $R-\phi$ view of the CTC layout.

3.3.3 Central Drift Tubes

The central drift tubes, CDT, [27] aid tracking by providing additional $R-\phi$ measurements and more precise z measurements. The system consists of 3 layers of 1.27 cm diameter 3 m long tubes mounted on the outside of the CTC. Measurements of drift times give $R-\phi$ information and charge division gives z information. An ^{55}Fe source is located near each end of the drift tubes for charge division calibration. The tubes operate in limited streamer mode and use a 49.25%/49.25%/1.5% mixture of argon/ethane/ isoproponol. Typical resolutions are 200 μm in $R-\phi$ and 2.5 mm in z.

3.3.4 Forward Tracking Chamber

The FTC [28] is a radial wire drift chamber which covers the angular region $2^\circ - 10^\circ$. The chamber consists of 72 cells containing radial planes of anode wires alternating with planes of cathode strips. The planes are tilted 2° relative to the beam axis so left-right ambiguities may be resolved. The anode planes have 21 sense wires strung approximately along the radial direction. Four of these sense wires are instrumented for charge division in order to get a 3-dimensional coordinate.

The FTC operates in the saturated avalanche region with a 50%/50% mix of argon/ethane gas. The chamber has achieved a resolution of $\sigma = 145$ μm per hit and a 2-track resolution of about 2 mm in the $\phi - z$ plane.

3.4 Muon Detection

Muon detection in CDF consists of 2 systems - the central muon chambers [29] and the forward-backward muon system [30]. Each central wedge contains 3 muon chambers which sit outside the hadron calorimeter, and cover the angular region $56° < \theta < 124°$. The chambers run in limited streamer mode and contain a 49.9%/ 49.9%/0.2% mixture of argon/ethane/ethyl alcohol. There are 4 wire layers which measure the azimuthal position to an accuracy of 250 μm per layer and through charge division measure the z position to 1.2 mm per layer.

The forward/backward muon spectrometers each consist of two 1 meter thick steel toroids sandwiched between 3 sets of drift chambers. The toroids produce a magnetic field of 20 Kgauss at the inner radius and 1.6 Kgauss at the outer radius. The chambers measure the muon trajectory to 5° in ϕ and 200 μm in R. The spectrometers cover the angular region 3° to 16° and the momentum resolution is 13% for tracks with $p_T > 8$ GeV.

3.5 Trigger counters

A plane of scintillation counters, called beam-beam counters (BBC), positioned in front of the forward and backward calorimeters provide luminosity monitoring and act as part of the hardware trigger. There are 16 counters, mounted in a rectangular pattern around the beam pipe, which cover the angular region from 0.32° to 4.47°

$(3.24 < \eta < 5.90)$. Timing signals from the 2 photomultiplier tubes connected to each counter pass through a mean-timer to a Fastbus latch. In order to determine if a real beam-beam interaction occured, there are 2 gates – a beam-halo gate and a beam-beam gate. The beam-halo gate is 100 ns wide and closes 10 ns before the beam crossing time (30 ns before outgoing particles reach the counters). The beam-beam gate is 15 ns wide and centered 20 ns after the beam crossing time (when the outgoing particles reach the counters). The trigger requires hits in at least one counter on each side of the interaction region during the beam-beam gate and no beam-halo hits. The counters have a timing resolution of < 200 psec. The counters give the best measurement of the interaction time and yield a crude estimate of the vertex position.

3.6 Data acquisition and Trigger hardware

The CDF detector has roughly 100,000 electronics channels with 60,000 in the calorimeters and almost all the rest for tracking. The calorimeters requires a very large dynamic range extending from a few MeV to several hundred GeV, and a custom-built data acquisition system [31] was developed to read out the calorimeters. This system consists of a crate-based analog front-end device called the RABBIT crate [32] which is read out by intelligent scanners called MXs. The tracking data is read out by a second intelligent scanner called SSPs [33].

At the Fermilab Tevatron design luminosity of $10^{30}cm^{-2}s^{-1}$ the event rate is 50 kHz. The CDF trigger system [34] was designed to reduce this rate to the maximum event tape writing rate of roughly 1 Hz. The trigger is a 4 level system with the BBCs serving as level 0, hardware decision logic serving as levels 1 and 2, and finally software modules which make decisions based on various event properties as level 3. Since the luminosity during the 1987 run was about a factor of 10 under the design and the trigger was unfinished, levels 0 and 1 were combined and no other trigger levels were utilized.

The hardware trigger exploits the projective geometry of the calorimeters. A trigger tower is $0.2 \times 15^\circ$ $(\Delta\eta \times \Delta\phi)$ with EM and hadronic energy stored separately. The photomultiplier tube signals are brought from the RABBIT crate to the trigger electronics on cables that bypass the data acquisition hardware and then are weighted by $\sin\theta$ to form the transverse energy, E_T . The voltage levels remain on the cables until a level 1 decision is made. Individual tower energies are compared with programmable threshold levels, and all towers passing the threshold are summed to form the total E_T . Decisions can be made based on individual tower energies, sum E_T , or both.

Chapter 4

Event Selection

4.1 Introduction

Strategies to search for W bosons depend on W production and decay properties. This thesis discusses only events where the W decays leptonically into an electron and neutrino. Since neutrinos are not detected, a prominent event property is the presence of missing transverse energy, $\not\!\!E_T$. The electron will deposit energy in the calorimeter, and because the W has a relatively high mass, the electron p_T is usually large. Aside from the neutrino and electron, there are other particles created in the $p\bar{p}$ interaction which we will collectively refer to as the "underlying event". The vast majority of these particles have very little energy, and their numbers are small enough that they contribute little to the event signature. The electron then is isolated – there is little energy in the surrounding calorimeter towers. In general, search strategies for W bosons require events to have a high p_T electron candidate and significant $\not\!\!E_T$.

W bosons can be produced in higher order processes where the W is produced

with a gluon or quark. In this case there is a jet added to the event signature. Since the p_T of the W tends to be small compared to the W mass, the electron receives only a small boost, and the electron and jet positions are not highly correlated. The event still has $\not\!\!E_T$ due to the neutrino, and the electron has a high probability of being isolated. There is some chance that the jet and the electron enter the calorimeter back-to-back in ϕ, and the event has a topology similar to 2 jet events. This possibility becomes important when considering certain cuts to eliminate background due to 2 jet events.

The CDF collaboration used two separate strategies to search for W candidates. In one strategy, called the $\not\!\!E_T$ analysis, strict $\not\!\!E_T$ cuts are used to get a small sample of interesting events and subsequent weak electron cuts are used to find the final W candidates. The other strategy, called the electron analysis, used the opposite approach of imposing strict electron cuts to produce a small, interesting sample and later used weak $\not\!\!E_T$ cuts to find W bosons. This thesis describes only the electron analysis.

A brief overview of the electron analysis will be given here, with the details presented below. After selecting electromagnetic clusters with the hardware trigger, there were 3 passes through software cuts. The first pass utilized an electron finding algorithm which used loose cuts to select a set of inclusive electron candidates based on calorimeter response. Electrons deposit over 95% of their energy in the EM

calorimeter with little hadronic leakage. Requiring the hadronic energy fraction to be small significantly reduces the number of jets entering the electron sample. The second pass imposed much stricter cuts to find high E_T isolated electrons. A tracking requirement was added, and the electron candidate was required to be isolated in the calorimeter. The third and final pass used global event properties. This pass included a $\not\!\!E_T$ cut and a restriction on jets to reduce the multijet background.

4.2 Triggers

The CDF experiment ran with several triggers during the 1987 data taking period, but only two are relevant to this analysis. The beam-beam counters served as both a minimum bias trigger and luminosity monitor. The "electron" trigger selected events with significant electromagnetic energy deposited in the calorimeter.

4.2.1 Minimum Bias Trigger and Luminosity

The minimum bias trigger required at least one hit in both the east and west beam-beam counters. These triggers were used to calculate the luminosity on a run by run basis. The integrated luminosity is given by the following equation:

$$\int \mathcal{L} dt = \frac{\text{Number of BBC triggers}}{\sigma_{BBC}} \tag{4.1}$$

where σ_{BBC} is the part of the total cross section that the BBC can detect. During the 1987 run, we were unable to measure the total $p\bar{p}$ cross section, and therefore, we

could not directly calculate the BBC cross section.

To estimate $\sigma_{\rm BBC}$ [35] we divided the total cross section into its various components – elastic, diffractive, and hard core (i.e. inelastic minus single and double diffractive), and determined these values by extrapolating from measurements at lower energies. We then used Monte Carlo simulations to calculate the BBC efficiency for the cross section components. The total cross section may be extrapolated from lower energies by assuming that the cross section either evolves proportionally to $\log^2 s$ or is asymptotically constant at high energies but locally proportional to $\log^2 s$ [36]. Taking the mean of various predictions we estimate:

$$\sigma_{tot} = 77 \pm 6\ mb$$

Using measurements of the ratio σ_{el}/σ_{tot} from UA4 [37] and UA5 [38] at lower center of mass energies, we extrapolate to estimate $\sigma_{el}/\sigma_{tot} = 0.23 \pm 0.01$ at $\sqrt{s} =$ 1.8 TeV. Then

$$\sigma_{el} = 17.6 \pm 1.6\ mb$$

We can then calculate the inelastic cross section as:

$$\sigma_{in} = \sigma_{tot} - \sigma_{el} = 59.4 \pm 6.2\ mb$$

Extrapolating the single and double diffractive cross sections from lower energies entails significant error; however, these contribute relatively little to σ_{BBC}. We estimate:

$$\sigma_{sd} = 15.0 \pm 5.0\ mb$$

$$\sigma_{dd} = 4.2 \pm 1.0\ mb$$

We can then calculate the hard core, σ_o, contribution:

$$\sigma_o = \sigma_{in} - \sigma_{sd} - \sigma_{dd} = 40.2 \pm 6.9\ mb$$

Using the Monte Carlo efficiencies, we find

$$\sigma_{BBC} = 0.17\sigma_{sd} + 0.71\sigma_{dd} + 0.96\sigma_o = 44.1 \pm 6.7\ mb$$

From this cross section we calculated the integrated luminosity of the runs used in the W analysis to be 25.3 $\pm$ 3.8 nb^{-1}. The error in the BBC cross section is 15% and dominates the systematic error in the W cross section. In determining errors from other terms in the cross section calculation we will often be conservative and overestimate since the effect on the overall error is negligible.

4.2.2 Electron Trigger

The other relevant trigger is the "electron" trigger which consisted of a single trigger tower threshold combined with a sum E_T threshold (see section 3.6). The single tower threshold required that there be at least one trigger tower with EM E_T greater than a minimum level. The sum E_T threshold summed the EM E_T for all the trigger towers. The trigger thresholds varied during the run due primarily to changing luminosity conditions. Table 4.1 lists the different triggers, their thresholds, and their percentage of the total luminosity.

Trigger Type	Single Tower E_T	Sum Et	% Total Luminosity
Buffet low	7.4	7.0	2.2
Buffet medium	9.0	9.0	12.4
Buffet high	10.0	9.6	24.2
Buffet burn	12	11.6	29.1
Buffet 30	5.0	15.0	32.1

Table 4.1: Triggers used during the 1987 run. Listed are the electron trigger single tower thresholds, the sum E_T , and the percentage of the total luminosity for each trigger type. The term Buffet refers to a mix of various triggers including the electron trigger.

4.3 Electron Cluster Algorithm

All events which passed the electromagnetic trigger cuts were run through offline code to look for electrons. The offline code used a simple electron cluster algorithm to select events with energy deposition in the calorimetry that was consistent with electron testbeam data. Electron signatures in the central, plug, and forward calorimeters differ, primarily in the number of towers needed to contain the shower; therefore, the cluster algorithm varies depending on where the cluster is found.

Electrons deposit energy in matter in a well understood process [39]. All the electromagnetic shower counters are relatively deep in number of radiation lengths so electrons are expected to deposit only a few percent of their energy in the hadron calorimeters. Electromagnetic showers are well contained in a single tower, and only

particles entering the calorimeter near a tower border will deposit appreciable energy in an adjacent tower.

The ratio of energy deposited in the hadron calorimeter to that deposited in the EM calorimeter for 50 GeV testbeam electrons incident on tower center is shown in figure 4.1. Figure 4.2 show transverse energy leakage across the ϕ boundary. Since wedge boundaries physically separate towers adjacent in ϕ, electrons in the central calorimeter do not deposit energy into 2 such towers unless they are incident very near the tower border. Electrons are more likely to deposit energy in towers adjacent in θ because there are no physical boundaries in this direction. Central electron clusters therefore consist of electromagnetic energy deposition in one or two towers from the same wedge.

The clustering algorithm searched all the electromagnetic towers to find potential seed towers where seed towers were required to have $>$ 3 GeV E_T . These seed towers were then sorted such that clustering would begin with the highest energy tower and proceed in descending order. Once a tower (the parent) was selected, all its neighboring towers (daughters) were tested to see if they should be included in the cluster. A daughter tower must have $>$ 0.1 GeV E_T , and the ratio of the daughter tower E_T to the parent tower E_T must be less than 1 in order to include the daughter in the cluster. The parent - daughter ratio requirement insures that 2 overlapping clusters may be resolved rather than merged into one cluster. Clustering

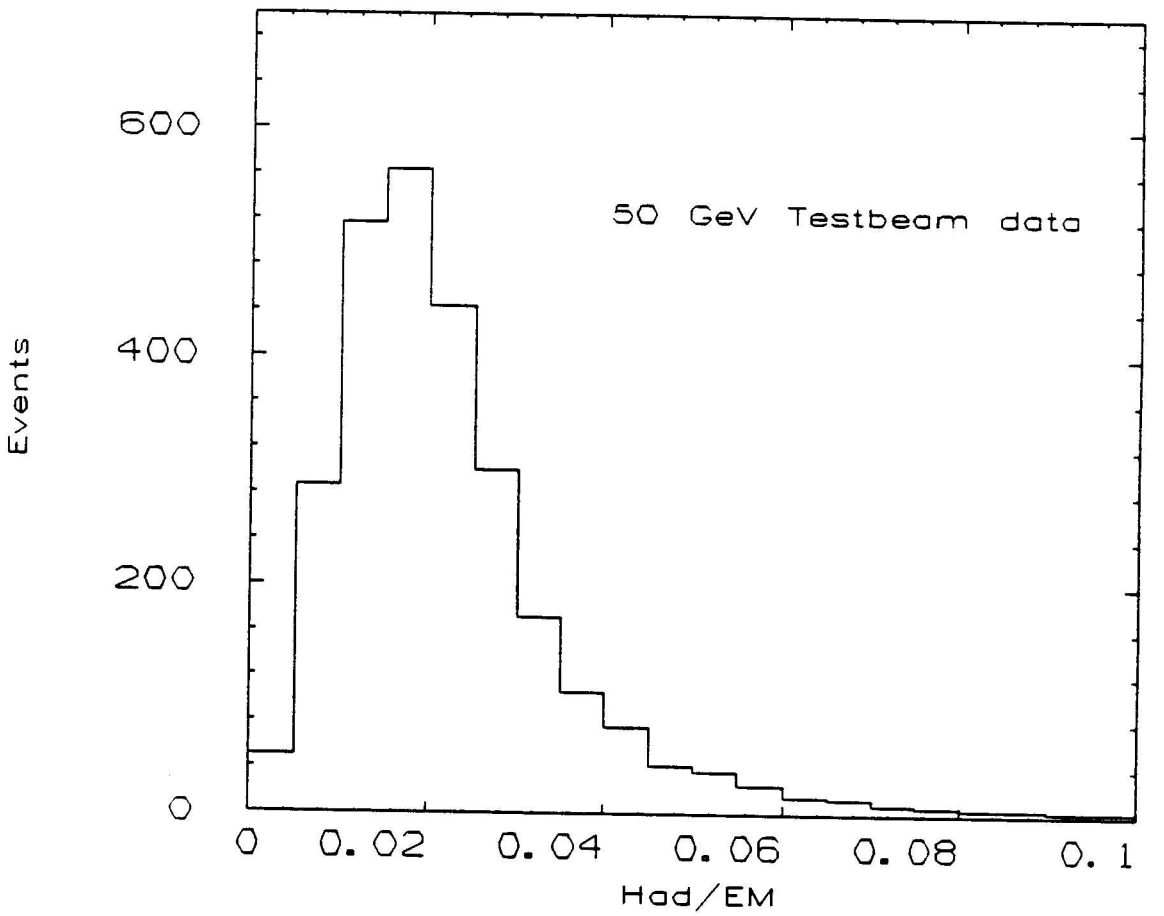

Figure 4.1: Distribution of the ratio of energy deposited in the hadronic calorimeter to the energy deposited in the EM calorimeter for 50 GeV testbeam electrons.

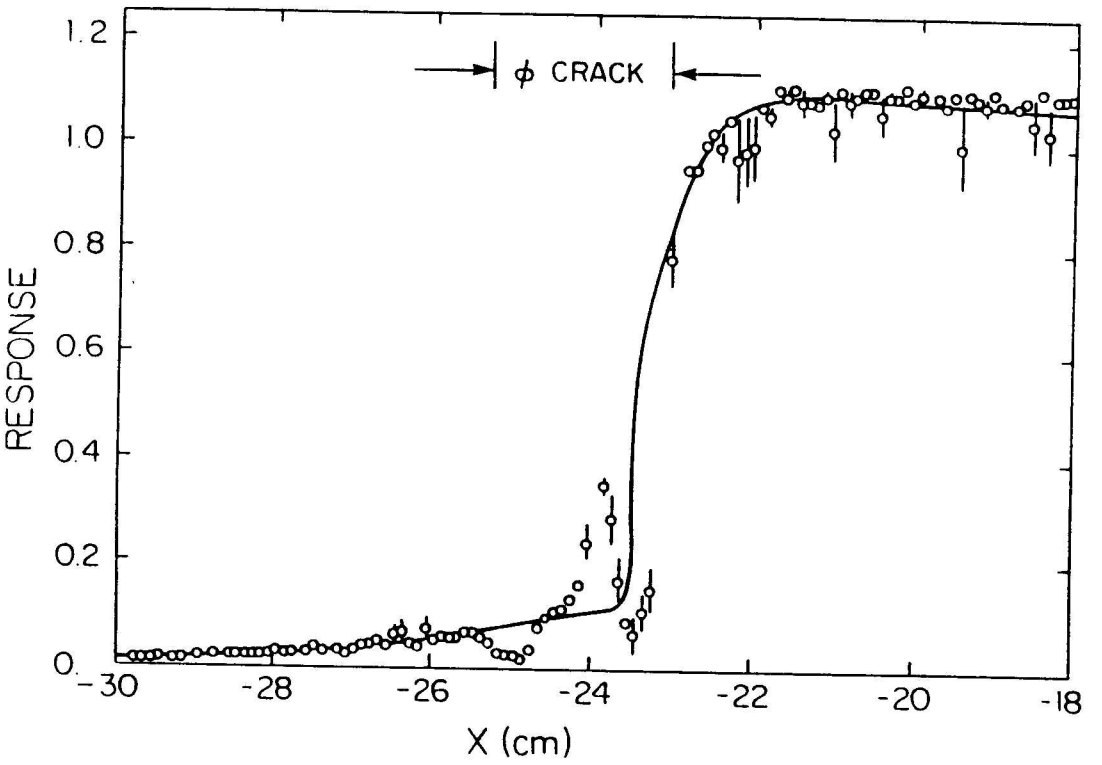

Figure 4.2: Transverse Energy leakage across the ϕ boundary from testbeam measurements. The inactive region between two wedges (ϕ crack) is indicated. Electrons entering the active region of a given wedge deposit very little energy in adjacent wedges.

continued by checking all possible daughter towers until the maximum cluster size was exceeded. This size varied for the different calorimeters essentially because the physical tower size varies. The maximum cluster size for the various calorimeters is– central: 3 towers η × 1 tower ϕ, plug: 5 towers η × 5 towers ϕ, forward: 7 towers η × 7 towers ϕ. Clusters were required to pass 2 final cuts. The summed EM E_T for all the cluster towers must exceed 5 GeV. Finally, the ratio of the total hadron cluster energy to the EM cluster energy, Had/EM, must be less than 0.1. All events with electron candidates satisfying these requirements were written to Electron Data Summary Tapes (DSTs). We wrote roughly 140 tapes with 4×10^5 events.

4.4 High E_T isolated Electron Cuts

We then used the kinematics of W decay and electron detection properties to impose further selection criteria and reduce the sample. The following 5 cuts produced a sample of high E_T isolated central electron candidates.

4.4.1 Calorimeter Cuts

Rapidity

Electrons were required to enter the central EM calorimetry which covers the region $-1.1 < \eta < 1.1$. Tower 9 (the last tower on the 45 degree side of the central wedges - see figure 3.3) has a profile significantly different from the other towers, and the

electron response is affected especially in the parameter Had/EM. Since the response is not understood as well as the other tower responses, electrons with their seed tower in tower 9 were dropped from the sample. The rapidity acceptance then becomes $-1.0 < \eta < 1.0$.

Transverse Energy

Light produced in the scintillator by the showering electron may be absorbed before reaching the wavelength shifter. The calorimeter response may then differ for electrons which deposit the same amount of energy in the scintillator because the electron position in the tower varies. Using testbeam electrons the detector response was mapped out across the face of the towers to produce a response map (see figure refmapping). Knowing the event vertex from the VTPC and the electron cluster centroid from strip chamber readings, the electron trajectory may be calculated, and the response map can then be used to correct the cluster E_T . Electron clusters were required to have $E_T > 15$ GeV. This value is both high enough so that the all electron triggers were almost fully efficient and low enough so the acceptance for W decays is large. Figure 4.3 shows the Monte Carlo generated E_T spectrum for central electrons from W decays. A cut at $E_T > 15$GeV accepts roughly 96% of central W bosons.

Had/EM

The Had/EM ratio was tightened to require clusters to have Had/EM < 0.05.

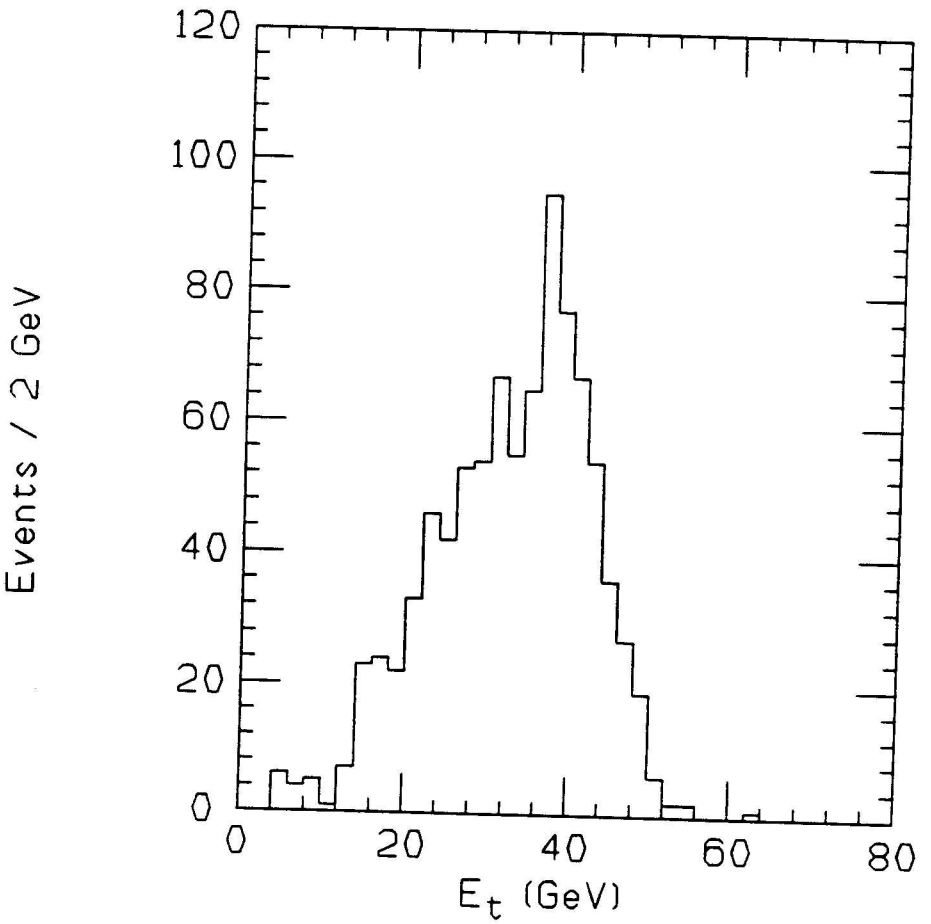

Figure 4.3: Monte Carlo electron E_T spectrum from W decays with an electron cluster in the central detector.

Isolation

Since in general W decays produce electrons with very little activity near them, we imposed an isolation requirement on W candidates. The CDF calorimeters are highly segmented and can localize electron showers. This segmentation can be used to detect the energy deposited in a relatively small region of $\eta - \phi$ space around the electron and yield a good measure of how isolated the electron is. To specify the region around the electron cluster, we used a cone in $\eta - \phi$ space. Then isolation is defined as

$$\text{Isolation} = \frac{\text{E}_\text{T}(\text{Cone}) - \text{E}_\text{T}(\text{cluster})}{\text{E}_\text{T}(\text{cluster})} \tag{4.2}$$

where E_T (Cone) is the sum of the E_T within the cone and E_T (cluster) is the electron cluster E_T . The cone radius, R, was 0.4 where R is defined as

$$R = \sqrt{(\Delta\eta)^2 + (\Delta\phi)^2} \tag{4.3}$$

and ϕ is measured in radians. Isolation is required to be less than 0.1. The number of towers included in the isolation cone varies depending on exactly where energy is deposited in the various towers of the cluster and its neighboring towers, but the number is usually 12-14 in the central calorimeter.

4.4.2 Tracking

The above cuts use calorimetry to select electron candidates. The central tracking chamber gives excellent position and momentum information for charged particles

over the rapidity region $-1.0 < \eta < 1.0$; consequently, it is useful in detecting high momentum electrons by finding high p_T tracks and associating them with electromagnetic clusters in the calorimetry. The offline tracking code searched for high p_T tracks which extrapolate to any of the electron cluster towers. Tracks were required to have $p_T > 2$GeV. If such a track was found, we formed the ratio of the E_T of the electron cluster to the p_T of the track (E/p) . We required E/p < 2.0 . These isolated, high E_T electron cuts selected 137 events. The vast majority of all events cut have no track with $p_T > 2$ GeV (2967 out of 3753). Figures 4.4- 4.5 show the distribution of the parameters Had/EM, E/p, isolation, and E_T for these events.

4.5 Global Event Cuts

The cuts in the previous section have used properties of the electron or the immediately surrounding region. This section will discuss cuts which look at properties of the whole event. As mentioned earlier W events should have relatively little activity opposite the electron cluster because the momentum of the electron is not balanced by a detected particle.

4.5.1 Dijet Veto

The largest background to $W \rightarrow e\nu$ events are multijet events where one jet fakes an electron and another jet is mismeasured in the calorimeter causing an apparent

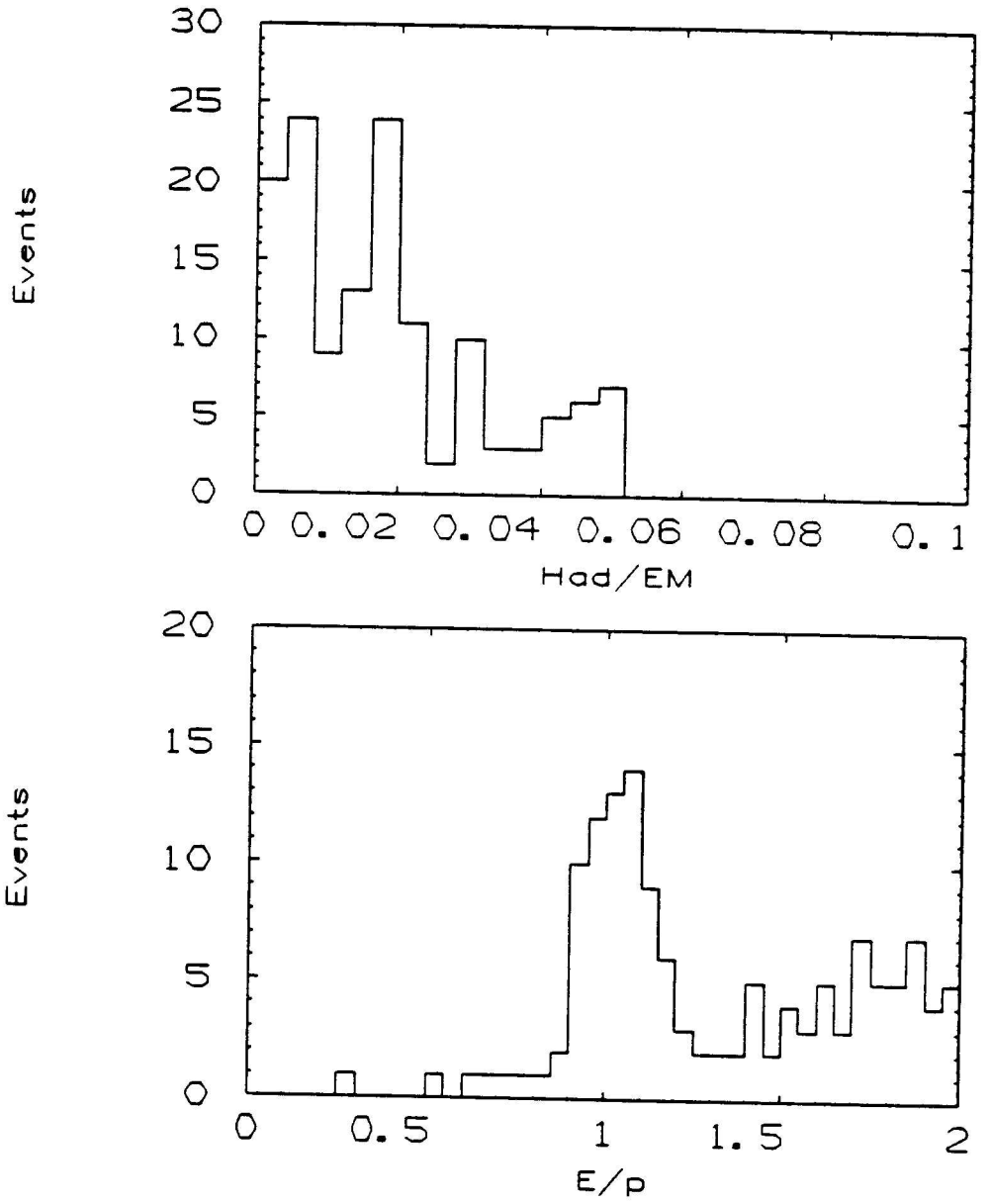

Figure 4.4: Distribution of Had/EM (top) and E/p (bottom) for events passing high p_T , isolated electron cuts.

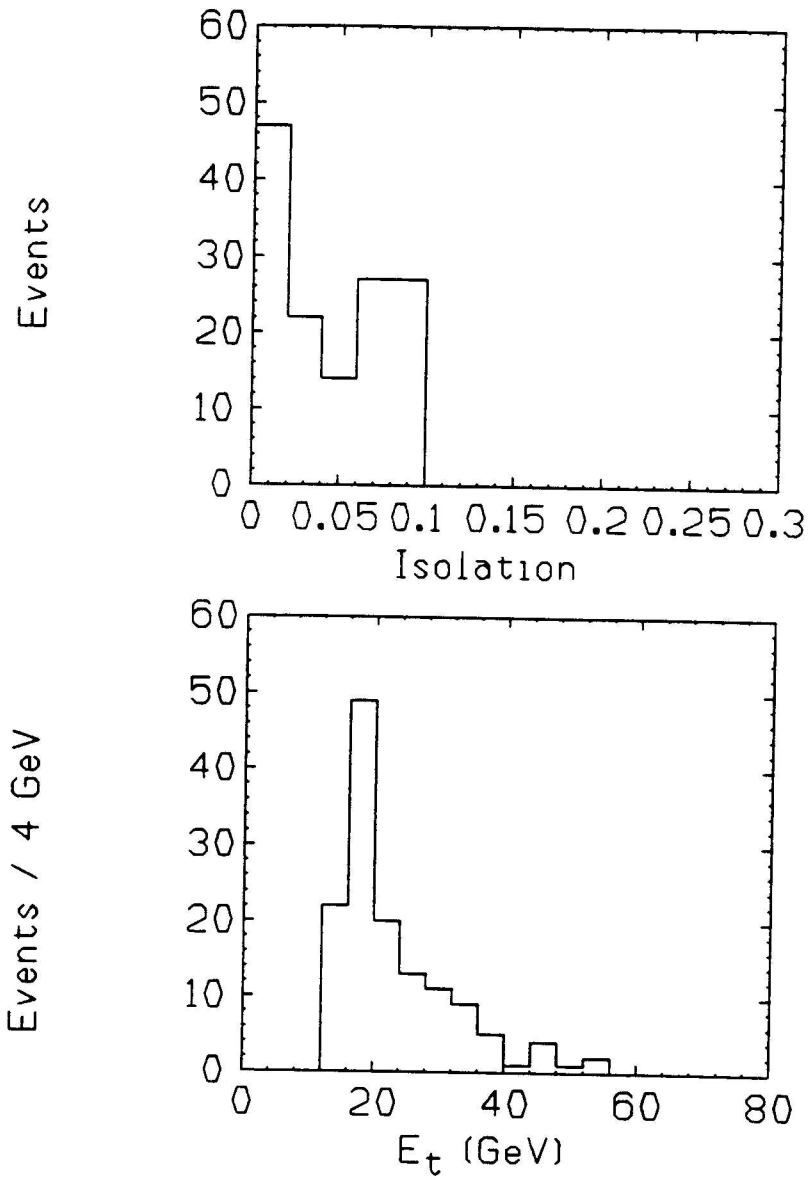

Figure 4.5: Distribution of isolation (top) and E_T (bottom) for events passing the high p_T , isolated electron cuts.

momentum imbalance. Jets fail the electron cuts for several reasons. Jets are primarily hadronic particles such as pions which tend to deposit significant energy in the hadronic calorimeter and, thus, fail the Had/EM cut. Jet fragmentation tends to produce many particles such that no single particle carries over 50% of the momentum; therefore, E/p will be greater than 2.0. Finally, jets tend not to be contained in the dimensions of an electron cluster so there will be excessive energy in the isolation cone. Hard fragmentation does occur, however, so occasionally a single charged particle carries the vast majority of the jet momentum. If this fraction is high enough, the jet may be contained in a small number of towers, and energy in the isolation cone may be small. Charged pions can interact via charge exchange, and if this interaction occurs early enough in the electromagnetic calorimeter, a shower similar to electron showers can result. The probability that all these requirements are met by jets is very small; however, the jet cross section is enormous and leads to significant background.

In theory any multijet event can contribute to the W background, but the cross section for 2 jet events dominates the other cross sections by a factor of at least α_s. We therefore reduced the jet background by using a "dijet" veto. In 2 jet events we expect another jet roughly 180° in ϕ from the fake electron. We ran a jet cluster algorithm [40] to find all potential jets, and required that there be no cluster with $E_T > 5$ GeV within $\pm$ 30° in ϕ opposite the electron cluster. This cut reduces the sample to 61 events. Figure 4.6 is a 2-dimensional plot of $\not\!\!E_T$ versus E_T for these

events.

4.5.2 Missing E_T

Since $W \rightarrow e\nu$ events have a neutrino which is not detected, there should be significant missing energy in the calorimeters. The final cut required events to exhibit this large missing energy. We define $\not\!\!E_T$ as the vector sum of the E_T corrected for the position of the vertex over all towers in the rapidity range $-3.6 < \eta < 3.6$. The calorimeters did not have complete azimuthal coverage in the region $| \eta | > 3.6$ due to the intrusion of low-beta quadrupole magnets. Calorimeter towers were included in the sum if their energy exceeded the threshold values of 0.1 GeV (central EM), 0.2 GeV (central hadron), 0.5 GeV (plug and forward EM), and 0.8 GeV (forward hadron).

Since noise and detector inefficiencies change the true event $\not\!\!E_T$, the $\not\!\!E_T$ calculation must include corrections. There are several effects which can significantly change the $\not\!\!E_T$. Calorimeter electronics channels may be "hot" (always measuring energy) or "dead" (always off), thus adding or subtracting energy from the event. Individual "hot" channels were removed by offline routines, but clusters of "hot" channels were much harder to identify. At Fermilab, beam is accelerated in the "main ring" and then injected into the Tevatron for collisions. The main ring passes above the CDF detector, and occasional spray from this beam entered the detector and deposited energy in the calorimeter. Large effects such as these typically show up in many

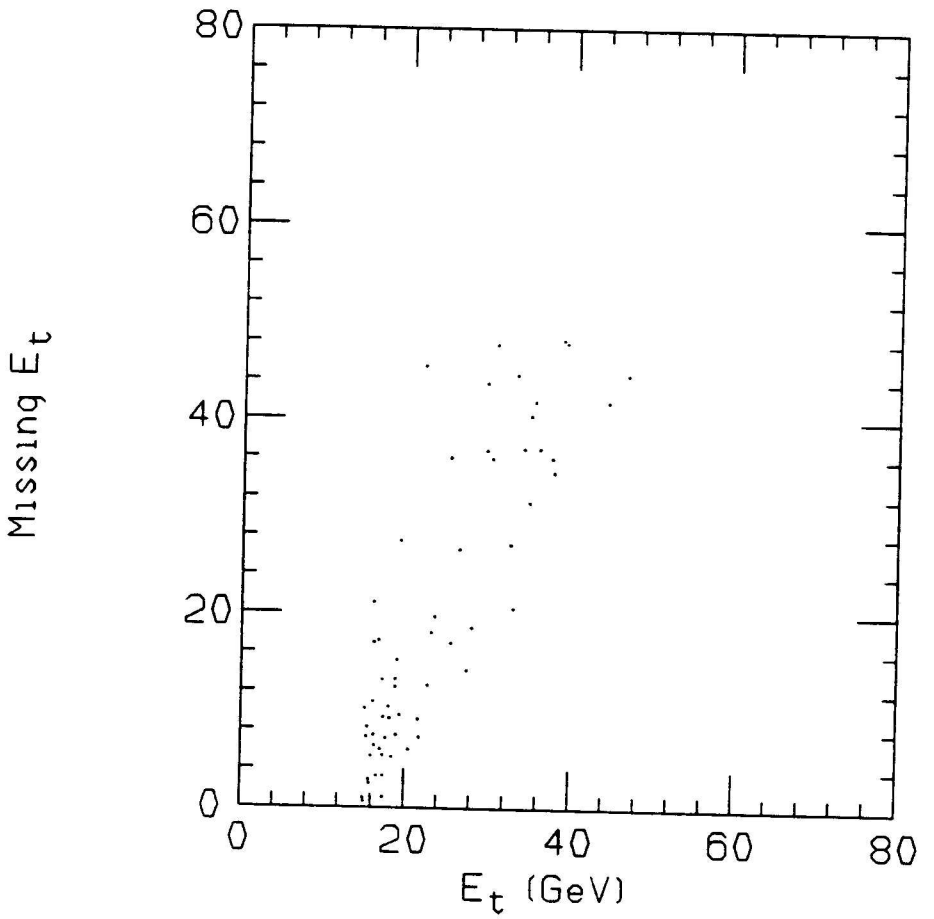

Figure 4.6: Distribution of $\not\!\!E_T$ versus E_T for events passing all W selection criteria except the $\not\!\!E_T$ cut.

W Cuts	Events passing cuts
Electron DSTs	$\approx 4 \times 10^5$
Had/EM < 0.05 isolation < 0.1 $E_T > 15$ GeV $-1 < \eta < 1$	3753
$E/p < 2.0$	137
Dijet veto	61
$\not\!\!E_T > 25$ GeV	21

Table 4.2: Cuts used in the selection of W candidates. The number of events passing each set of cuts is listed.

events from a single run rather than sporadically.

In order to find these effects, the average event $\not\!\!E_T$ for minimum bias triggers was calculated on a run by run basis (this value is called the $\not\!\!E_T$ offset). Runs whose average $\not\!\!E_T$ was larger than 5 GeV were excluded from the data sample. For all other runs, the $\not\!\!E_T$ offset is subtracted vectorially on an event-by-event basis to correct the $\not\!\!E_T$. We then require $\not\!\!E_T > 25$ GeV and are left with 21 W candidates. Table 4.2 lists all the cuts made and the number of events passing each set of cuts.

4.6 The W Sample

Figures 4.7- 4.9 show pictures from a CDF display package of a typical W candidate. Figure 4.7 is a "lego" plot of the calorimeters showing a rectangular view of the detector in $\eta - \phi$ space. The height of each vertical column is proportional to the E_T deposited. There is a cut on E_T of 0.5 GeV such that any tower with less than this amount is plotted with no energy. In the central region each column represents a single calorimeter tower. This event contains a single cluster with roughly 36 GeV and very little else in the calorimeter. The electron candidate is well isolated, and the event $\not\!\!E_T$ is 37 GeV.

Figure 4.8 shows an $R - \phi$ display of the CTC hits and reconstructed tracks. Energy in the central calorimeter is displayed as shaded areas immediately outside the CTC ring. This event has a high p_T track pointing at the electron cluster. There is relatively little activity in the chamber with all other tracks having p_T less than 2 GeV and no obvious clustering. Charged particles with $p_T < 250$ MeV have a radius of curvature too small to reach the calorimeters.

Figure 4.9 shows a display of the central wedge in which the electron candidate deposited its energy. Each phototube for the 10 towers is displayed separately with the shaded part of the column representing hadronic energy. The shower is mostly contained in one tower with very little transverse leakage into adjacent towers and small longitudinal leakage into the hadronic calorimeter. The wedge display also

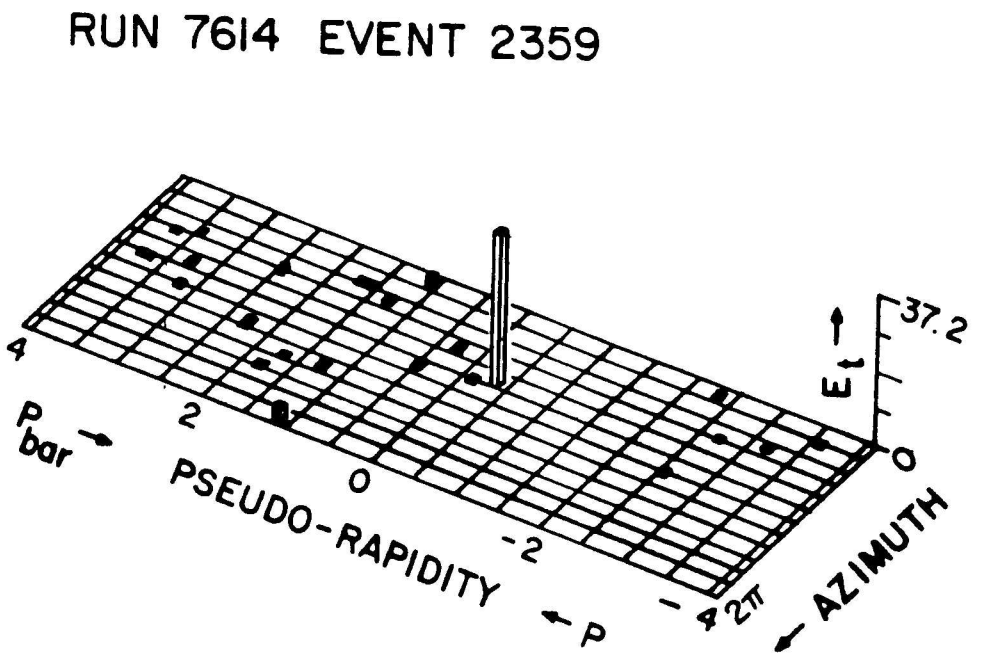

Figure 4.7: CDF display package "lego" plot showing energy deposited in the calorimeter for a typical W candidate.

RUN 7614 EVENT 2359

Trk.	Pt	ϕ	Ctg.
1	34.18	145	-0.52
2	0.88	92	0.29
5	0.80	107	
7	0.78	76	
3	-0.69	296	-0.37
4	0.62	325	0.80
6	-0.56	264	

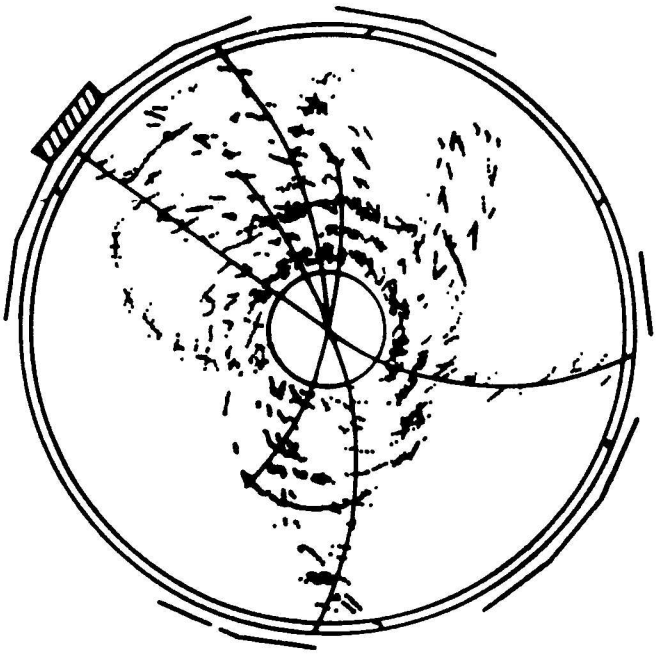

Figure 4.8: CDF display package view of the hits and reconstructed tracks in the central tracking chamber for a typical W candidate.

shows the shower profile found in the strip chamber. There are clear clusters in both the wires (ϕ) and the strips (η). The strip chamber cluster positions match the calorimeter energy deposition.

Figures 4.10 -4.12 show event distributions for the 21 W candidates. The Had/EM and isolation plots show these distributions falling off well before the cut value. The E/p plot shows a sharp peak near 1.0 with two events at relatively high E/p. Electrons from W decays can radiate photons (bremsstrahlung) as they pass through matter in the detector. If the photons are radiated before the CTC, the track p_T may be significantly less than the cluster E_T resulting in a large value for E/p. The two events at high E/p are considered likely bremsstrahlung candidates. Figure 4.11 shows the distance along the ϕ coordinate between the extrapolated CTC track position and the electron strip cluster wire position. Although we do not use this parameter to select W candidates, this plot indicates that the CDF detector is capable of matching track–strip positions to within roughly 3 mm. Finally, figure 4.12 shows the electron E_T spectrum. The plot shows the expected Jacobian shape with a peak near 36 GeV.

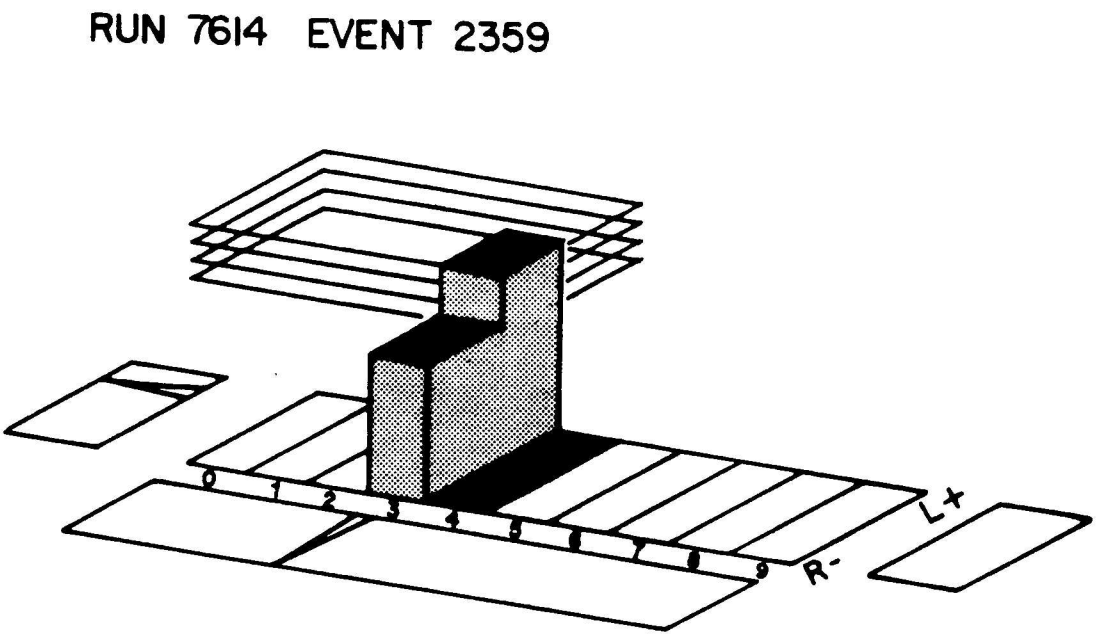

Figure 4.9: CTC display package view of a single wedge where the electron from a typical W candidate deposited its energy.

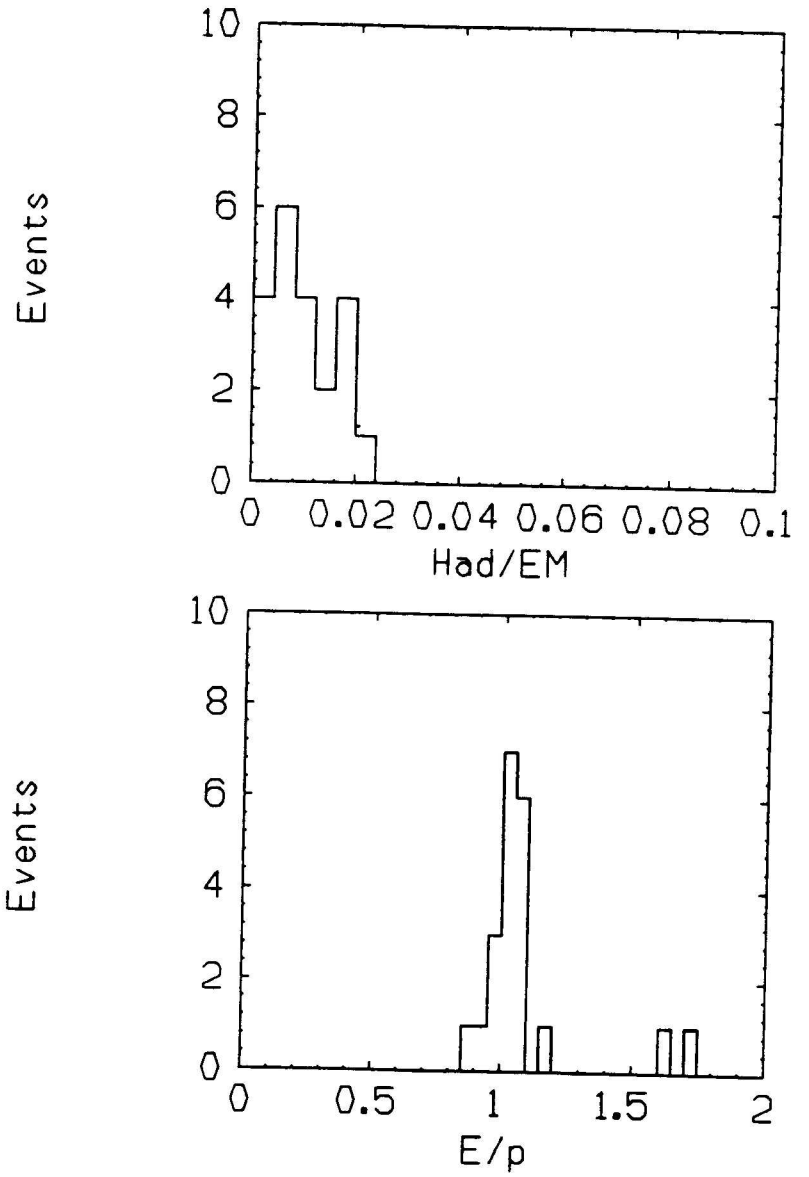

Figure 4.10: Distribution of Had/EM (top) and E/p (bottom) for the 21 W candidates.

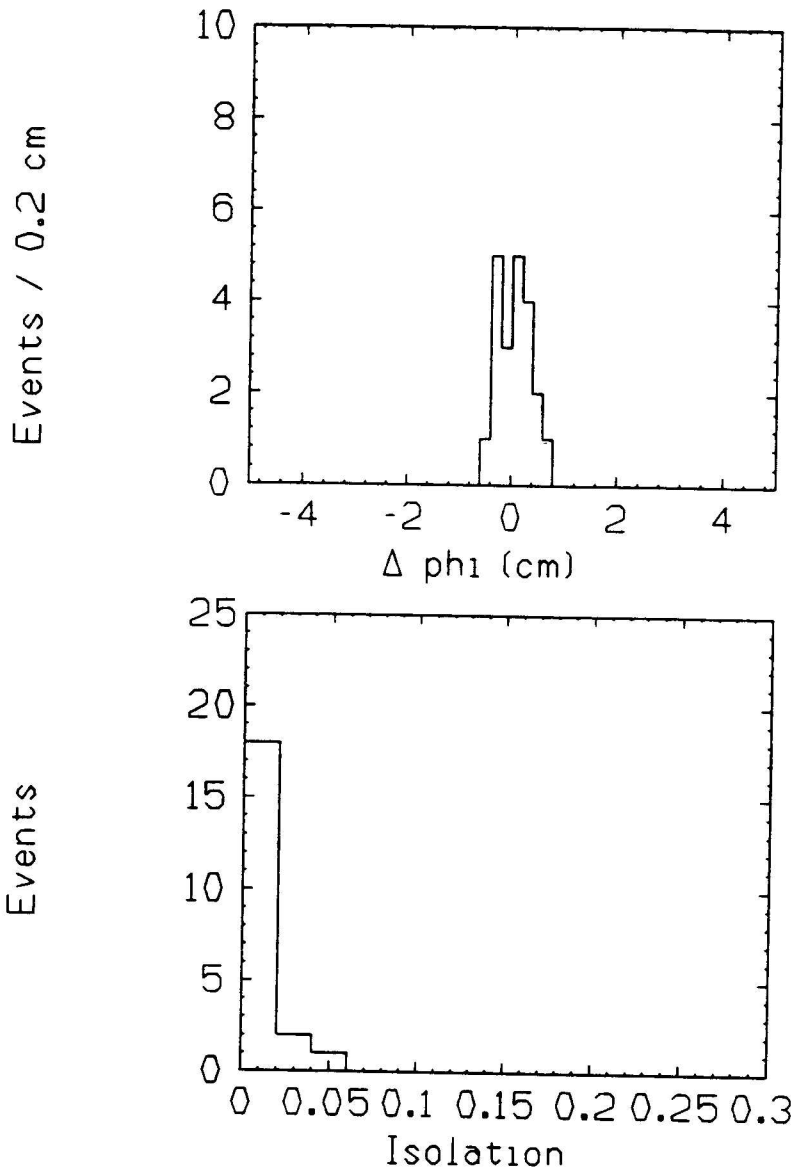

Figure 4.11: Distribution of isolation (top) and $\Delta\phi$ (bottom), the distance in ϕ between the extrapolated CTC track and the electron strip cluster centroid, for the 21 W candidates.

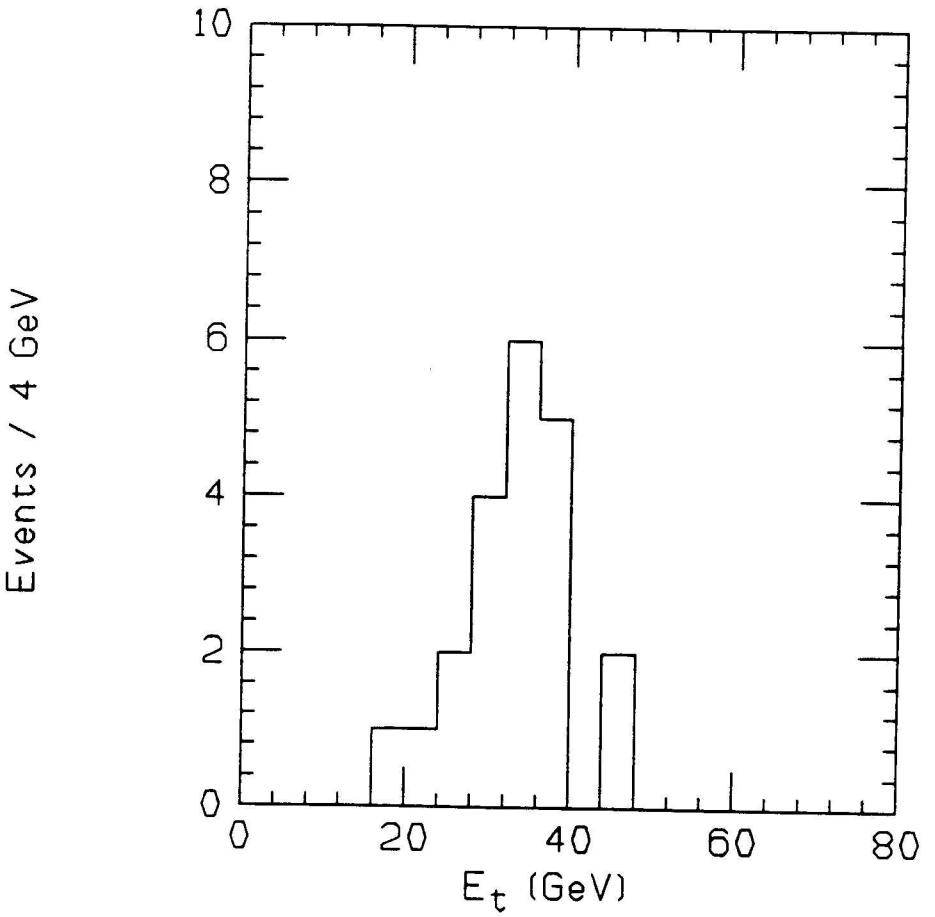

Figure 4.12: Distribution of E_T for the 21 W candidates.

Chapter 5

Acceptance and Efficiencies

To calculate a cross section we must understand the acceptance of the detector, the trigger, and our software in selecting W events. The study of these acceptances falls into 2 categories: acceptances we can study directly from colliding beam data and those we must study using Monte Carlo simulations. In general, we prefer acceptances based on colliding beam data, and whenever possible, use the numbers which come from those calculations. In some cases we are faced with the dual problem that studies based on data are plagued by low statistics whereas Monte Carlo predictions are uncertain because they haven't been well tested in the new energy region ($\sqrt{s}$ = 1.8 TeV). In cases such as these, we would like to check our results from colliding beam data with results from Monte Carlo studies to increase our confidence in the acceptance values.

We studied the Had/EM, isolation, E/p (tracking efficiencies), and dijet cuts directly from either testbeam or 1987 colliding beam data. Due to low statistics, the

isolation and dijet cuts were checked with Monte Carlo results for consistency. We used Monte Carlo simulations to calculate acceptances for the trigger, electron offline code, rapidity, E_T , and $\not\!\!E_T$ cuts. We also used Monte Carlo simulations to study the probability that electron bremsstrahlung would cause the E/p cut to fail.

5.1 Monte Carlo acceptances

The Monte Carlo simulations consisted of generating $W \rightarrow e\nu$ events with version 6.10 of the Isajet Monte Carlo program and modeling the detector response with the CDF detector simulation software package. The acceptance calculations followed the flow of the data analysis as much as possible. We first studied the trigger acceptance. Then, using only the events which passed the trigger cuts, we ran the offline electron cluster algorithm and applied cuts on the electron η, the electron E_T , the event $\not\!\!E_T$. In order to check the results of the acceptance studies from colliding beam data, we then studied the remaining W selection criteria.

There is some uncertainty in the Monte Carlo parameters such as W mass and the proton structure functions which affect acceptance calculations. The dominant error in the acceptance calculations is the error associated with the η acceptance. This error is large due to the uncertainty in the structure functions and the sharp falloff in the electron η distribution. Figure 5.1 shows the η distribution for electrons from W decay generated by the Isajet Monte Carlo simulation. Since the distribution

falls off sharply near our cut value of $|\eta| = 1$, small changes in the distribution can have significant effects on the acceptance. Theoretical calculations in lowest order perturbation theory using several structure functions and varying the W mass yield acceptances from 0.47-0.51 [41]. Monte Carlo studies with various structure functions give acceptances in the range 0.48-0.53. We take the acceptance in the region -1.0 $< \eta <$ 1.0 to be 0.50 $\pm$ 0.3. Table 5.1 shows the acceptances as a function of the various trigger thresholds for the W selection cuts.

The trigger acceptances show a significant dependence on the trigger thresholds used in the electron trigger (see table 4.1). Since the E_T and the $\not\!\!E_T$ cut are large compared to the trigger thresholds, this variation is essentially eliminated by the time the E_T and $\not\!\!E_T$ cuts are imposed, and we do not have to weight the acceptance by the percentage of the total luminosity for each trigger table. The acceptance for the trigger, electron algorithm, η, E_T , and $\not\!\!E_T$ cuts is 0.38 $\pm$ 0.03 where the error combines the acceptance error and the statistical error for the Monte Carlo events.

Results from table 5.1 allow us to check acceptances found from data against the Monte Carlo simulation. We then estimate the following acceptances:

dijet	0.95
Had/EM	0.98
Tracking efficiency	0.98
Isolation	0.99

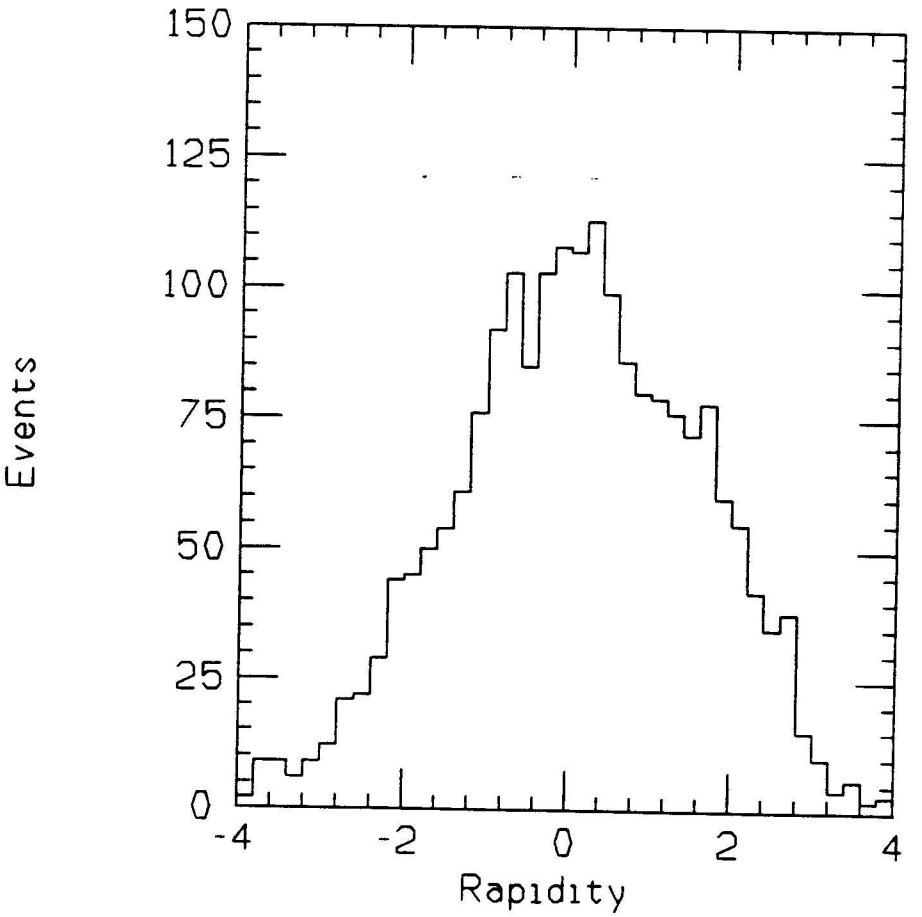

Figure 5.1: The rapidity distribution for electrons from W decay.

Cut	Trigger Table				
	Low	Med	High	Burn	30
Trigger	.818	.680	.553	.535	.618
Production	.752	.641	.537	.520	.583
$-1 < \eta < 1$	.470	.468	.465	.454	.447
E_T	.436	.436	.436	.434	.433
$\not{E}_T$	.380	.380	.380	.379	.380
Dijet	.361	.361	.361	.360	.361
Had/EM	.354	.354	.354	.353	.354
E/p	.347	.347	.347	.346	.347
Isolation	.344	.344	.344	.343	.344

Table 5.1: The cumulative fraction of W bosons passing the cuts based on Monte Carlo simulations. Detector noise and radiative decays of the electron are not included.

A W event may fail the dijet cut because there is a jet recoiling off the W and into the dijet region or because detector noise simulates a jet in the dijet region. The detector simulation does not explicitly put in detector noise; therefore, the acceptance shown above only indicates failures due to real jets in W events.

5.1.1 E/p

There are two ways a real W event can fail the E/p cut. A stiff track may not be reconstructed by the tracking program due to inefficiencies in the CTC or the tracking software. A second failure mode involves radiative W decays. If the electron from the W decay radiates a photon of sufficient energy, the momentum of the electron as measured by the CTC may be less than half the cluster energy, and E/p will be larger than 2. Tracking efficiencies will be discussed below in section 5.2.3. The probability that radiative decays will cause the E/p cut to fail will be considered here.

The radiative decay process was studied using an algorithm developed by Berends and Kleis [42]. The study was performed in 3 steps: first, the initial state W was generated; second, the W was allowed to decay into $e\nu$ or $e\nu\gamma$ (internal bremsstrahlung); finally, the detector response and external bremsstrahlung were simulated. W bosons were generated using the Glück, Hoffmann, Reya parametrization [43] for the structure functions. To properly decay the W bosons, one must choose a minimum energy for the radiated photons. This "cutoff" energy was defined in the W center-of-mass

frame such that photons below this energy would not affect the decay kinematics or the E/p ratio. For this study the cutoff was chosen near 200 MeV [44]. With this cutoff, 22.9% of all generated W bosons decayed into $e\nu\gamma$. The CDF detector simulation package then adds external bremsstrahlung. At $\theta = 90°$ there are roughly 0.03 radiation lengths of material before the active region of the CTC (see figure 3.9).

After internal and external bremsstrahlung were simulated, the E/p response was calculated, and the probability that the E/p cut would fail was determined. Figure 5.2 shows the E/p distribution for our sample of 21 W events with the normalized distribution from simulated decays overlayed. The main contribution to the broadening comes from detector resolution and not radiative decays. Radiative decays produce a tail in the distribution at high E/p values where the photon has carried off a significant fraction of the cluster energy. From the E/p distribution of simulated decays, we estimate the radiative part of the E/p acceptance to be 0.97 ± 0.01.

5.2 Acceptances from data

5.2.1 Had/EM

There are 2 ways to determine the Had/EM response of the central calorimeter. One can use the extensive testbeam data taken at several energies or select a clean sample of electrons from the 1987 run data. The testbeam approximated the detector response, but there were subtle differences between testbeam conditions and those

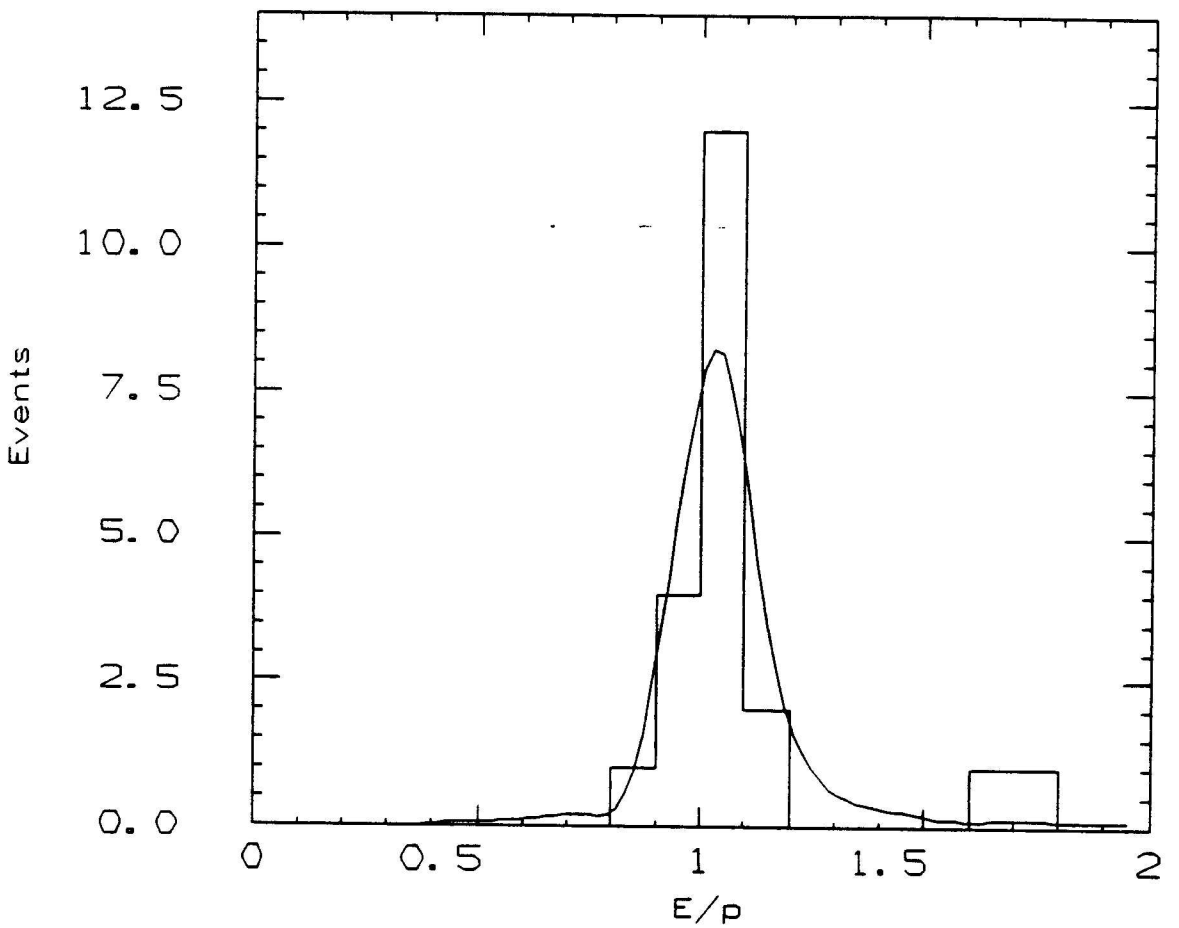

Figure 5.2: The E/p distribution for the 21 W candidates with a normalized curve from Monte Carlo data which simulated electron bremsstrahlung.

during the run. The testbeam measures the response to single electrons whereas real electron clusters may contain energy from other particles in the event. A typical 500 MeV pion can double the hadronic energy in an electron cluster from W decay. All testbeam data was taken with the electrons originating from an event vertex at the center of the detector. During data taking at the Tevatron, the distribution of event vertices was gaussian with a sigma of $\sim$ 30 cm in the beam direction. Electrons entering the detector from a vertex off center will pass through a different number of radiation lengths of material in the EM calorimeter than one from a vertex at detector center, and the Had/EM responses may differ. Because of these considerations, we would like to check the Had/EM response of a clean electron sample with that predicted from testbeam studies.

There are several potential electron samples from the 1987 data. There are electrons coming from W decays, inclusive electrons (any event with an electron candidate), and electrons from photon conversions. Since higher energy electrons have a greater longitudinal leakage than lower energy electrons, the Had/EM response varies with energy. Ideally, we'd like an electron sample with roughly the same energy spectrum as electrons from W decays. The electron analysis W sample is a biased set; however, the $\not\!\!E_T$ analysis sample uses only a very weak longitudinal leakage requirement (the EM fraction was required to be greater than 85%) and is essentially unbiased. This sample has too few events to make reasonable comparisons with testbeam

data so we must look elsewhere.

We may select a sample of inclusive electrons by imposing strict electron cuts excluding a Had/EM cut, and this sample has the best statistics of any electron sample. Unfortunately, inclusive electrons candidates contain pion background which is essentially impossible to remove. Pions may interact via charge exchange after only a short distance in the EM calorimeter and closely simulate an electromagnetic shower. Strict isolation requirements vastly reduce the jet background; however, the huge jet cross section coupled with the non-negligible fraction of jets which undergo hard fragmentation into a single stiff charged track and other low energy particles ensure that jets can pass isolation cuts. Testbeam studies with pions show their Had/EM distribution is essentially flat between 0.0 and 0.1 . The Had/EM distribution of inclusive electron samples show a long tail which is presumably heavily contaminated with pion background. Although one could try to estimate the background and subtract it from the sample, the conversion sample seems more promising.

A sample of conversion electrons was found using an inclusive electron sample which was then scanned in detail for evidence of conversions. The scanning process consisted of looking for 2 oppositely charged CTC tracks one of which pointed accurately at the electron cluster. The tracks were required to have a near zero opening angle indicating decay from a massless particle. The Vertex Time Projection Chamber hits were searched either for evidence of no track matching the extrapolated CTC

track position or evidence of a track beginning inside the chamber and matching the CTC track position. A sample of 56 good conversion candidates were selected.

The Had/EM response for electrons is sensitive to the event topology. Electron clusters from W decays contain very little energy from other particles in the event; therefore, their Had/EM response should be similar to testbeam electrons. Conversion electrons may be found in events with significant energy flow near the electron. These other particles may "contaminate" the electron cluster and raise the Had/EM value. Since we are using the conversion sample to understand the Had/EM response of electrons from W decays, we would like the event topology in the region near the electron cluster to resemble W events; therefore, we used an isolation requirement in the conversion sample similar to that used for the W selection.

The E_T spectrum of the conversion candidates is shown in figure 5.3. The spectrum peaks near 15 GeV; therefore, we compared the Had/EM response to 15 GeV testbeam electrons. Figure 5.4 shows the Had/EM response for the conversion candidates with a curve showing the response of 15 GeV testbeam electrons. Clearly the testbeam data does not fit the conversion data very well for low values of Had/EM. At higher values (above 0.02) there is much better correspondence. A χ^2 fit for all bins gives χ^2/DOF (degrees of freedom) = 3.11; however, if the first 2 bins are combined, the χ^2/DOF = 1.15. There are details of the Had/EM response at low values which need to be understood better, but for higher values the testbeam data should give a

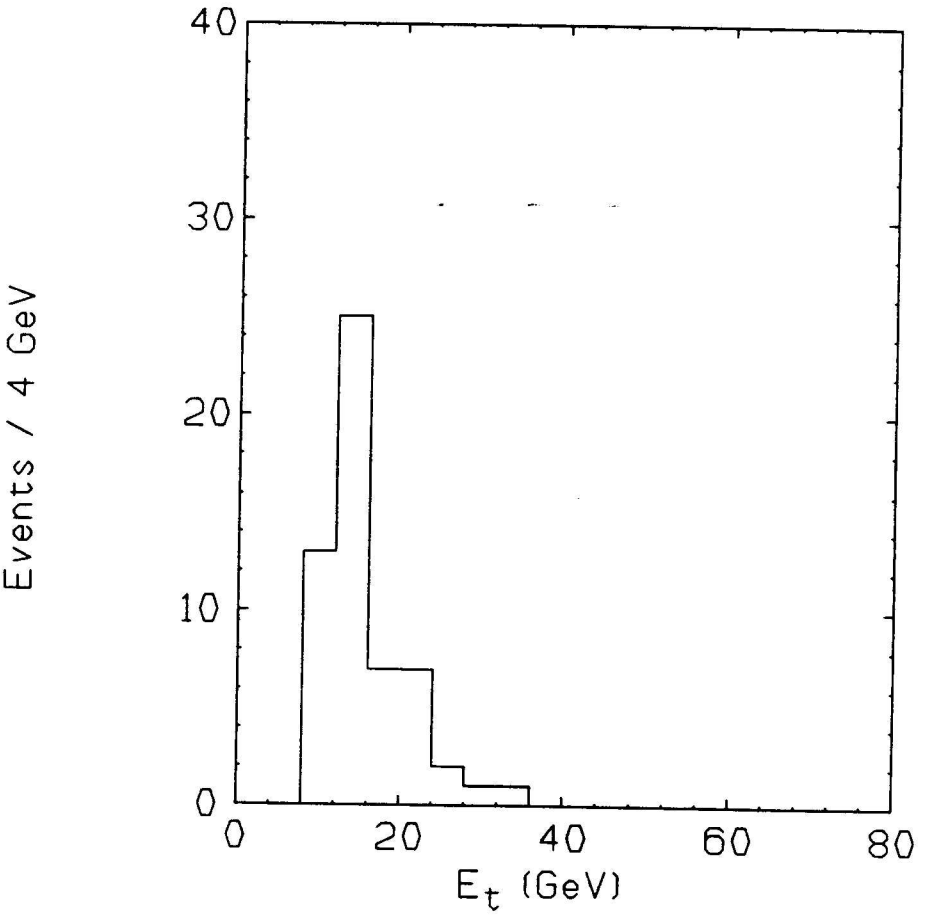

Figure 5.3: E_T spectrum for the conversion electron sample.

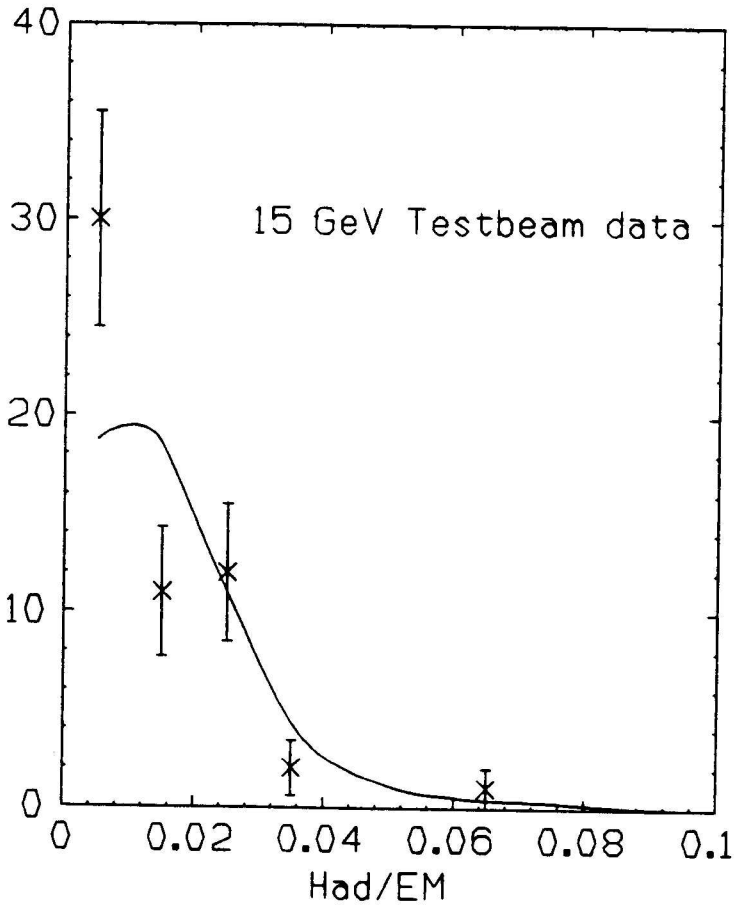

Figure 5.4: Had/EM response for conversion candidates. The curve shows testbeam data for 15 GeV electrons.

Energy(GeV)	Acceptance
15	0.97
25	0.96
37.5	0.96
50	0.94
75	0.92
100	0.90

Table 5.2: Electron acceptance for the cut Had/EM $<$ 0.05 from testbeam data at various energies.

reasonably accurate measure of the Had/EM acceptance for electrons. Table 5.2 shows the electron acceptances for the Had/EM cut from testbeam data at various energies. Since the acceptances do not vary strongly with energy, we expect the response of 37.5 GeV testbeam electrons to give an accurate measure of the acceptance of the Had/EM cut for electrons from W decays. A upper limit on the error comes from the assumption that the acceptance could be 100% at Had/EM values of 0.05. Then the error would be 1.00 – 0.96 or 0.04. We then take the Had/EM acceptance to be 0.96 $\pm$0.04.

5.2.2 Isolation

The isolation parameter is a measure of the energy deposited in the calorimeter near the electron cluster. Monte Carlo predictions for energy in the underlying event for

W boson production at $\sqrt{s} = 1.8$ TeV have not been tested; therefore, we would like to measure the distribution of the isolation from real data. Unfortunately, our W sample contains too few events to gather reasonable statistics. In order to bypass this problem we make the following assumption: in W events the electron position in $\eta - \phi$ space is independent of the energy flow in the rest of the event. This assumption is not strictly correct, but the error is small compared to other acceptance errors. The assumption is valid for W events with no jets since the rapidity distribution of tracks from the underlying event is flat with no ϕ structure. For W events with jets, the W recoils off the jet with some p_T . In general the p_T is much smaller than the W mass, and the decaying electron receives very little boost. There is, however, a tendency for the electron to decay away from the jet due to this boost. Therefore, energy from jets will more likely be deposited outside the W isolation cone than inside the cone.

The isolation study began by selecting a sample of W bosons with strict cuts to eliminate backgrounds as much as possible. For each W event, we translated the actual electron cluster position to various locations in the central calorimeter and calculated the isolation value. We replaced the tower energies in the new location with the tower energies of the electron cluster leaving all other tower energies unchanged. The procedure ensured that no 2 cones overlapped (i.e. no towers were sampled more than once for any event) and no cone overlapped the original electron cluster towers. Regions inside the original W isolation cone were sampled less frequently than regions

outside this cone since cones which might contain these towers are sometimes thrown out because they also contain the electron cluster towers. We then sample regions with some energy from jets more frequently than we should, and the isolation values will be somewhat higher than actual W isolation values. Our acceptance value is therefore an underestimate.

There are 21 W bosons in the W sample used for cross section calculations; however, this sample comes from a subset of the full data. As mentioned earlier, some runs were thrown out due to various problems. These problems did not necessarily effect every event in those runs. In order to get the maximum useful W sample to study the isolation cut, we chose to select W bosons from the entire data set with a combination of strict cuts and scanning to ensure that the events were not background. The cuts used are shown in table 5.3. The cut $\Delta\phi$ is the distance in the ϕ direction between the extrapolated CTC track position and the strip chamber cluster position. In addition to adding this cut, the E_T and Had/EM cut were made tighter. The isolation cut was loosened because requiring a small isolation value could bias the overall energy flow in events. In fact, due to the stricter W cuts used in this study, no events passed all the other cuts and had an isolation value larger than 0.1, the W selection cut value. There were 26 W events selected in this manner.

To some extent the radius of the isolation cone is arbitrary. The cut is used to remove jets and other objects whose cluster size exceeds that of electrons. A

Cut		value
E_T	>	20 GeV
$\not\!\!E_T$	>	25 GeV
Had/EM	<	0.03
E/p	<	2.0
isolation	<	0.3
$\Delta\phi$	<	1.0 cm
Dijet veto		

Table 5.3: Cuts used to select W bosons for the isolation acceptance study

larger cone will have a greater chance of including the excess energy of these objects; however, it will also have a greater chance of excluding W events with a jet near the electron. We studied 2 cone radii, 0.7 and 0.4. The smaller cone contains roughly 12-14 calorimeter towers after eliminating the towers of the electron cluster. The larger cone has about 3 times as many towers. Based on considerations of W acceptance and background rejection, we chose to use a cone of radius 0.4, but results from both acceptance studies will be given here.

The underlying event for W bosons is similar to minimum bias events in the number of charged tracks and the energy deposition in the detector. We repeated this study on a sample of minimum bias events to compare results with W events. Using the Isajet electron E_T spectrum from W decay, we simulated an electron cluster

at various positions in the central calorimeter and overlayed the cluster on minimum bias events. We required the electron cluster to have $E_T > 15$ GeV.

Figure 5.5 shows the isolation values for both cone sizes from the various studies. The actual isolation values for the 26 W bosons are shown with normalized, smoothed results from minimum bias events and from the W isolation study. For both cone sizes the minimum bias curve closely follows the W curve. Since the number of charged tracks in W events is larger than in minimum bias events (see figure 5.7), we expect higher isolation values from W events. The differences are small, and only in the 0.7 radius case does the minimum bias curve noticeably fall off more sharply. These isolation values are ratios where the energy in the cone is normalized to the W electron E_T , and they are only relevant to electron samples whose E_T spectrum is similar to the W electron E_T spectrum. Figure 5.6 shows the energy in the isolation cone, excluding the electron cluster energy, for the W isolation studies and both cone sizes. These distributions show the expected energy deposited by the underlying event for isolated electron clusters.

Table 5.4 gives acceptances for both cone sizes with statistical errors. The acceptance for the isolation cut used in the cross section analysis (cone size = 0.4 and cut value = 0.1) is 0.99 ± 0.01. From table 5.1 the acceptance for the isolation cut from Monte Carlo studies was also 0.99.

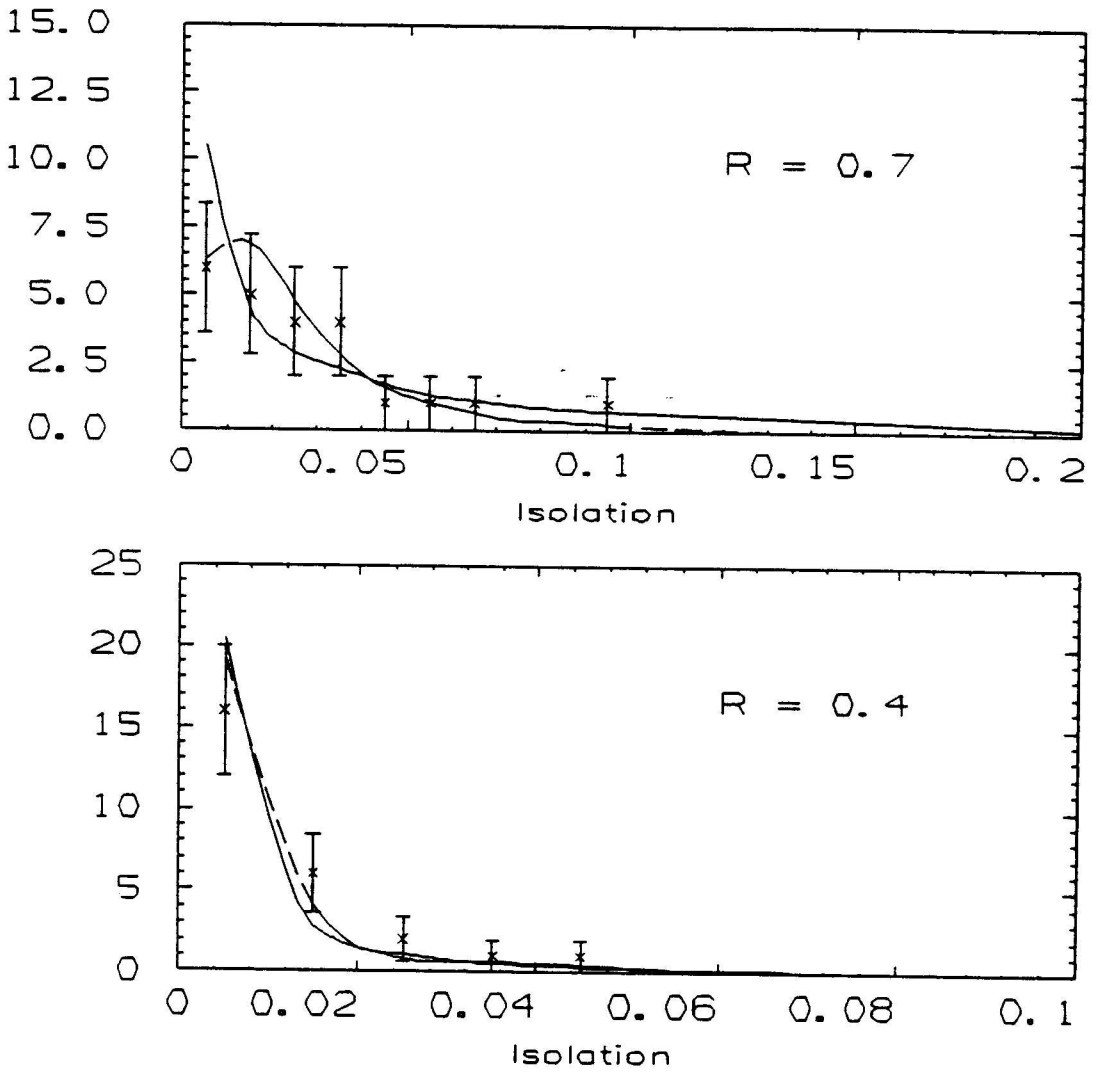

Figure 5.5: Isolation values for W events (crosses). Cone size = 0.7 (top). Cone size = 0.4 (bottom). The dashed line represents the Monte Carlo distribution and the solid line represents the W isolation study results.

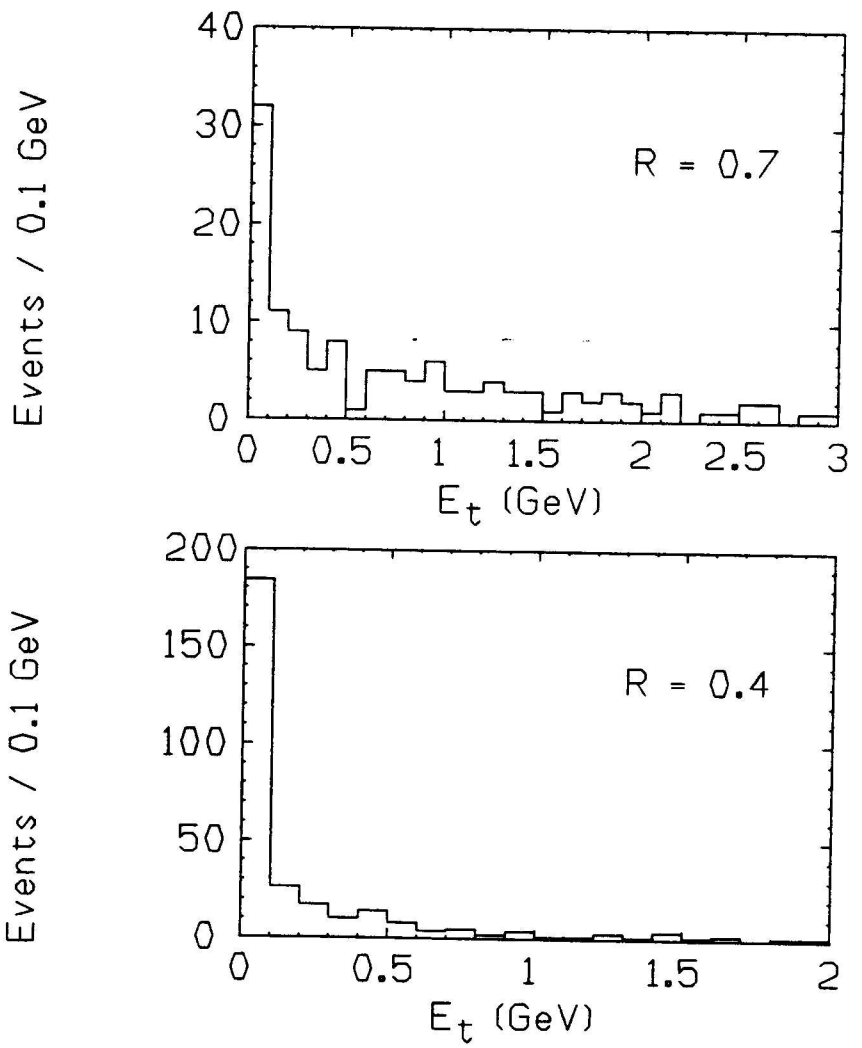

Figure 5.6: E_T inside isolation cone excluding the electron cluster. (Bottom) Cone size = 0.4. (Top) Cone size = 0.7.

Cone size	Cut value	Acceptance
0.4	0.1	0.99 ± 0.01
	0.2	1.0
0.7	0.1	0.94 ± 0.02
	0.2	0.99 ± 0.01

Table 5.4: Acceptance values for the isolation cut. Errors are statistical.

5.2.3 Tracking

Since the W selection criteria require a track in the CTC pointing at the electron cluster, we must understand the efficiency of the CTC track-finding algorithm. W bosons differ from many hadron collider events because they are so "clean". The production of the W and its subsequent decay into an electron and neutrino often produces a single detected particle with E_T significantly larger than 1.0 GeV. The underlying event looks similar to a minimum bias event. In order to study the tracking efficiency, the most useful events then are minimum bias events.

In this case the relevant feature of the event types is the density of tracks. Figure 5.7 shows the quantity $dN/d\eta$ for both W and minimum bias events as a function of η. W events have roughly 50% more tracks per unit of rapidity; however, since the number of tracks is small and tracks are reasonably well isolated, we would expect track finding efficiencies to be similar.

Two studies were done to determine the tracking efficiency for minimum bias

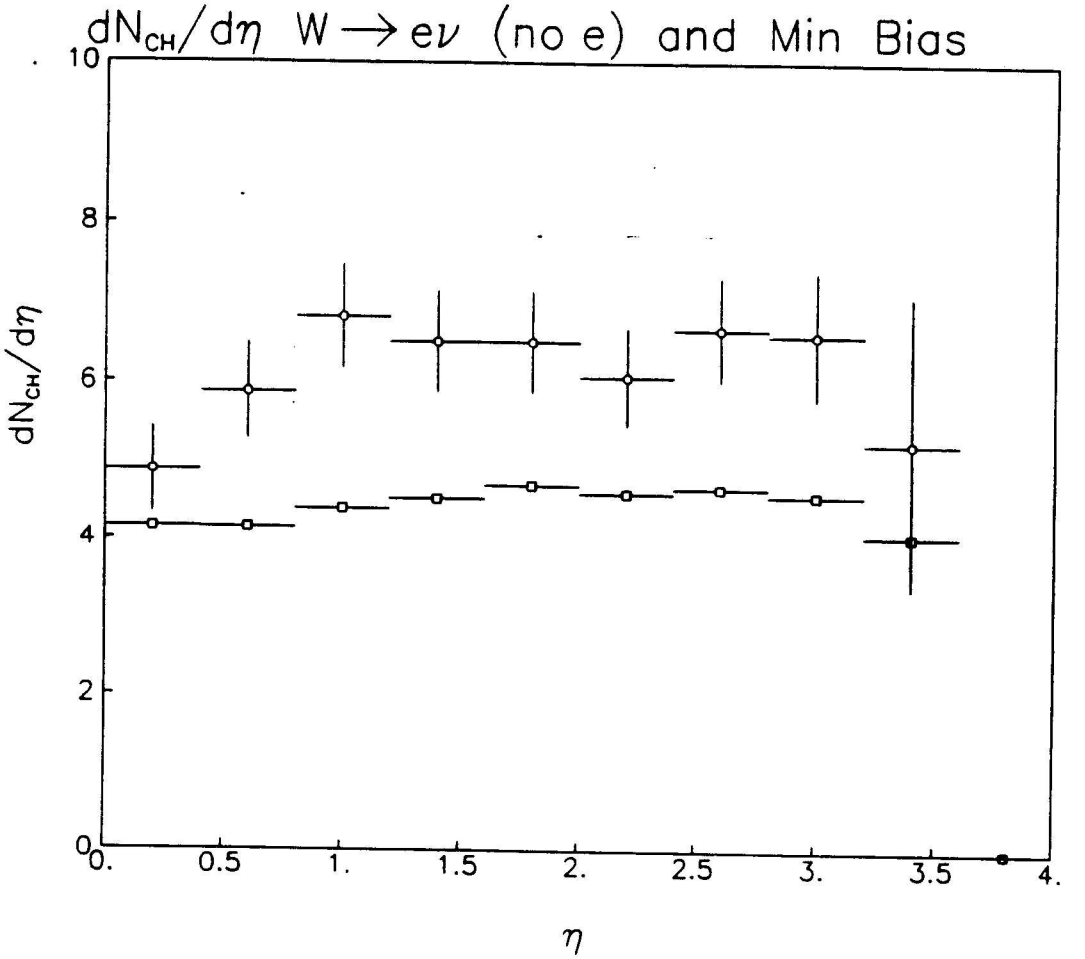

Figure 5.7: $dN/d\eta$ for W events and minimum bias events as a function of η. The circles are W event data, and the squares are minimum bias data.

Track p_T (GeV)	Efficiency
0.300	0.665 ± 0.02
0.400	0.913 ± 0.02
0.500	0.973 ± 0.01
1.0	0.995 ± 0.004
2.0	0.995 ± 0.004
5.0	0.981 ± 0.01

Table 5.5: Track finding efficiency from Monte Carlo study simulating tracks. The errors are statistical.

tracks. The first involved scanning a large number of minimum bias events to find all tracks. The tracking program was then run, and the efficiency was calculated as the percentage of number of tracks found by the tracking program divided by the number of tracks found through scanning.

The second study used a Monte Carlo program to simulate tracks. The study superimposed CTC hits of a simulated track over the CTC hits of a real minimum bias event. The tracking algorithm was then run to see if the simulated track was found. The ϕ distribution of the simulated tracks was uniform and the rapidity distribution was flat from -1 < η <1. Table 5.5 shows the tracking efficiency for tracks of varying p_T.

Both studies calculated efficiencies at various track p_T's. Minimum bias events

contain mostly low p_T tracks. Since electrons from W decays have high p_T , we should use the tracking efficiency for minimum bias tracks with the highest p_T . The efficiency from the scanning study for tracks in the range 3 - 10 GeV/c was 0.99 $\pm$ 0.01. The Monte Carlo study with tracks of 5 GeV/c gave an efficiency of 0.98 $\pm$ 0.01. The errors in each case are statistical. We take the tracking efficiency for W events to be 0.98 $\pm$ 0.02.

5.2.4 Dijet

There are 2 effects which contribute to events failing the dijet cut. As mentioned earlier, W bosons may recoil off quarks or gluons which form jets in the calorimeter. If the W decays such that the electron is roughly 180° in ϕ from the jet, then the event may be vetoed. This acceptance may be studied from the data, however, once again statistics is a problem. The other contribution to the dijet acceptance comes from noise in the gas calorimetry yielding spurious jets. Several effects give rise to anomalous clusters including electronic noise generated in cables, high voltage discharge in gas calorimetry, and low energy particles (often neutrons) which produce large calorimeter response due to the combination of high gain and sampling fluctuations. Noise may produce jet-like clusters with sufficient energy in the proper ϕ sector to veto the event. Software noise filters which eliminate many of these spurious clusters have been written. These filters help us to discriminate between real clusters

and noise.

To study the dijet cut acceptance, we used a method similar to that used in studying the isolation acceptance. We used the same W sample described in section 5.2.2 for the isolation study. The dijet cut vetos events with clusters within a 60° sector opposite the electron cluster ϕ. There are 6 such sectors per event; however, since the W sample used for the isolation study was selected with the dijet cut to reduce background, there are only 5 available ϕ sectors for jets. If jets were evenly distributed in ϕ, there would be a 1 in 5 chance that a given jet of sufficient energy would cause the event to fail. We could simply count the number of jets found in the W sample and divide by the number of potential 60° sectors in the events (5 $\times$ number of events) to find the probability that W events will fail the cut. Noise clusters are produced roughly independent of ϕ so we may use this method to calculate the probability that a W event will fail the dijet cut due to noise. Real jet production in W events is correlated to the electron ϕ. The ϕ difference between jets and the electron peaks near 180° because the W recoils against the jet and the decay electron receives a boost opposite the jet direction. Since real jets and noise have different ϕ distributions, we study them separately.

Running the noise filters on the W sample determines which jets are likely to be generated by noise and which are probably real. There are 7 noise clusters and 6 real jets in the 26 events. The dijet failure rate due to noise is then simply $7/(5 \times 26)$ or

Cuts	Acceptance
Trigger, Rapidity E_T , $\not\!\!E_T$	0.38 ± 0.03
Had/EM	0.96 ± 0.04
Isolation	0.99 ± 0.01
Dijet	0.90 ± 0.03
E/p (Tracking)	0.98 ± 0.01
E/p (Radiative decay)	0.97 ± 0.01
Overall Acceptance (ϵ)	0.31 ± 0.03

Table 5.6: Summary of values used in cross section calculation.

5.3% (the acceptance is 0.95 ± 0.02). The same type of calculation for the contribution of real jets yields 4.6%. The real jet value is suspect due to the jet ϕ distribution so we used Monte Carlo simulations to check our result. Various simulations yield acceptances between 0.93 and 0.96. We take the dijet acceptance due to real jets to be 0.95 ± 0.02. Combining the 2 acceptances, we find the dijet acceptance is 0.90 ± 0.03.

5.3 Summary

Table 5.6 summarizes the acceptances for the various W selection criteria. The dominant contribution to the error comes from our estimate of the rapidity acceptance.

This error is probably overestimated, and as mentioned, if the whole calorimeter is used to detect W bosons in the next data run, the acceptance will be higher and the error will drop considerably.

Chapter 6

Backgrounds

Backgrounds to the process $W \rightarrow e\nu$ must contain the two features which make the W decay signature distinctive - a high p_T isolated electron candidate and significant $\not\!\!E_T$. The background process does not have to produce either a physical electron or particles that always go undetected in the calorimetry such as neutrinos. Under the proper conditions a jet may fake an electron, and particles which enter cracks in the calorimeters will cause an energy imbalance in the event. There are three processes which can contribute to the background: W bosons decaying to taus, light quark production (referred to as QCD background), and heavy quark (i.e. b and possibly t) production.

The decay $W \rightarrow \tau\nu$ with the subsequent decay $\tau \rightarrow e\nu\nu$ gives almost the identical signature as $W \rightarrow e\nu$. The electron from the decaying tau has a lower p_T spectrum because it must share the tau's energy with two neutrinos, but on an event by event basis, these two processes cannot be distinguished. Light quark jet production can

contribute to the background through a two step process. First, one jet must fake an electron (see section 4.5.1). Second, at least one other jet in the event must be mismeasured such that there is significant $\not\!\!E_T$. Heavy quark production differs from light quark production in that heavy quark decays can directly produce high p_T isolated electrons instead of faking them. The background calculations for these 3 processes will be discussed in the sections below.

6.1 QCD Light Quark Background

To estimate the QCD light quark background we need to understand the probability that a jet will fake an electron in events that have kinematic properties similar to W events. We loosened our W selection cuts slightly to find samples of events that have a high probability of containing jets rather than electrons. Using these samples, we then extrapolated into the W signal region to estimate the QCD background. We did several studies all using this approach but differing in the details.

6.1.1 $\not\!\!E_T$ – E_T extrapolation

Our first study involved defining 2 regions in $\not\!\!E_T$ – E_T kinematic space. The first region, called the "control" region, has the following cuts: $E_T > 10$ GeV and $\not\!\!E_T < 20$ GeV. The second region, or "signal" region, is defined by the cuts: $E_T > 15$ GeV and $\not\!\!E_T > 25$ GeV. This "signal" region has the same kinematic cuts as the W

Cut	Event Type		
	QCD1	QCD2	Isolated electron
Had/EM	0.03 - 0.1	0.03 - 0.1	< 0.05
E/p	< 2.0	< 2.0	< 2.0
isolation	0.1 - 0.3	< 0.1	< 0.1
LSHR	-	> 0.2	-
Dijet	no	no	yes
Rapidity	$-1 < \eta < 1$	$-1 < \eta < 1$	$-1 < \eta < 1$

Table 6.1: Cuts for the various event types used in QCD background study.

selection criteria. The "signal" region's high $\not\!\!E_T$ cut should exclude all light quark multijet events except those which contain an unusually large amount of energy either mismeasured or lost in calorimeter cracks. On the other hand, the "control" region should be dominated by background.

We then defined 2 types of events: those which pass all the isolated electron cuts and those which pass similar cuts modified to select QCD background and reject electrons. Events that pass the isolated electron cuts and fall in the "signal" region are precisely our W candidates. We used 2 mutually exclusive sets of cuts to select QCD background events. These are shown in table 6.1 along with the isolated electron cuts for reference.

The cut LSHR is a localized isolation requirement and is used to discriminate between electrons and jet background. Testbeam data and Monte Carlo calorimeter simulations enable us to predict how electrons will deposit their energy in the central calorimeter. Knowing the electron p_T and the trajectory into the wedge, we can calculate the relative amounts of energy expected in the different towers of an electron cluster. LSHR is a measure of the difference between the predicted energy deposited in each tower of a cluster and the actual energy measured in the towers. Electron candidates with more than a single particle depositing energy in the cluster will usually fail a tight LSHR cut because the tower energy profile will not match the expected profile for a isolated electron.

The cuts listed in table 6.1 differ from the W selection cuts in the Had/EM range and the isolation requirements. Pions have a flat Had/EM response in the region below 0.1, but few electrons have Had/EM $>$ 0.03 (roughly 5 - 10% depending on the energy). Isolated electrons from W decay have a very low probability of having isolation $>$ 0.1 or LSHR $>$ 0.2. The 2 samples, QCD1 and QCD2, are mutually exclusive because the isolation requirements do not overlap.

Using the "control" and "signal" regions and the 2 types of events, we estimate the QCD background with the equation:

$$\text{QCD background} = \frac{N^W_{QCD}}{N^C_{QCD}} \times N^C_e \tag{6.1}$$

where the superscripts refer to the region (signal or control) and the subscripts refer

to the type of event (QCD or electron). Equation 6.1 essentially equates the ratio of QCD-like events to electron-like events in the two regions.

There are two reasons why we expect this estimate for the QCD background to be an upper limit. First, we know from testbeam studies that the π/e rejection gets better as the energy increases so fewer pions will fake electrons. The energy of clusters in the signal region tends to be higher than those in the control region (see figure 4.6); therefore,

$$\frac{N_e^C}{N_{QCD}^C} > \frac{N_e^W}{N_{QCD}^W}$$

where the term N_e^W is the QCD background. Second, since equation 6.1 is intended to estimate only QCD background, ideally only real QCD events would be included; however, there is contamination from other sources. This contamination is dominated by electrons, which may come from $W \rightarrow e\nu$ decays, $W \rightarrow \tau\nu$ decays, b decays, or other sources. These electrons will increase the term N_e^C in equation 6.1 and tend to increase the background estimate.

Table 6.2 shows the results of this study along with the background calculation for each type of QCD event.

6.1.2 Isolation – $\not\!\!E_T$ extrapolation

The second study involved defining regions in isolation – $\not\!\!E_T$ space and preforming a similar extrapolation. We defined the 4 regions:

Quantity		Number	Background
	N_e^C	113	
QCD1	N_{QCD}^W	1	
	N_{QCD}^C	120	0.79 ± 0.79
QCD2	N_{QCD}^W	4	
	N_{QCD}^C	680	0.56 ± 0.28

Table 6.2: Results from the $\not{E}_T$ - E_T extrapolation study on QCD background

region 1 : W cuts

region 2 : 10 GeV $<$ $\not{E}_T$ $<$ 20 GeV

region 3 : 10 GeV $<$ $\not{E}_T$ $<$ 20 GeV

0.1 $<$ isolation $<$ 0.3

region 4 : 0.1 $<$ isolation $<$ 0.3

where the cuts listed are the only differences from the W selection criteria. We then use the equation

$$\text{QCD background} = \frac{N(4)}{N(3)} N(2) \tag{6.2}$$

where N(x) refers to the number of events found in region x. We found

$$N(2) = 69$$

$$N(3) = 88$$

$$N(4) = 1$$

Substituting into eq 6.2 yields a background estimate of 0.68 $\pm$ 0.68. This estimate should also be an upper limit. The term N(3) will contain some electrons from b decays while the term N(2) will contain electrons from b decays, W $\rightarrow e\nu$ decays, and W $\rightarrow \tau\nu$ decays. From Monte Carlo studies we can make rough estimates of the contributions to these terms and determine that the electron background in N(2) is larger. Since N(3) > N(2), subtracting the effect of the electron contamination will lower the background estimate.

To calculate the QCD background we used a weighted mean and sigma from the results of the 3 background studies. We then estimate the QCD background to be 0.6 $\pm$ 0.3.

6.2 Heavy quark background

Heavy quarks can produce background to W $\rightarrow e\nu$ events by decaying semi-leptonicly into a lepton, neutrino, and a lighter quark which we will refer to as the daughter quark. The p_T of the electron and neutrino are determined by the initial p_T of the heavy quark and by the boost given to the leptons from the decay process. The leptons must be produced with large p_T for the event to pass the W E_T and $\not\!\!E_T$ cuts (mismeasured energy and neutrinos from semi-leptonic decays of other quarks in the event can increase or decrease the $\not\!\!E_T$). The W selection cuts include an isolation requirement; consequently, the electron and daughter quark must receive enough

p_T transverse to the heavy quark p_T to insure that the daughter quark does not deposit too much energy in the isolation cone. Finally, there is a large probability that decay products from the quark which doesn't produce the isolated electron will cause the event to fail the dijet cut.

The relevant event characteristics depend significantly on the heavy quark mass. Heavy quarks are produced with p_T roughly equal to their mass [45]. B quarks have a much lower p_T distribution than t quarks, and the electron spectrum from b decays falls off more sharply than the spectrum from t decays. Figure 6.1 shows the lepton spectrum from b and t quark decays normalized to the same integrated luminosity. As the top mass increases, its lepton spectrum broadens due both to the increased p_T of the t quark and to the increased boost the lepton receives. A heavier quark mass will also produce more isolated electrons because the electron and daughter quark have a higher p_T spectrum in the heavy quark center of mass. On the other hand, heavy quark cross sections fall off with increasing mass. The $b\bar{b}$ cross section at the Tevatron is estimated to be 14-30 μb [46], whereas the $t\bar{t}$ cross section is at least a factor of 1000 smaller (see figure 6.3).

6.2.1 Bottom quark background

Since we expect the background from $b\bar{b}$ production to be low, we must generate the equivalent of several times our integrated luminosity of 25.3 nb^{-1} for an adequate

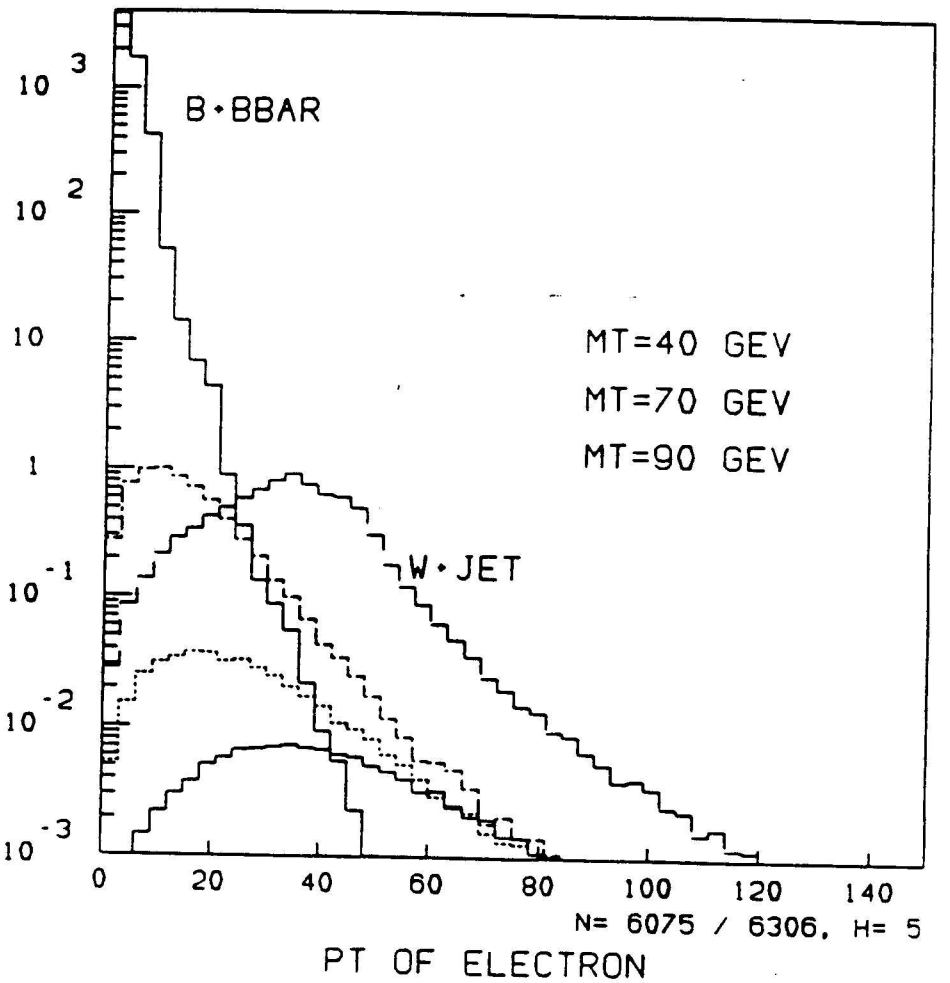

Figure 6.1: Lepton spectrum from b and t quark decays normalized to the same integrated luminosity. The 3 unlabelled curves are the lepton spectra from $t\bar{t}$ production at top masses of 40, 70, and 90 GeV (90 GeV curve is the lowest).

study. Assuming a cross section of 20 μb, there were roughly 500,000 $b\bar{b}$ events produced during the 1987 run. Generating and simulating several times this number of events requires too much computer time; therefore, we reduced the task by applying several cuts. W candidates were required to have an electron with $E_T > 15$ GeV. During Monte Carlo event generation, we required a b quark with greater than 10 GeV p_T , and after the quark decay, we required an electron with greater than 15 GeV p_T . Only events satisfying these criteria were run through the detector simulation.

Using these cuts, we were able to generate and simulate a sample of 389 $b\bar{b}$ events corresponding to 304 nb^{-1}. We then ran this sample through the W selection criteria. The number of events passing various stages in the analysis is shown in table 6.3. The largest factor causing these events to fail the selection criteria is the event $\not\!\!E_T$. Figure 6.2 shows the $\not\!\!E_T$ distribution for the $b\bar{b}$ events which have clusters found by the electron algorithm. Since b quarks are not in general produced with high p_T , the neutrino in a semi-leptonic decay will not have large enough p_T to pass the $\not\!\!E_T$ cut.

No events passed all the W selection criteria; therefore, we can put an upper limit on the $b\bar{b}$ background of

$$2.3 \times \frac{25.3}{304} = 0.19 \text{ events} \quad 90\%\text{C.L.}$$

W Selection Cut	Events
Total Sample	389
Electron Cluster Algorithm	325
$-1 < \eta < 1$	211
E_T	150
$\not\!\!E_T$	3
Dijet	0
Had/EM	0
E/p	0
Isolation	0

Table 6.3: Number of $b\bar{b}$ events passing the W selection cuts. The $b\bar{b}$ sample was required to have an electron with $p_T > 15$ GeV.

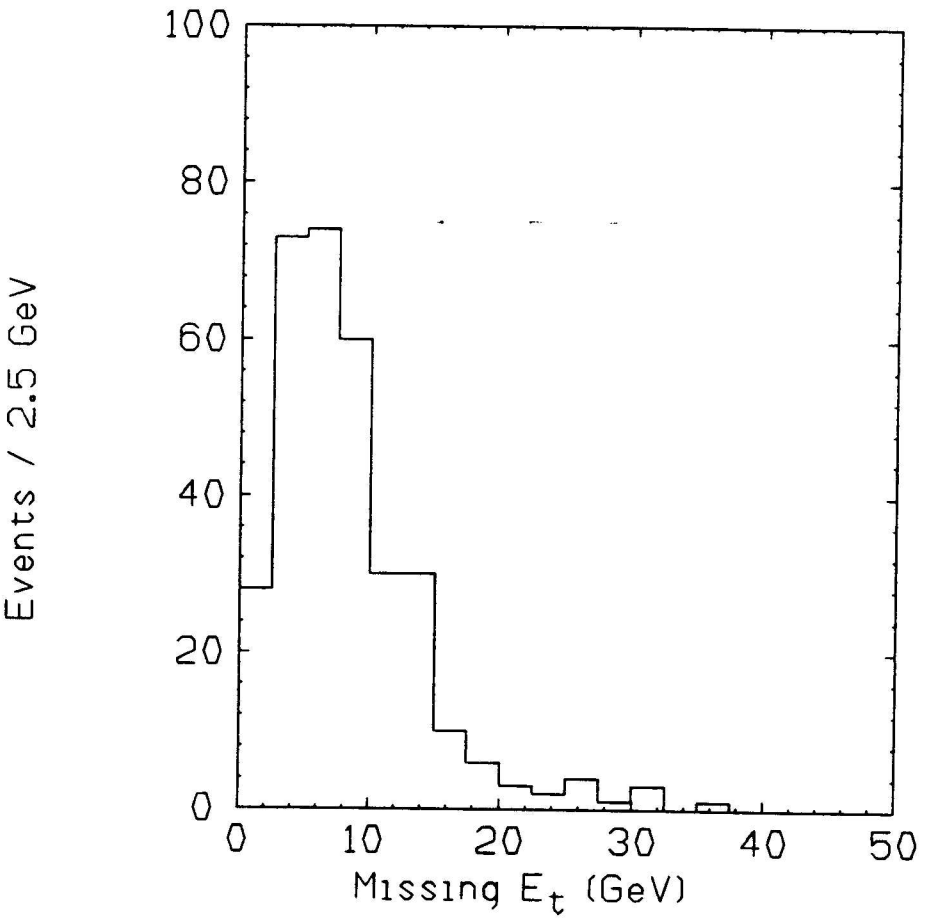

Figure 6.2: Distribution of $\not\!\!E_T$ from the Monte Carlo $b\bar{b}$ sample. Events in this plot were required to have an electron cluster reconstructed by the electron algorithm.

6.2.2 Top quark background

Top quarks may be produced directly as $t\bar{t}$ pairs or through the decay of a W to $t\bar{b}$ or $b\bar{t}$. Theoretical estimates of the cross sections for these processes as a function of the top mass are shown in figure 6.3 [47]. For low top masses, the tb cross section contributes significantly, but as the top mass increases, the available phase space decreases and the cross section falls off sharply.

Since we don't know the top quark mass, we simulated $t\bar{t}$ and tb decays at various top masses and ran the W selection cuts to estimate the contribution to the background. Table 6.4 shows the results of the Monte Carlo simulation and analysis of the top background. The backgrounds from the 2 production processes are summed and displayed in figure 6.4. The background peaks at a top mass of 60 GeV.

If the top quark mass is large enough, the cross section becomes too small to allow any contribution to the $W \rightarrow e\nu$ background. The limits on the background are then 0.0 - 0.3 events with no best estimate. We, therefore, take the top background to be $0.0^{+0.3}_{-0.0}$ events.

6.3 Tau decay

To estimate the background from the process $W \rightarrow \tau\nu$ we use a Monte Carlo program to generate the production and decay of the W and simulate the detector response. The E_T spectrum for electrons from the tau decay which enter the central calorimeter

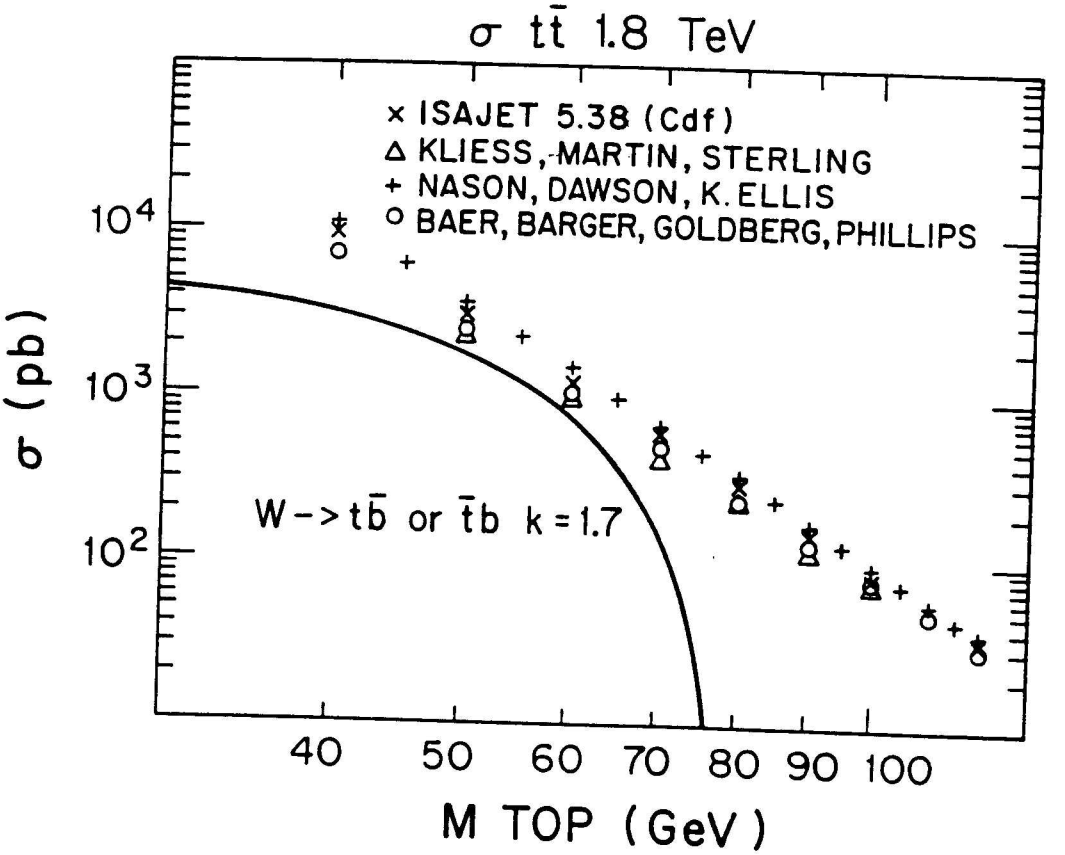

Figure 6.3: Top production cross section as a function of the top quark mass. The curve shows the cross section for tb production. The points show the expected cross section for $t\bar{t}$ production.

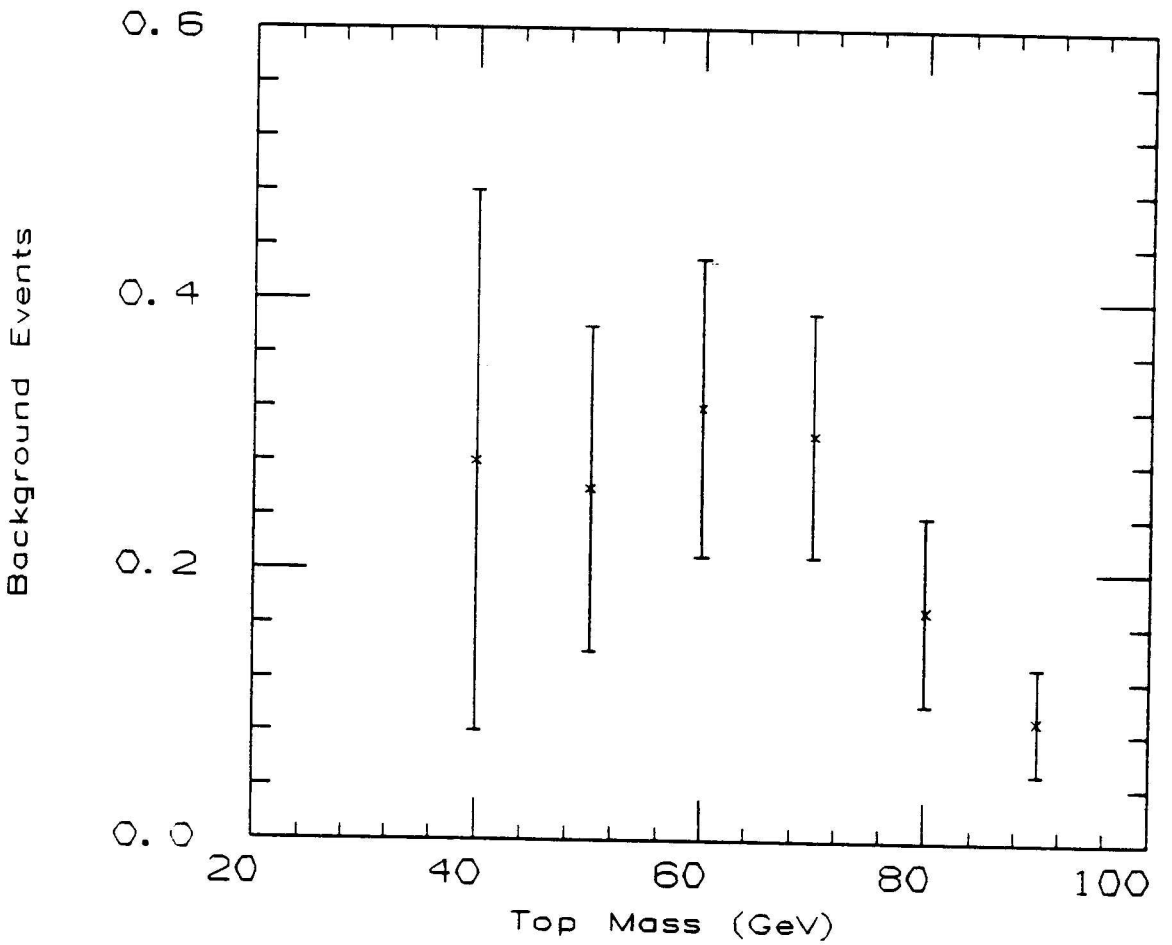

Figure 6.4: Background from top events versus the top mass.

Top Mass	Quarks Produced	σ (nb)	Integrated Luminosity (nb^{-1}	Events Passed	Background
40	$t\bar{t}$	9.4	183	2	0.28
	$t\bar{b}$ or $b\bar{t}$	4.75	421	0	< 0.05 (90% C.L.)
50	$t\bar{t}$	3.1	453	4	0.22
	$t\bar{b}$ or $b\bar{t}$	3.38	593	1	0.04
60	$t\bar{t}$	1.2	676	6	0.22
	$t\bar{b}$ or $b\bar{t}$	1.9	527	2	0.1
70	$t\bar{t}$	0.56	890	10	.28
	$t\bar{b}$ or $b\bar{t}$	0.63	1600	1	0.02
80	$t\bar{t}$	0.28	900	6	.17
	$t\bar{b}$ or $b\bar{t}$	-	-	-	-
90	$t\bar{t}$	0.15	1675	6	.09
	$t\bar{b}$ or $b\bar{t}$	-	-	-	-

Table 6.4: Summary of the results of top background studies.

is shown in figure 6.5. Also shown in this figure is the spectrum of the electrons from a direct W decay. Since the electrons from tau decays must share the energy with the extra neutrinos, the E_T spectrum is shifted to lower values and broadened.

To calculate the tau background we start with the equation

$$W_{\text{cand}} = W_e + W_\tau + B_{QCD} \tag{6.3}$$

where W_{cand} is the total number of W candidates in our sample, W_e is the number of W bosons in our sample decaying directly to electrons, W_τ is the number of W bosons in our sample decaying to taus and then electrons, and B_{QCD} is the QCD background. We have assumed that heavy quark background is negligible as calculated above. If we let W_l designate the number of W decays into any one type of lepton, then from lepton universality we may rewrite the terms W_e and W_τ as

$$W_e = W_l \times \epsilon_e \tag{6.4}$$

$$W_\tau = W_l \times \epsilon_\tau \tag{6.5}$$

where ϵ_e and ϵ_τ are the efficiencies for detecting the processes $W \rightarrow e\nu$ and $W \rightarrow \tau\nu$ with subsequent tau decay to an electron.

The term, ϵ_τ, is a product of 2 factors. First, the tau must decay to an electron and neutrinos so we must include the probability for this decay. Averaging data from recent experiments gives this probability as 0.177 ± 0.004 [48]. Second, our W cuts must select the event as a W candidate. The Monte Carlo studies estimate this

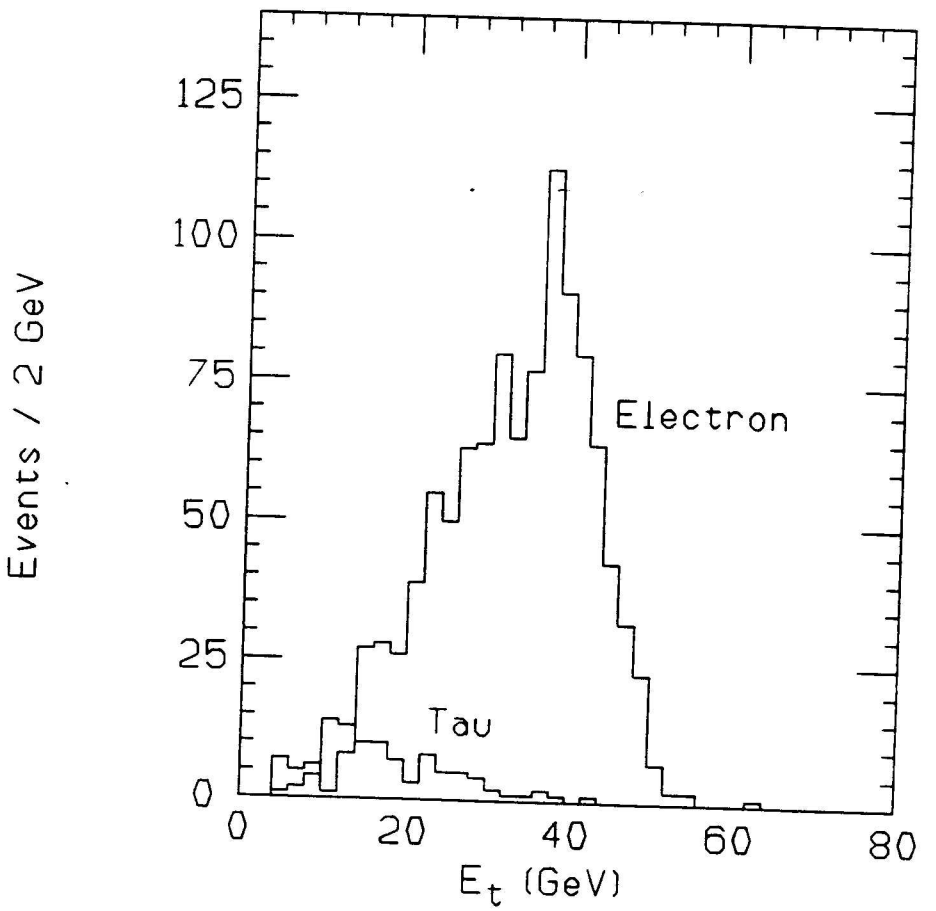

Figure 6.5: The E_T distribution for electron clusters in the central calorimeter for $W \rightarrow \tau\nu$ and $W \rightarrow e\nu$ events.

probability as 0.045 $\pm$ 0.005 where the error is statistical. The term ϵ_τ is then 0.008 $\pm$ 0.001. From section 5.3 we estimated the efficiency, ϵ_e to be 0.31 $\pm$ 0.03.

Substituting equations 6.4 and 6.5 into equation 6.3 and rewriting, we find

$$W_l = \frac{W_{\text{cand}} - B_{QCD}}{\epsilon_e + \epsilon_\tau} \tag{6.6}$$

Using the QCD background estimate, 0.6 $\pm$ 0.3, from section 6.1 we find $W_l = 64 \pm 6$. Finally, we may then substitute back into equation 6.5 and find $W_\tau = 0.5 \pm 0.1$.

Since the number of W $\rightarrow \tau\nu$ decays in our sample is so small, we can't see the contribution to the E_T spectrum.

Chapter 7

Results

7.1 Cross Section

The cross section for W production and decay into electron and neutrino is given by:

$$\sigma\left(p\bar{p} \rightarrow WX \rightarrow e\nu X\right) = \frac{(W \rightarrow e\nu)_{\text{Candidates}} - \text{Background}}{\int \mathcal{L}\text{dt} \times \epsilon} \tag{7.1}$$

where ϵ is the product of all efficiencies and acceptances. Table 5.6 gives a summary of the terms in equation 7.1 measured at $\sqrt{s} = 1.8$ TeV at the Fermilab Tevatron during the 1987 data run. Substituting, we calculate the result:

$$\sigma\left(p\bar{p} \rightarrow WX \rightarrow e\nu X\right) = 2.5 \pm 0.6 \pm 0.5\ nb \tag{7.2}$$

where the first error is statistical and the second error is systematic.

Figure 7.1 shows our cross section measurement with curves from theoretical calculations by Alterelli, Ellis, and Martinelli [49] and the cross section measurements from UA1 and UA2 at 630 GeV [50]. The theoretical prediction agrees with our measured result. The theoretical calculations assume a top quark mass of 50

Parameter	Value
$W \rightarrow e\nu$ candidates	21
Luminosity	25.3 ± 3.8 nb^{-1}
Backgrounds	
QCD	0.6 ± 0.3
W $\rightarrow \tau\nu$	0.5 ± 0.1
Heavy Quark	$0.0^{+0.3}_{-0.0}$
Efficiencies	
Had/EM	0.96 ± 0.04
Isolation	0.99 ± 0.01
Dijet	0.90 ± 0.03
Tracking	0.98 ± 0.01
Radiative	0.97 ± 0.01
Monte Carlo Acceptance	0.38 ± 0.03
Overall Acceptance (ϵ)	0.31 ± 0.03

Table 7.1: Summary of values used in cross section calculation

	W decay			Z decay		$\int \mathcal{L}dt$	
Experiment	$e\nu$	$\mu\nu$	$\tau\nu$	ee	$\mu\mu$	546 GeV	630 GeV
UA1	299	67	32	33	19	136 nb^{-1}	568 nb^{-1}
UA2	248			39		142 nb^{-1}	768 nb^{-1}

Table 7.2: World's present published W and Z sample.

GeV. If the top quark mass is larger, the W $\rightarrow tb$ branching ratio decreases, and the W $\rightarrow e\nu$ branching ratio increases. The maximum W $\rightarrow e\nu$ branching ratio occurs when the top quark mass exceeds the W mass so the decay $W \rightarrow tX$ is kinematicly forbidden. In this case the theoretical cross section shown in figure 7.1 would increase by 13%.

The integrated luminosity for the 1988-89 colliding beam run at Fermilab should total 2-4 pb^{-1}. Using a reasonable efficiency estimate which includes the full detector acceptance, we should select between 2500 and 5000 W $\rightarrow e\nu$ events. Table 7.2 shows the world's published sample of W bosons and Z bosons through 1987 [53,54]. The UA2 experiment will have 2 runs during 1988-89 and hopes to write 10 pb^{-1} to tape [55]. Based on their measured cross section and efficiencies, they can then expect to have roughly 2500 W $\rightarrow e\nu$ candidates. Similarly, the 1988-89 CDF data run should produce a significantly larger number of Z, W $\rightarrow \mu\nu$, and W $\rightarrow \tau\nu$ candidates than the present sample. CDF's current cross section value has an error dominated by statistics. The 1988-89 results will contain errors limited only by the luminosity

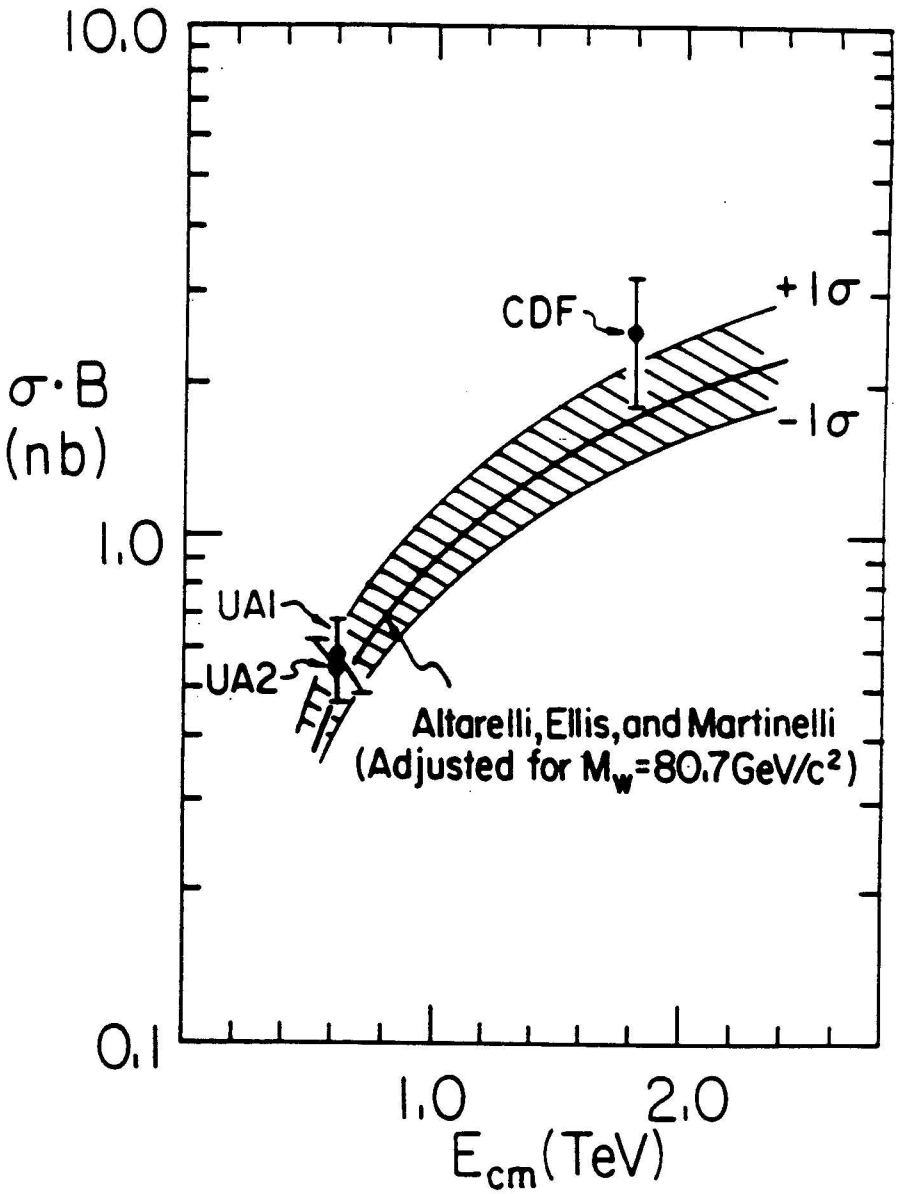

Figure 7.1: Cross section times branching ratio for W $\rightarrow e\nu$ versus center-of-mass energy. The curves represent theoretical predictions with error bars.

measurement. Certain interesting results depend on the ratio, R, of the 2 cross sections, $\sigma(p\bar{p} \rightarrow WX \rightarrow e\nu X)$ and $\sigma(p\bar{p} \rightarrow ZX \rightarrow eeX)$. The top mass, the number of light neutrinos, and R are related such that knowing any 2 determines the third [56,57]. Many systematic errors, such as those associated with the luminosity and electron identification, cancel when calculating this ratio. The large samples expected from the 1988-89 run will enable a much more accurate measurement of R.

7.2 Mass measurement

We can measure the W mass by fitting the electron p_T spectrum or the W m_T spectrum to Monte Carlo generated distributions. The m_T spectrum is less sensitive to the W p_T than the electron p_T spectrum, and therefore, can yield a better measurement of the W mass.

To fit the m_T spectrum, we simulated the m_T spectrum of W bosons with masses 76, 78, 80, 82, and 84 GeV. The decay $W \rightarrow \tau\nu$ with the tau decaying to an electron and neutrinos can affect the mass measurement by adding events on the lower tail of the m_T distribution; therefore, we reduced this effect by requiring the m_T to be greater than 52 GeV. We calculated the χ^2 for the W candidates and the Monte Carlo distributions using 8 GeV bins beginning at 52 GeV. Figure 7.2 shows these χ^2 values as a function of the generated W mass. We fit these points to a quadratic function which has a minimum at 79.5 GeV with a statistical error of 2.9 GeV. The

error is determined by varying the minimum χ^2 value by one unit and finding the corresponding mass values.

There are several contributions to the systematic error. The overall energy scale may have an absolute error associated with it. We can estimate the potential error in the overall energy scale by comparing calorimeter electron cluster energy and the CTC electron track p_T . The mean of the E/p distribution (see figure 4.10) excluding the events with E/p > 1.5 is 1.029. Electron bremsstrahlung will result in average p_T values slightly lower than cluster E_T values; consequently, the E/p ratio will have a mean greater than 1.0. This effect is on the order of 1.0%. We can place an upper limit on the energy scale error by ignoring the 1.0% effect and taking the error to be 2.9%.

The $\not\!\!E_T$ error is caused by the electron cluster energy resolution, the $\not\!\!E_T$ energy resolution for the "underlying event", and the $\not\!\!E_T$ offset errors (see section 4.5.2). The energy resolutions are included in the Monte Carlo detector simulations. An upper limit on the offset error was obtained by assuming the error is equal to the value of the offset. We then recalculated the m_T of the W candidates and repeated the χ^2 analysis to find m_T = 78.9 GeV. We then estimate the m_T error due to the $\not\!\!E_T$ offsets as 0.6 GeV.

The $\not\!\!E_T$ offset error is in principle only a lower error; however, since it adds very little to the energy scale error, we add it in quadrature. Our W mass measurement

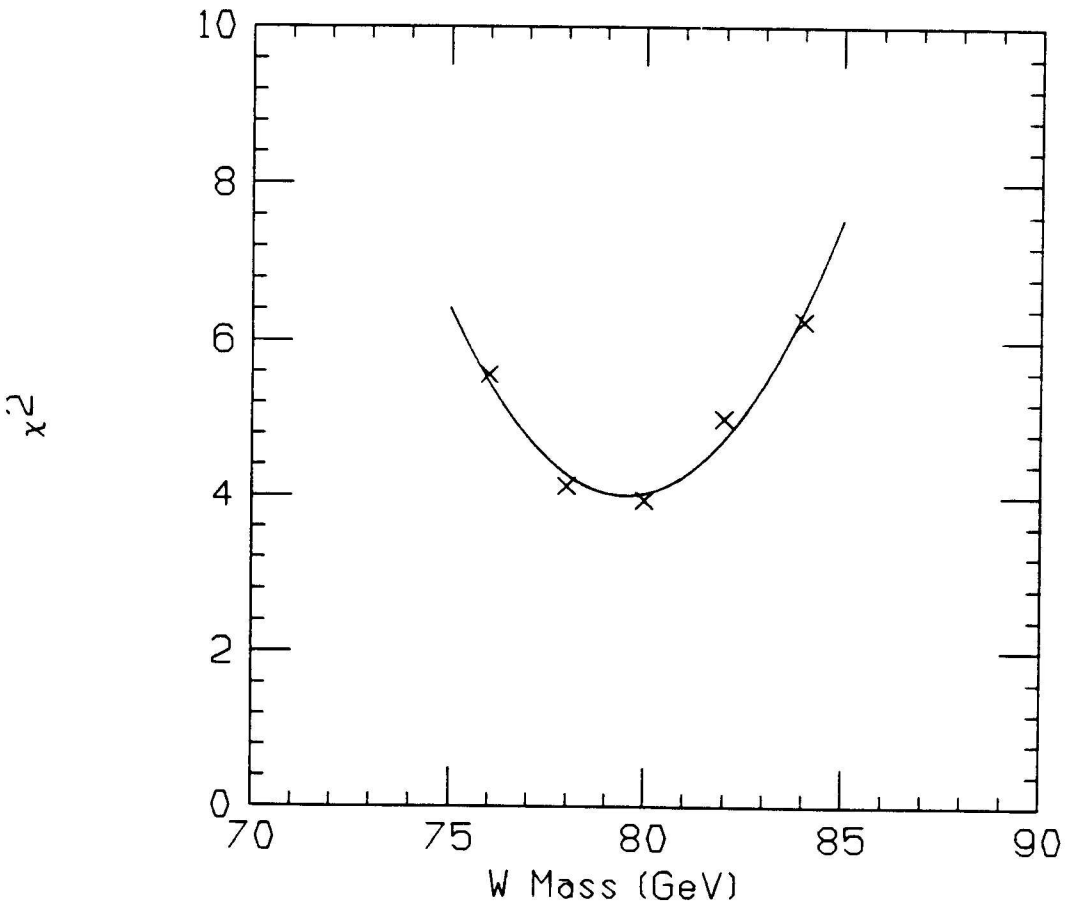

Figure 7.2: χ^2 values from fitting Monte Carlo m_T distributions to W candidates with the requirement $m_T > 52$ GeV. The curve is a quadratic fit to the χ^2 points and has a minimum at 79.5 ± 2.9 GeV.

then becomes $79.5 \pm 2.9 \pm 2.4$ GeV where the first error is statistical and the second is systematic. This measurement agrees with values from the UA experiments at CERN:

$$W_M = 80.2 \pm 0.6\ (\text{stat}) \pm 0.5\ (\text{sys}_1) \pm 1.3\ (\text{sys}_2)\ \text{GeV} \quad \text{UA2 [51]}$$

$$W_M = 83.5^{+1.1}_{-1.0} \pm 2.7\ (\text{syst})\text{GeV} \quad \text{UA1 [52]}$$

Figure 7.3 shows the transverse mass distribution for the 21 W candidates with a curve from Monte Carlo events generated with $M_W = 79.5$ GeV.

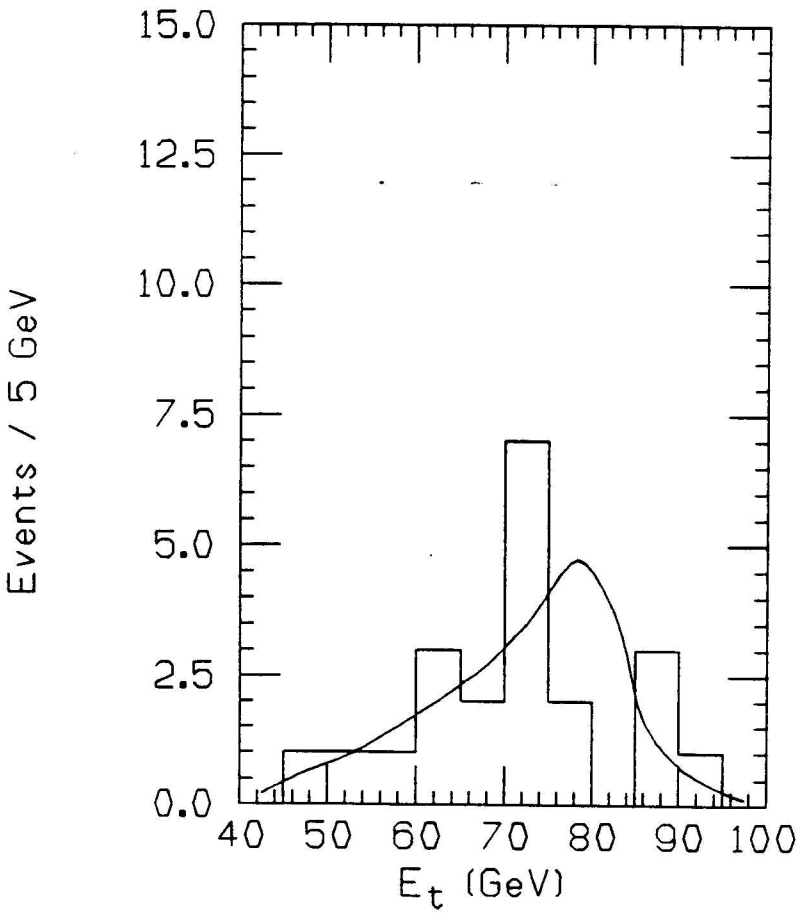

Figure 7.3: Transverse mass distribution for the 21 W candidates. The curve is a normalized transverse mass distribution from Monte Carlo generated events with M_W = 79.5 GeV.

Appendix A

Calibration of the Central Electromagnetic Calorimeter

A.1 Introduction

The design goal for calibration of the central EM calorimeter is 1% accuracy over the course of the experiment. In order to meet this goal several calibration systems and procedures were implemented. The systems are the ^{137}Cs source and its associated drive, the xenon flasher, the LED flasher, and electronic charge and current injection. These systems are described in some detail in chapter 3 and in greater detail in reference [21]. Experience gained from other experiments indicated that quality control during construction of the calorimeter greatly aids accurate calibration. Large variations in response from channel to channel require more difficult and time consuming calibration procedures. Considerable effort was given to reducing response variations during construction [18]. Instead of calibrating some wedges in a testbeam and extrapolating this calibration to all the other wedges, we chose to calibrate every wedge in the testbeam. We also wanted the ability to calibrate frequently and accurately

during data taking periods. This requirement led us to design a source calibration system which contained a remote controlled, movable, radioactive source which would allow us to calibrate while the detector was sealed in the collision hall.

The basic philosophy of the central EM calorimeter calibration is that calorimeter response to radioactive sources can be used to accurately monitor changes in the energy response to incident particles. Each phototube on every wedge was initially calibrated by measuring both its response to electrons of a known energy and its response to the ^{137}Cs source as it passed through the tower during a source run. Changes in the calorimeter response for energy deposited by incident particles are proportional to changes in the calorimeter response to the source. Subsequent source runs may then be used to track calorimeter response changes.

There are several ways the calorimeter response can change. Scintillator may deteriorate due to damage to the fluors or a decrease in the transparency of the scintillator base. The light collection efficiency may change either because the wavelength shifter or lightguide deteriorate or because the optical coupling between components may vary over time. Phototube gains depend strongly on the high voltage applied across the dynodes. This high voltage may drift and cause gain changes. Finally, the intrinsic phototube gain may vary with time.

There are some subtle effects which can result in source runs not accurately monitoring the calorimeter response. ^{137}Cs undergoes beta decay and emits electrons and

photons with energies 1.2 MeV maximum and .66 MeV respectively. Since the decay particles have relatively little energy, they will not penetrate to deposit energy in many layers of the calorimeter, and therefore, will only "sample" a small fraction of these layers. While it's unlikely that individual scintillator layers will deteriorate at a significantly different rate than others, small changes in the coupling of light from the scintillator to the wavelength shifter may result from transporting and handling the wedges. Preliminary results indicate that effects of this type are small (see section A.5).

Source runs provide gain monitoring on time scales of weeks or longer, but phototube gains may change significantly on time scales of days. The flasher systems (xenon and LED) are used to monitor short term variations. The flashers deposit light either in the wavelength shifter (xenon flasher) or the phototube transition piece (LED flasher), and consequently, do not monitor scintillator changes. For this reason they cannot be reliably used to measure long term variations. Flasher runs can be taken immediately after source calibration, and then subsequent flasher runs may monitor the gain changes until the next source run.

A.2 Calibration Measurements

During physics runs, front-end scanners read out calorimeter channels after digitization. The read out for each channel is multiplied by its corresponding calibration

constant which corrects for channel to channel gain variation. The constants are divided by a nominal gain such that the result is near unity, therefore, retaining a large fraction of the original 16-bit dynamic range of the ADC. Later, each channel can be converted to units of energy by multiplying by the nominal gain.

We have verified that the integrated charge, q, measured through the charge channels remains proportional to the ^{137}Cs source peak current, i, measured through the current channels. Therefore, for 2 different times, t_1 and t_2, we can write:

$$\frac{q(t_1)}{i(t_1)} = \frac{q(t_2)}{i(t_2)} \tag{A.1}$$

The energy gain [58], G_E, for a phototube (GeV/count) can be written in terms of the testbeam energy gain found at time t_0, source run measurements I (counts), charge channel electronic gains G_Q (fC/count), and current channel electronic gains G_I (nA/count):

$$G_E(t) = \frac{G_Q(t)}{G_Q(t_0)} \frac{I(t_0)}{I(t)} \frac{G_I(t_0)}{G_I(t)} G_E(t_0) \tag{A.2}$$

The source current terms contain correction factors for the decay of the source. The dimensionless channel to channel gain G'_E is then defined as:

$$G'_E(t) = \frac{G_E(t)}{G_E(\text{nominal})} \tag{A.3}$$

where G_E(nominal) is a constant for all calorimeter channels. Short term corrections to source calibrations taken at time t_1 can be made with the flasher systems using

the equation:

$$G_E(t) = \frac{G_Q(t)}{G_Q(t_1)} \frac{Q_f(t_1)}{Q_f(t)} G_E(t_1) \tag{A.4}$$

where Q_f is the channel response in counts to the flasher run.

After calibration runs, the responses are stored in a calibration data base, and the latest version of the dimensionless gain, G'_E, is downloaded to the front-end scanners. Details of testbeam measurements and calibration results are discussed below.

A.3 Testbeam Measurements

During testbeam operation, many studies were performed to understand the detector response. These included varying the electron energy to measure the linearity of the detector response, varying the incident electron position to find the tower response map, determining the response near ϕ boundaries, and performing the basic energy calibration.

During 1984 and 1985, the 50 central wedges (48 for the detector and 2 spare) were calibrated in the Fermilab NW testbeam. The EM calibration consisted of 50 GeV electron runs and a corresponding ^{137}Cs source run. Each phototube has a calibration constant given by the charge response to the electron run divided by the current response to the source runs. A description of these calibration runs follows.

A.3.1 Electron runs

Electron runs consisted of measuring the phototube charge response to 50 GeV electrons incident on tower center for towers 0-8. Tower 9 has a significantly different shape from the other towers, and we decided not to calibrate at tower center. We scanned across the tower in the θ direction and used the position where the response was highest as the calibration point. The electron response was recorded separately for both tubes in the tower.

We made several cuts on electron events to ensure the electron position was close to tower center and to ensure that the electron momentum was well measured. We used strip chamber position information to require the electron to be within 1 cm in ϕ of tower center. The 2 photomultipliers collecting light from each tower will then share the deposited energy equally. The electron momentum was determined by 2 beam chambers on either side of a dipole bending magnet. If the electron momentum could not be reconstructed, the event was discarded. The energy response was then normalized to a 50 GeV/c electron. Roughly 200 events were taken at each calibration point. The energy resolution of the EM calorimeter is $\sigma/\mathrm{E} = 0.14\%/\sqrt{\mathrm{E}}$ so the statistical error on the calibration value is roughly 0.15%. The systematic error on the electron momentum resolution is 0.3%. Errors due to uncertainties in the gains of the charge channels which measure the electron response and the current channels which measure the source response are less than 0.25% and 0.15% respectively.

A.3.2 ^{137}Cs source runs

For each electron run, there were one or more source runs taken within a few hours of the electron run. A source run consisted of moving the source through all 10 towers such that a current peak could be measured for each phototube (see figure 3.8) Various schemes were tested to determine how best to measure the peak current value. We chose an algorithm which subtracts off the dark current (the flat region of the current response which occurs when the source is not in the tower) and fits the points in the top 20% of the signal to a 6^{th} order polynomial.

This procedure works very well; however, there are certain features of source runs which may result in an inaccurate fit or no fit. To ensure that the testbeam source calibration runs produced reliable data, runs were taken until at least one pair agreed to better than 1% for every phototube channel. In some cases this requirement was dropped if many runs were taken with no such agreement. In general 4-6 source runs were taken for each electron calibration.

To produce a single calibration current value for each phototube, we averaged all runs, throwing out any values which differed from the mean by over 5 standard deviations. Since the ^{137}Cs sources decay, we must correct for the decay by adjusting the peak current value taking into account when the run was done. The systematic error from run to run dominates the error from fitting the source peak and the current channel gain error; therefore, we used this systematic error as the calibration error.

A.4 Maintaining the Calibration

The use of remote controlled, permanently mounted sources has several advantages. Source calibration may be done easily and quickly. All 48 wedges are calibrated simultaneously, and source runs on the EM calorimeter can be completed in under an hour. Source runs may be taken regularly during data taking periods; however, the current channels can register large noise spikes from beam spray so source runs cannot be taken when there is beam in the Fermilab Main Ring or Tevatron. In general, source calibration is done every 2-4 weeks during data taking periods. Typically flasher runs are taken 3-4 times per week.

A.5 Results

The gain of the calorimeter should remain essentially constant over periods of minutes. We can then determine the reproducibility of the various calibration systems by taking several runs within a short time span and comparing them. During data taking, we generally do 4 EM source runs spaced roughly 10 min apart. Figure A.1 shows a comparison of 2 such runs. The results from all 956 phototubes in the EM calorimeter are included except for a few channels where the algorithm which fits the current peak failed due to cosmic rays or electronic noise. The percentage difference has a standard deviation of 0.6%.

Attempts were made to understand if there were systematic effects due to the

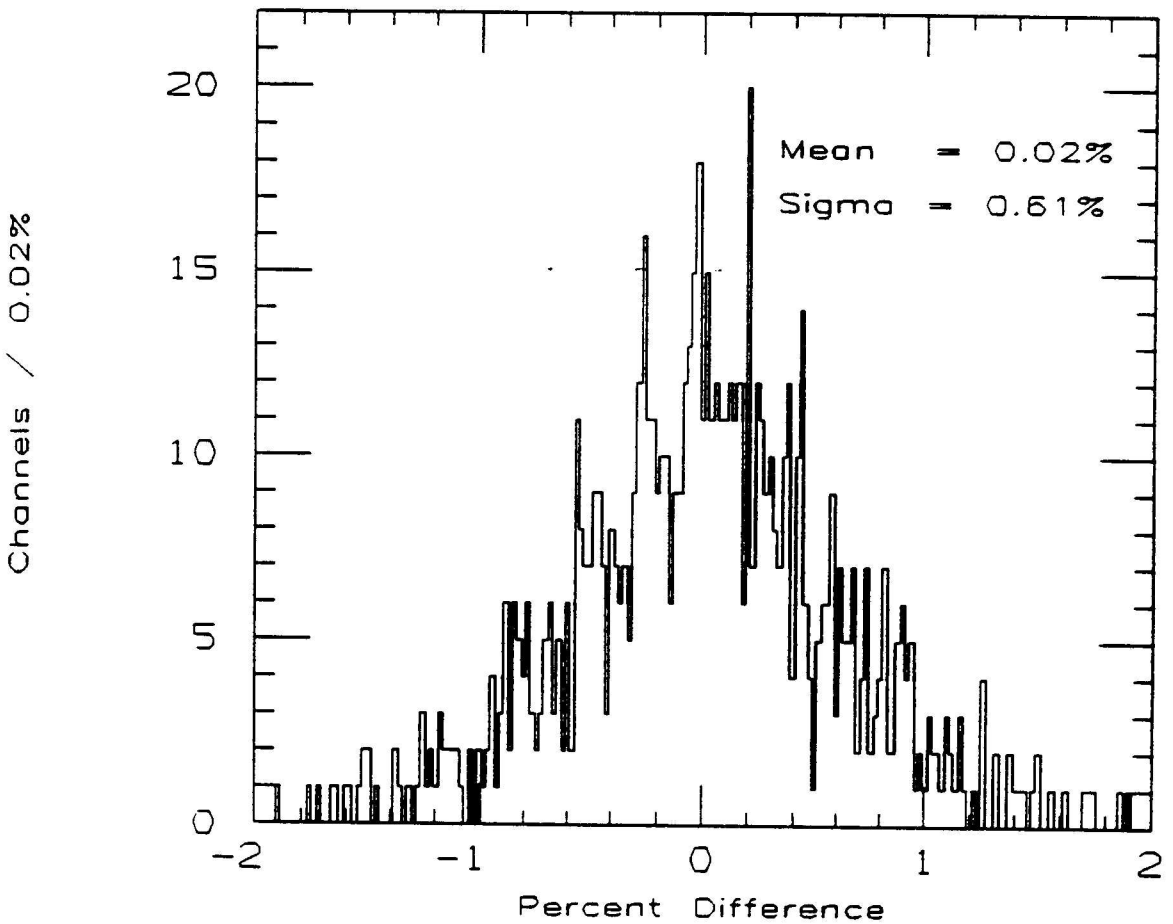

Figure A.1: Comparison of 2 ^{137}Cs source runs taken minutes apart. The distribution is the percentage difference defined as (Run2 - Run1)/Run1 $\times$ 100.

construction of the source drive apparatus which contribute to the run to run variation in the current response. During installation of the source drive system, a cylindrical brass capsule was tied to a nylon covered, steel wire loop which transports the source through the wedge. The sources were then placed inside cavities in the capsule, and solder filled the cavity to keep the source in place. As the source travels through the wedge, the wire twists rotating the capsule. Since the source tube sits directly over the strip chamber, the source deposits more energy in the layers of scintillator above the tube than those below the tube. Asymmetries in the cavities drilled in the capsules coupled with uneven solder flow on the capsule surface can result in asymmetric energy deposition.

This possibility was tested by driving the source into a fixed position in the wedge and measuring the source current while twisting the wire. The variation in response as a function of the source orientation in the tube was a significant fraction of the run to run error. Given the existing design, there was no clear way to prevent the source from rotating as it passed through the wedge, and therefore, this contribution to the run to run variation could not be eliminated.

The xenon flash bulb output varies considerably from flash to flash (see figure A.2a). The mean light deposited also varies for different bulbs and corresponds to a 20-40 GeV electron depositing all its energy in the tower. To reduce the spread in the distribution, the bulbs are monitored by PIN diodes. Normalizing the raw pho-

totube distributions to the PIN diode outputs reduces the standard deviation from roughly 15% to values around 2% (see figure A.2c). The light output from the LED flasher has a much narrower spread in energy with a standard deviation of 0.8%, and the light deposited is equivalent to a 200-300 GeV electron.

Flasher runs generally consist of 200-250 events so statistical errors on the normalized phototube signal for the xenon flasher and the raw phototube signal for the LED flasher are near 0.15% and 0.05% respectively. Figure A.3 shows the reproducibility of flasher runs taken roughly a day apart.

All 50 wedges were calibrated with at least one electron run and one set of corresponding source runs. Most wedges were kept at the testbeam long enough to perform 2 such calibrations and these values were combined to form one calibration constant. Three wedges were calibrated, removed from the testbeam area, and brought back roughly one month later to be calibrated again. These studies allowed us to test the assumption that source runs accurately track the overall calorimeter response to particles incident on the calorimeter.

Figure A.4 shows the percentage difference in calibration constants measured about one month apart for the 3 wedges. The constants are the ratio of the electron charge response to the ^{137}Cs current response. There is an overall 0.2% shift in the mean which corresponds to the decay in the ^{137}Cs source over the one month period ($t_{1/2}$ = 30.17 years). The distribution shows a sigma of 0.7%, and since each

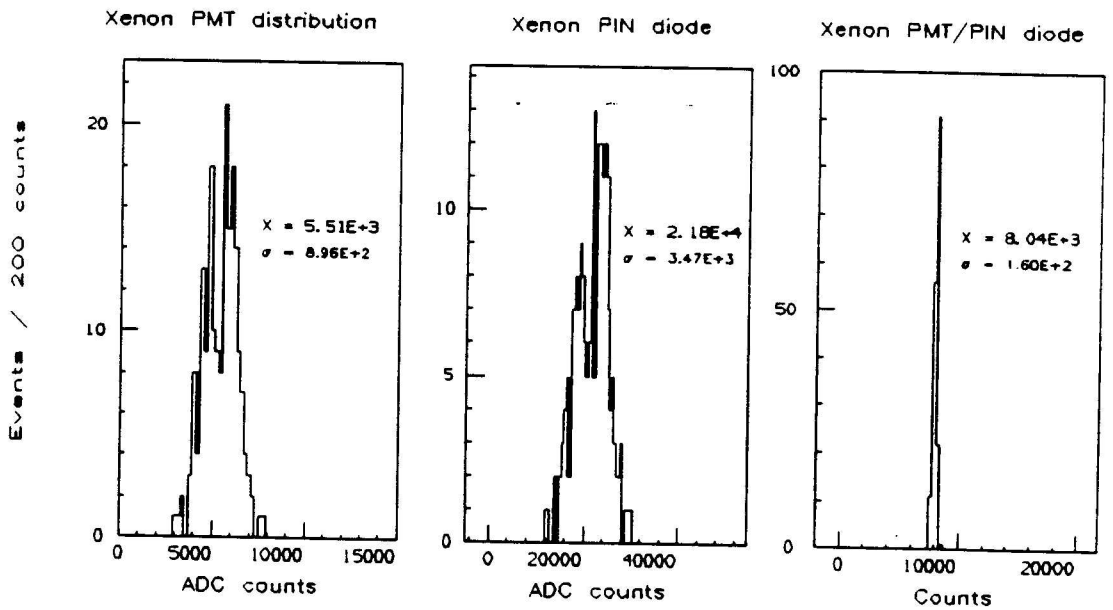

Figure A.2: Typical xenon flasher distributions. (a) Distribution of raw phototube signals. (b) Distribution of the PIN diode signals. (c) Distribution of the ratio of raw phototube signals to PIN diode signals (in dimensionless units).

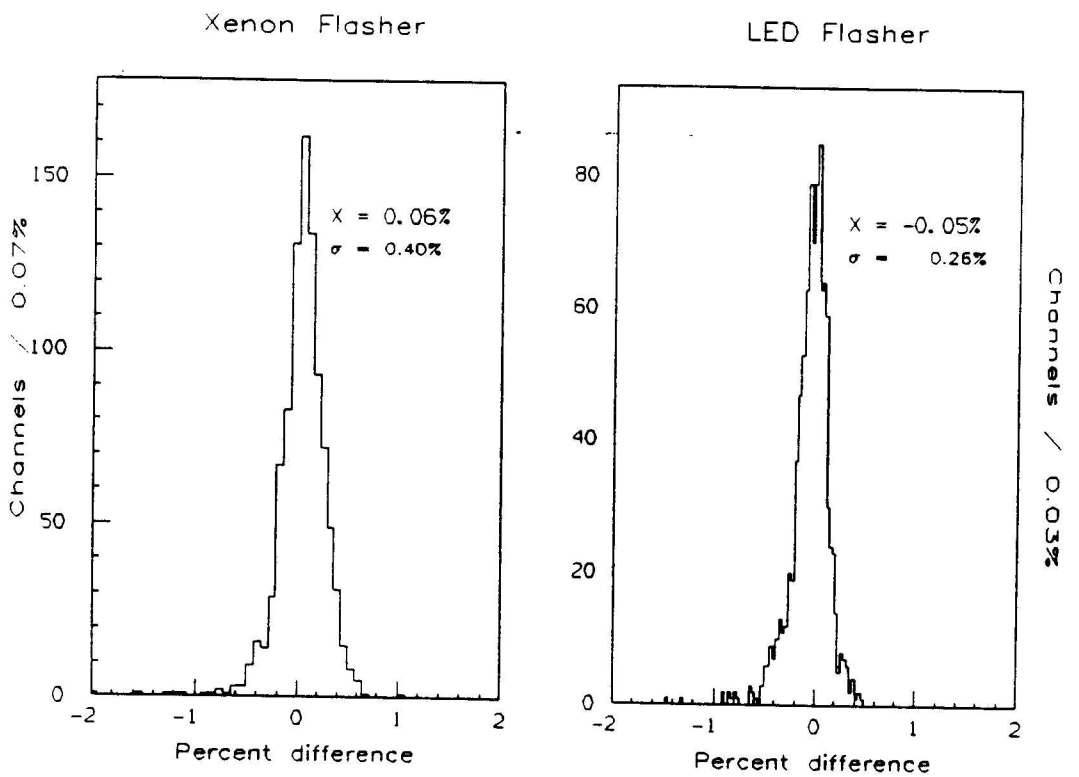

Figure A.3: Comparisons of 2 xenon flasher and LED flasher runs taken roughly one day apart. The ratio of phototube to PIN diode is used for xenon flasher runs while the raw phototube is used for LED flasher runs.

point represents 2 measurements, the calibration reproducibility is 0.4%. The source tracks the calorimeter gain accurately, and handling of the wedges does not appear to result in variations in individual scintillator layer response.

We would like the channel to channel variation in gain to be small. Uniform gain maximizes the dynamic range available, simplifies the triggering scheme, and allows easier and more accurate calibration. Although attempts were made during construction to minimize the variation between wedges and between towers in a single wedge, individual channel gains differ due to tower non-uniformities. The phototube high voltages on all channels were set to yield 2 pC per GeV of energy deposited in the tower. One method of achieving this gain is to use testbeam electrons of known energy and vary the high voltage to give the proper output. This method was rejected because it wastes too much valuable testbeam time. Instead we used radioactive sources and varied the high voltage until the current channel output during the source run equalled the fixed target value. Since a different source is mounted on each wedge, we must measure the source activity and correct for this variation. The accuracy of the source run method is limited by the tower-to-tower variation in calorimeter response, the reproducibility of source runs, and the error in the measurement of the source activity. The source activity was measured to 1.7% accuracy. Averaging 4 ^{137}Cs source run current values gives roughly a 0.3% error. From these numbers and the distribution of gains from testbeam data, we can calculate the tower to tower

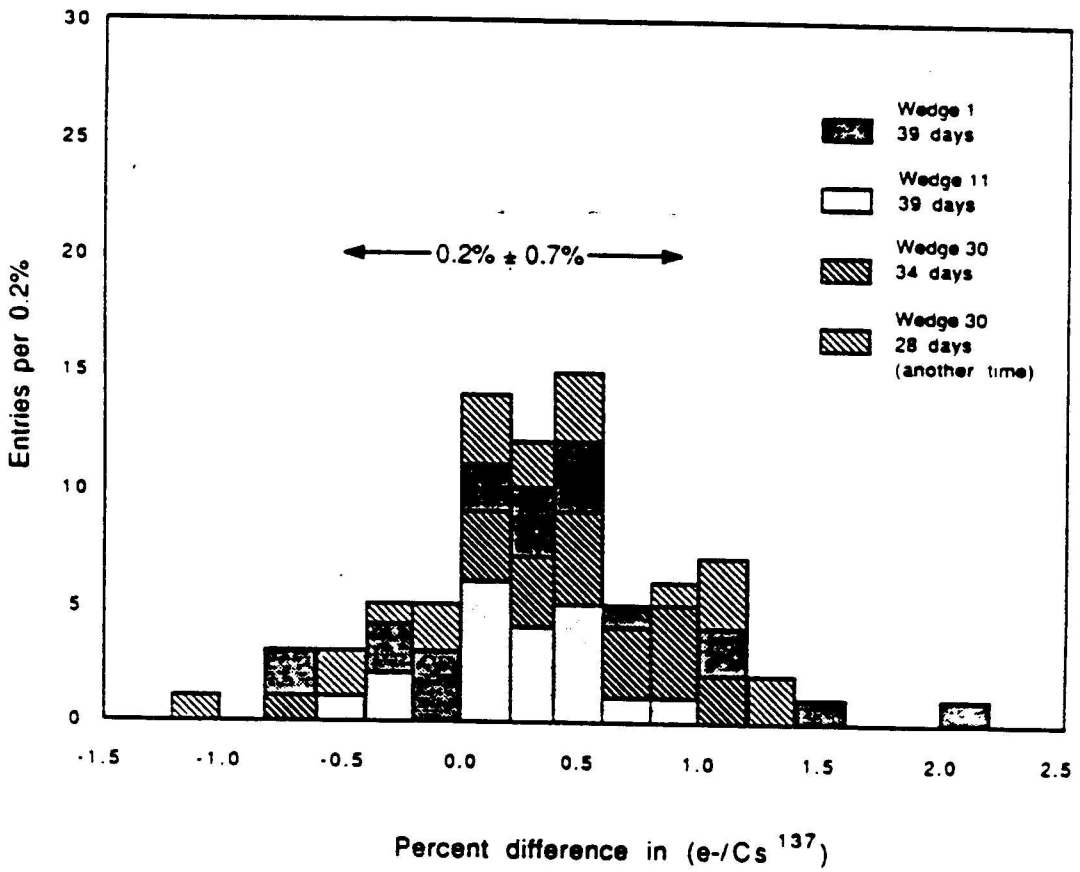

Figure A.4: Calibration reproducibility. The difference in electron to ^{137}Cs source response is shown for each tube for calibrations taken roughly 5 weeks apart. The 0.2% shift in the mean corresponds to the decay of the ^{137}Cs source.

variation in calorimeter response. Figure A.5 shows the calorimeter charge channel response to 50 GeV testbeam electrons from calibration runs on 20 wedges. The mean of the distribution is 2.04 pC/GeV, and the standard deviation is 2.91%. Unfolding the errors from source activity and source run reproducibility yields a tower to tower variation in construction of roughly 2.35%.

Figure A.6 shows the calorimeter response uniformity during calibration in the testbeam and after monitoring for several years. The results are given as a ratio of the channel gain to the nominal design gain (equivalent to 100 pC per phototube for a 50 GeV electron times the design electronic charge channel gain). Figure A.6b indicates that the mean of the calorimeter gains is 1% off the design value with a sigma of 4%. There is a tail on the upper end of the distribution which consists almost entirely of phototubes in tower 9. Tower 9 has a significantly different shape from the other towers (see figure 3.3) and the response to electrons is lower. If phototubes from tower 9 are eliminated from the distribution, the mean is 1.00.

Figure A.6a shows how the calorimeter uniformity has changed with time. This distribution comes from calibrations taken during the 1987 run. The mean and rms are 1.03 ± 0.08. The mean has changed due to deterioration of the response caused by aging, and there is a slight increase in the spread. Figure A.7 shows the percentage change in the gains between the testbeam values and those measured during the 1987 run.

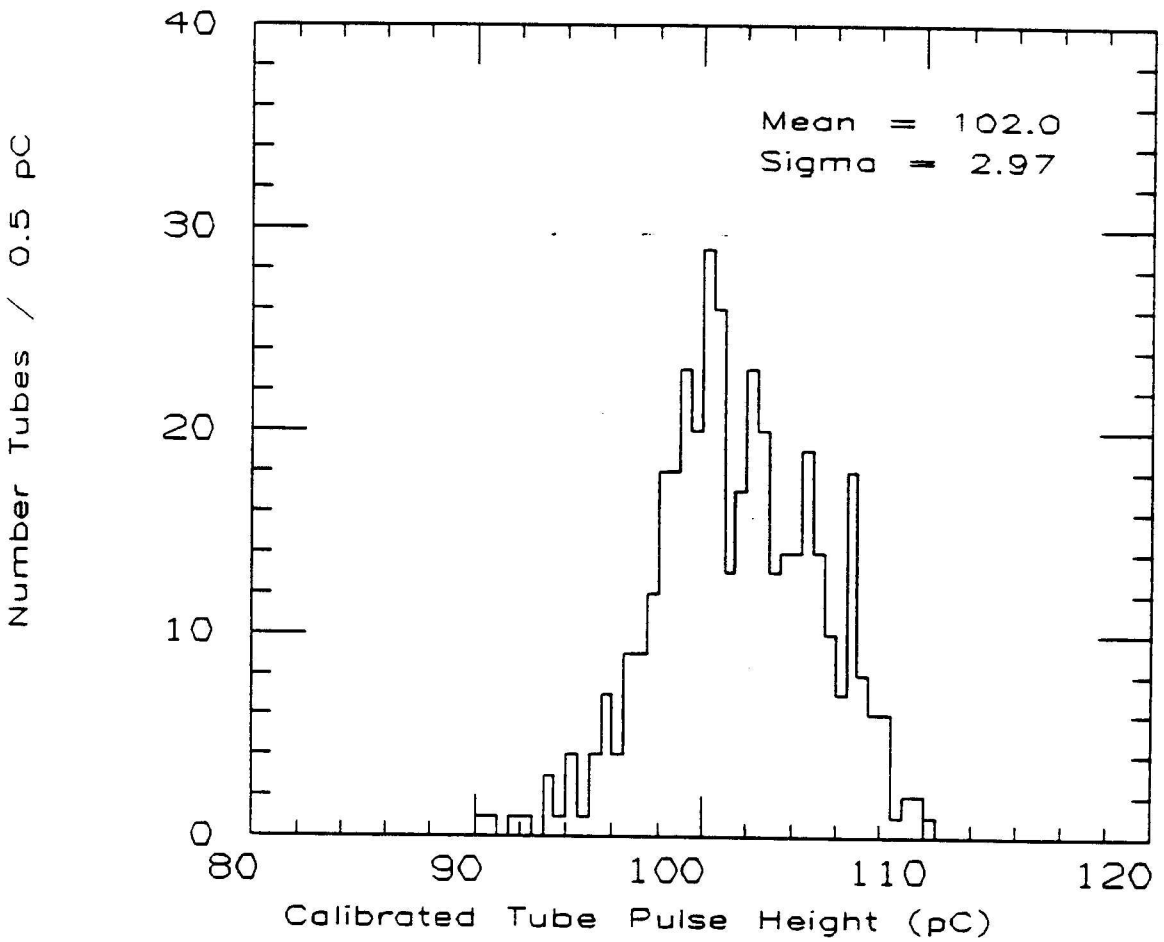

Figure A.5: Distribution of the charge channel response to 50 GeV testbeam electrons for 20 wedges.

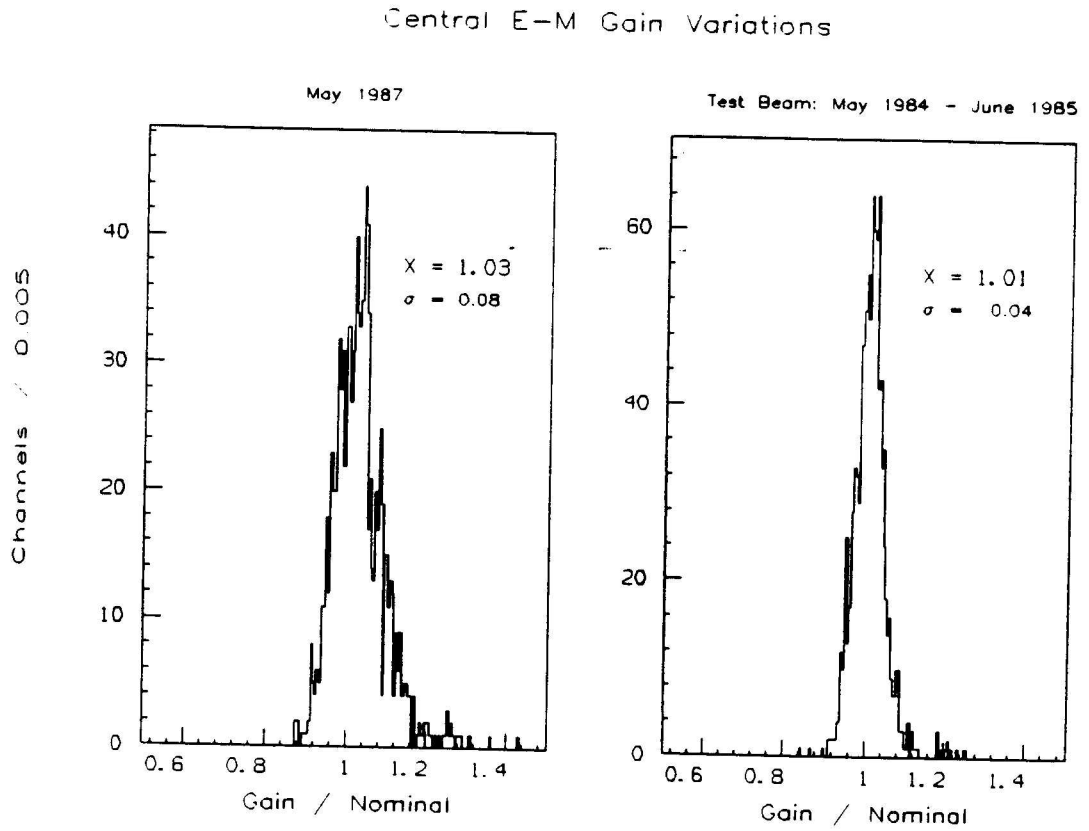

Figure A.6: Calibration uniformity. (a) Distribution of the channel to channel gain variation for all central EM calorimeter channels measured in May 1987. (b) Distribution of the same quantity taken at the testbeam from May 1984 to June 1985.

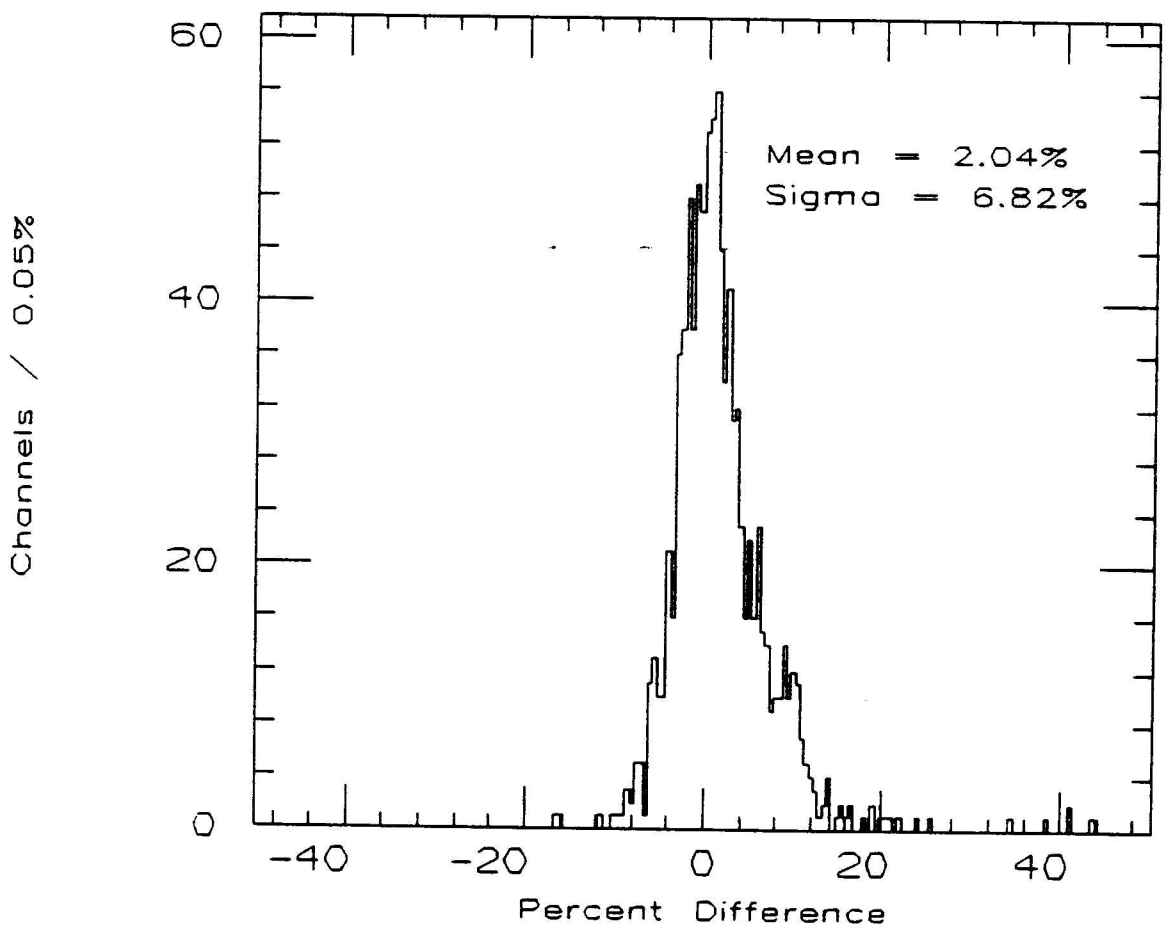

Figure A.7: Percentage difference between calorimeter gains measured during the 1987 run (May) and those measured at the testbeam.

All calibration runs are kept in a database, and we are able to look at trends in channel gains by looking at the channel history. Figure A.8 shows the calibration history for 4 tubes chosen to exhibit typical trends. The source current is plotted versus run number over a period of about 9 months. The vast majority of phototubes exhibit a flat response with time as shown in figure A.8a. A small number of tubes exhibit slowly rising or falling responses and occasionally abrupt changes are seen. The main cause for these variations are changes in the phototube gains either through high voltage changes or intrinsic phototube changes.

During testbeam calibration, there was no magnetic field present; however, during data taking the solenoidal magnetic field is turned on. A simple magnetic field model of the detector predicts a field in the EM calorimeter which is essentially parallel to the scintillator layers and which varies from 120 G to 860 G. Near the outside of the arches where the phototubes sit, the field should be roughly 20-40 G. The EM phototubes have sufficient iron and mu-metal shielding to prevent the solenoidal field from affecting the tubes.

Studies of the calorimeter response to the ^{137}Cs source as a function of the solenoidal field show a significant increase in gain (see figure A.9). Similar studies with the LED flasher show no such increase. The LED flasher deposits light into the photomultiplier transition pieces whereas the source deposits energy directly into the scintillator. These studies indicate that the magnetic field affects the scintillator

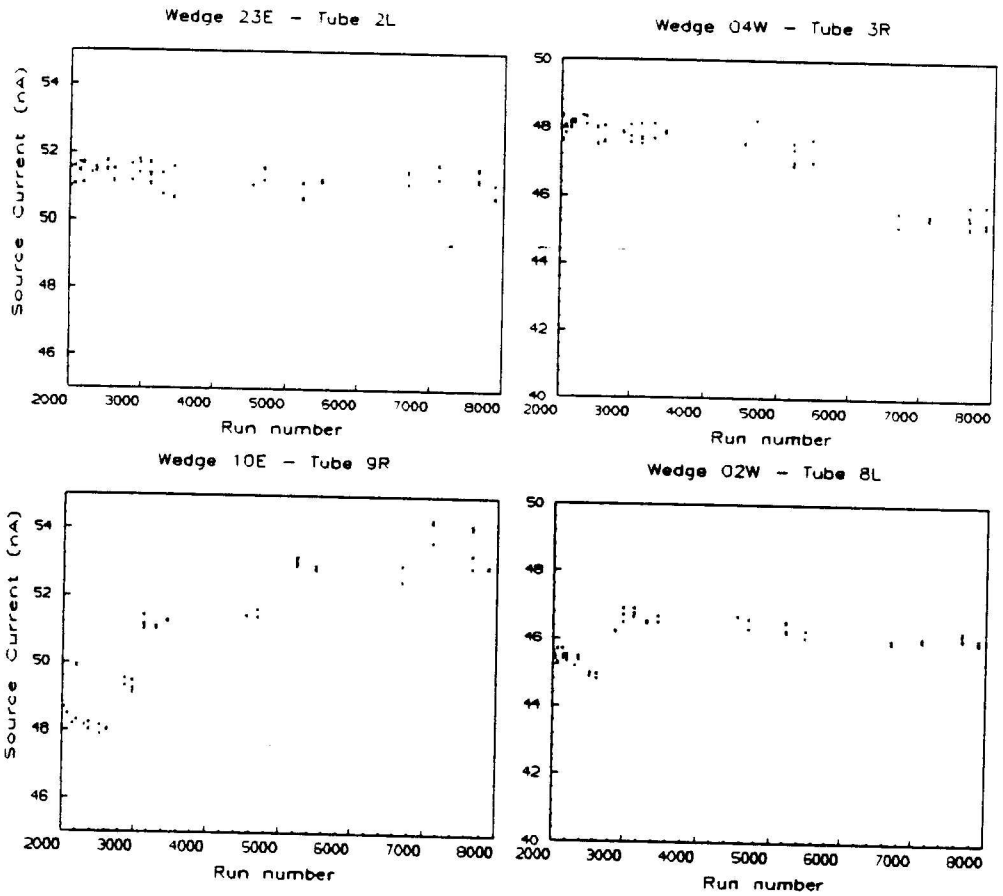

Figure A.8: Long term variations (roughly 9 months) in phototube gains measured by ^{137}Cs source response.

output. Increases in scintillator response to ionizing radiation with magnetic fields present has been observed in other organic scintillators [59]. The calibration constants measured when the field is on enable us to correct for this phenomenon.

A.6 Summary

All channels in the central EM calorimeter were calibrated in a testbeam where the basic measurement was the ratio of the charge channel response to 50 GeV electrons to the current channel response to a ^{137}Cs source. Studies on wedges brought back for repeated calibration indicate a 0.4% error on this measurement. Future testbeam studies and colliding beam data will allow us to continue to monitor the calibration performance.

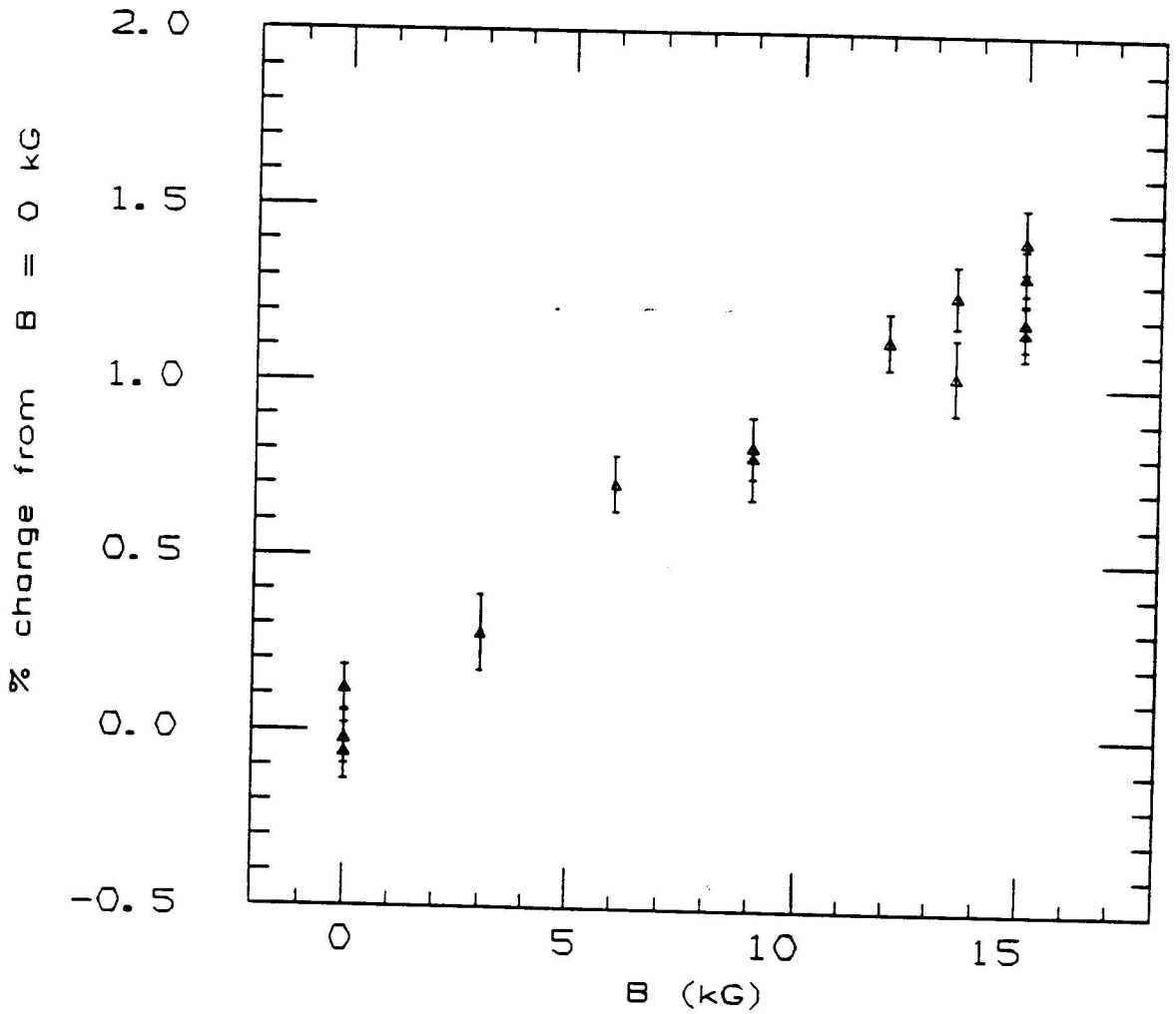

Figure A.9: Percentage change in the calorimeter response to ^{137}Cs source as a function of the solenoidal magnetic field.

Bibliography

[1] F. Abe et al., *Nucl. Instr. and Meth.*, **A271**, (1988) 387.

[2] UA1 Coll., G. Arnison et al., *Phys. Lett.*, **122B**, (1983) 103; *Phys. Lett.*, **126B**, (1983) 398; *Phys. Lett.*, **129B**, (1983) 273; *Phys. Lett.*, **134B**, (1983) 469.

[3] UA2 Coll., M. Banner et al., *Phys. Lett.*, **122B**, (1983) 476; UA2 Coll., P. Bagnaia et al., *Phys. Lett.*, **129B**, (1983) 130.

[4] S. L. Glashow, *Nucl. Phys.*, **22**, (1961) 579.

[5] S. Weinberg, *Phys. Rev. Lett.*, **19**, (1967) 1264.

[6] A. Salam, *Proc.* 8^{th} *Nobel Symp.* (Aspenäsgården, 1968) (Almqvist and Wikell, Stockholm) p. 367.

[7] F. Paige and S. D. Protopopescu, **BNL 38034** (1986).

[8] Descriptions of the electroweak theory can be found in V. D. Barger and R. J. N. Phillips, *Collider Physics* (Addison-Wesley, Redwood City, Ca. 1987)

and C. Quigg, *Gauge Theories of the Strong, Weak, and Electromagnetic Interactions* (Benjamin/Cummings, Reading, Mass. 1983).

[9] P. W. Higgs, *Phys. Lett.*, **12**, (1964) 132; *Phys. Rev. Lett.*, **13**, (1964) 508; *Phys. Rev.*, **145**, (1966) 1156.

[10] α is a function of the Q^2 of the interaction. The value given is valid at very low energies. At energies relevant to W production (i.e. $Q^2 = M_w^2$), $\alpha(M_W^2) \simeq 1/128$.

[11] The value quoted is the mean of two measurements from deep inelastic neutrino scattering from isoscalar targets. They both quote experimental errors of 0.005 and theoretical errors of 0.003 plus a term which depends on the uncertainty of the charm quark mass. H. Abramowicz et al., *Phys. Rev. Lett.*, **57**, (1986) 298; J. V. Allaby et al., CHARM Coll., *Phys. Lett.*, **177B**, (1986) 446.

[12] *SLAC Linear Collider Conceptual Design Report* SLAC Report-229, (1980).

[13] CERN 76-16, *Physics with 100 GeV Colliding Beams*, CERN (1976).

[14] P. Langacker, *Standard Model of the Electroweak Interactions*, DESY 87-153 (1987)

[15] UA1 Coll., C. Albajar et al., *Z. Phys.*, **C37**, (1987) 505.

[16] U. Amaldi et al., *Phys. Rev. D*, **36**, (1987) 1385.

[17] UA1 Coll., G. Arnison et al., *Phys. Lett.*, **166B**, (1986) 484.

[18] L. Balka et al., *Nucl. Instr. and Meth.*, **A267**, (1988) 272.

[19] K. Yasuoka et al., *Nucl. instr. and Meth.*, **A267**, (1988) 315.

[20] S. Bertolucci et al., *Nucl. instr. and Meth.*, **A267**, (1988) 301.

[21] S. R. Hahn et al., *Nucl. Instr. and Meth.*, **A267**, (1988) 351.

[22] Y. Fukui et al., *Nucl. Instr. and Meth.*, **A267**, (1988) 280.

[23] G. Brandenburg et al., *Nucl. Instr. and Meth.*, **A267**, (1988) 257.

[24] S. Cihangir et al., *Nucl. Instr. and Meth.*, **A267**, (1988) 249.

[25] F. Snider et al., *Nucl. Instr. and Meth.*, **A268**, (1988) 75.

[26] F. Bedeschi et al., *Nucl. Instr. and Meth.*, **A268**, (1988) 50.

[27] S. Bhadra et al., *Nucl. Instr. and Meth.*, **A268**, (1988) 92.

[28] M. Atac et al., *Nucl. Instr. and Meth.*, **A269**, (1988) 40.

[29] G. Ascoli et al., *Nucl. Instr. and Meth.*, **A268**, (1988) 33.

[30] K. Byrum et al., *Nucl. Instr. and Meth.*, **A268**, (1988) 46.

[31] E. Barsotti et al., *Nucl. Instr. and Meth.*, **A269**, (1988) 82.

[32] G. Drake et al., *Nucl. Instr. and Meth.*, **A269**, (1988) 68.

[33] H. Brafman et al., *IEEE Trans. Nucl. Sci.*, **NS-32**, (1985) 336.

[34] D. Amidei et al., *Nucl. Instr. and Meth.*, **A269**, (1988) 51.

[35] T. Liss, Internal CDF Note 552, (unpublished).

[36] M. M. Block and R. N. Cahn, *Phys. Lett.*, **188B**, (1987) 143.

[37] M. Bozzo et al., *Phys. Lett.*, **147B**, (1984) 392.

[38] G. J. Alner et al., *Z. Phys.*, **C32**, (1986) 153.

[39] C. Fabjan, in *Techniques and Concepts of High-Energy Physics III*, ed. T. Ferbel, (Plenum Press, New York 1984) pp. 281-336.

[40] S. Kulhmann, Ph.D. thesis, Purdue University, 1988 (unpublished).

[41] E. Berger, Private communication.

[42] Berends, F. A., et al., *Z. Phys.*, **C27**, (1985) 155.; Berends, F. A., and R. Kleiss, *Z. Phys.*, **C27**, (1985) 365.

[43] Glück, M., E. Hoffmann, and E. Reya, *Z. Phys.*, **C13**, (1985) 119.

[44] The dimensionless parameter, $k = E_\gamma/E$, is required to be greater than 0.005.

[45] E. L. Berger, in *Proc. of the Hadronic Session of the Twenty-second Recontre de Moriod*, ed. J. Tran Thanh Van, (Kim Hup Lee Printing Co. Pte, Ltd., Singapore) pp. 3-40.

[46] E. Berger, *Benchmark Cross Sections for Bottom Quark Production*, **ANL-HEP-CP-87-121** (1987).

[47] P. Sinervo and R. Hollebeek, Internal CDF note 656 (unpublished).

[48] K. K. Gan and M. L. Perl, *Int. J. Mod. Phys.*, **A 3**, (1988) 351

[49] G. Alterelli, K. Ellis, M. Greco, and G. Martenelli, *Nucl. Phys.*, **B246**, (1984) 12; G. Alterelli, K. Ellis, and G. Martinelli, *Z. Phys.*, **C27**, ((1985) 617.

[50] UA2 Coll., J. Appel et al., *Z. Phys.*, **C30**, (1986) 1; UA1 Coll., C. Albajar et al., *Phys. Lett.*, **198B**, (1987) 271.

[51] UA2 Coll., R. Ansari et al., *Phys. Lett.*, **186B**, (1987) 440.

[52] UA1 Coll., G. Arnison et al., *Europhys. Lett.*, **1**, (1986) 327.

[53] C. Albajar et al., UA1 Coll., *Phys. Lett.*, **198B**, (1987) 271.

[54] R. Ansari et al., UA2 Coll., *Phys. Lett.*, **194B**, (1987) 158.

[55] The UA1 experiment has detector problems and will miss a significant fraction of the integrated luminosity.

[56] P. Colas, D. Denegri, and C. Stubenrauch, *Combined Limits on the Number of Light Neutrinos and the Top Mass from the Measurement of* $R = \sigma(W \to l\nu)/\sigma(Z \to ll)$, CERN-EP/88-16 submitted to Z. Phys. C.

[57] A. D. Martin, R. G. Roberts, and W. J. Stirling, *Phys. Lett.*, **189B**, (1987) 220.

[58] Energy gain is generally written as (counts/GeV). Storing gain constants in units of (GeV/count) allows us to simply multiply channel ADC readings (in counts) to find the energy.

[59] C. Swenberg and N. E. Geactinov, in *Organic Molecular Photophysics*, ed. J. Birks, (Wiley, New York, 1973) vol. 1.